Lawrence Berkeley National Laboratory

Lawrence Berkeley National Laboratory

Title

NORMAL EMISSION PHOTOELECTRON DIFFRACTION: A NEW TECHNIQUE FOR DETERMINING SURFACE STRUCTURE

Permalink

https://escholarship.org/uc/item/2p8986qm

Author

Kevan, S.D.

Publication Date

1980-05-01

Peer reviewed

eScholarship.org Powered by the California Digital Library
University of California

LBL-11017

RECEIVED BY TIC SEP 3 1980

Lawrence Berkeley Laboratory
UNIVERSITY OF CALIFORNIA

Materials & Molecular
Research Division

MASTER

NORMAL EMISSION PHOTOELECTRON DIFFRACTION: A NEW TECHNIQUE FOR DETERMINING SURFACE STRUCTURE

Stephen D. Kevan
(Ph.D. thesis)

May 1980

Prepared for the U.S. Department of Energy under Contract W-7405-ENG-48

DISTRIBUTION OF THIS DOCUMENT IS UNLIMITED

NORMAL EMISSION PHOTOELECTRON DIFFRACTION: A NEW TECHNIQUE FOR DETERMINING SURFACE STRUCTURE

Stephen D. Kevan

Lawrence Berkeley Laboratory
University of California
Berkeley, CA 94720

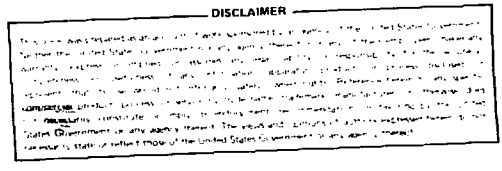

DISTRIBUTION OF THIS DOCUMENT IS UNLIMITED

NORMAL EMISSION PHOTOELECTRON DIFFRACTION: A NEW TECHNIQUE FOR DETERMINING SURFACE STRUCTURE

Stephen D. Kevan

ABSTRACT

The characterization of the geometric arrangement of atoms near a surface is becoming increasingly important in view of the immense technological importance of surface and interface phenomena. Classically, the problems of studying surfaces - the extremely low sample density and difficulty of producing clean, characterized surfaces reproducibly - produced large enough barriers that little accurate information was deduced about surface structure. The advent of ultra-high vacuum technology and of several surface analysis techniques provided a way of substantially overcoming these barriers. Still, however, the number of accurately known and accepted surface structures is relatively few, and these are of relatively simple systems. Traditionally, the technique of choice for determining surface structures has been low energy electron diffraction (LEED), the surface analog of x-ray diffraction. Various weaknesses of LEED have become apparent and have led to efforts to find other techniques which might prove useful in determining surface structure.

It is the purpose of this thesis to characterize one such technique, photoelectron diffraction (PhD), and to show that it has some promise in surmounting some of the problems of LEED. In PhD, the differential (angle-resolved) photoemission cross-section of a core level localized on an adsorbate atom is measured as a function of some

final state parameter. The photoemission final state consists of two components, one of which propagates directly to the detector and another which scatters off the surface and then propagates to the detector. These are added conerently, and interference between the two manifests itself as cross-section oscillations which are sensitive to the local structure around the absorbing atom. We have shown that PhD deals effectively with two- and probably also three-dimensionally disordered systems. Its non-damaging and localized, atom-specific nature gives PhD a good deal of promise in dealing with molecular overlayer systems. It is concluded that while PhD will never replace LEED, it may provide useful, complementary and possibly also more accurate surface structural information.

TABLE OF CONTENTS

I. INTRODUCTION

The increasing technological importance of surface and interface phenomena over the last two decades has led to a major research effort directed toward a fundamental microscopic understanding of both the geometric and electronic structure of surfaces. Reasonably reliable and accurate techniques for determining the geometric arrangement of atoms at a surface have not been developed until the last few years, and these are limited to relatively simple systems. Clearly, the development of such techniques is necessary for an understanding of the electronic structure and chemical reactivity of surface complexes. With these thoughts in mind, the experiments described in this thesis have been designed and performed to evaluate the application of angle-resolved photoelectron spectroscopy to structural determinations of adsorbate-metal surface complexes.

Photoelectron spectroscopy or photoemission is potentially rich in surface structural information. The relatively short mean-free-path of electrons in most solids in the kinetic energy range 5eV $\leq$ KE $\leq$ 1000eV (Fig. 1) indicates that the elastic photoelectron signal originates in the atomic layers closest to the surface. The energy conservation condition contained in the Einstein relation BE = $h\nu$ - KE demonstrates that measurements of elastic photoelectron energy distributions at fixed photon energy will yield binding energies of the various electronic levels near the surface. Aside from this binding energy information, if one measures the photocurrent from single crystalline samples into a small angular aperture (angle-resolved photoemission or

ARP), various momentum conservation conditions can be invoked in addition to the Einstein relation. Such differential ARP cross-section measurements have been shown to contain substantially more information than the total cross-sections measured by angle-integrated photoemission.[1,2]

The application of photoelectron spectroscopy to the study of adsorbate covered surfaces started with the pioneering work of Bordass and Linnett.[3] The earliest applications dealt with binding energies determined by use of the Einstein relation.[3,4] In the ultraviolet photon energy regime, the idea was to measure the binding energies of various states derived from adsorbate molecular orbitals and then to invert the observed energies, yielding surface structural information. The procedure has been shown to work reasonably well in determining the gross structural aspects of surface species,[5-7,18] but usually fails in attempts at determining accurate registries, bond lengths, etc., due to the insensitivity of the binding energy to these parameters, and also to the complexity of the spectra and the resulting data analysis.

If the adsorbate layer is ordered, another technique using ARP can be employed to determine surface structure. Order in the adsorbate layer will produce a two-dimensional valance band structure, derived mainly from adsorbate electronic levels, which can be experimentally determined in a very straight-forward way. The details of the two-dimensional bands will in general be sensitive to surface structure so that a comparison with calculated bands will indicate a certain structure. Several such studies have been successfully undertaken.

The first attempts to use ARP peak intensities to determine surface structure dealt with anisotropic emission from predominantly molecular-orbital-derived valence levels.[12-14] Analysis using symmetry effects[15] or by comparing data with fixed-molecule double-differential photoionization cross-section calculations[16,17] allowed conclusions to be drawn concerning adsorbate bond axis orientation relative to the surface. No conclusions concerning coordination numbers or bond lengths were possible.

In addition to these valence level studies, x-ray photoelectron spectroscopy (XPS) has been applied to the study of core electronic levels of adsorbed species.[18] The initial hope was that core level binding energies would be indicative of surface structure. While there have been some recent successes using this idea,[19] the general result is that while the binding energies are quite sensitive to oxidation state and somewhat sensitive to the changes involved in changing the registry of the adsorbate layer relative to the surface, attempts to extract quantitative chemical information are difficult at best.[16]

Of the various surface sensitive techniques, the surface analog of x-ray diffraction - low energy electron diffraction or LEED - has developed as the best known and most widely applied technique for accurate surface structure determination.[20-22] As such, it is the technique to which most other techniques are compared. While the author sees problems with these comparisons, they are perhaps a good way to start assessing the qualities of other techniques. There are certain shortcomings of LEED which render it less useful in some

systems. In particular, the requirement of ordered overlayers is often not met, especially for larger adsorbate systems, and the difficulty of interpreting LEED intensity vs. voltage curves limits the technique to relatively simple systems. In addition, there is the experimental problem that the primary electron beam often damages the adsorbate layer. This latter problem can be largely overcome by performing LEED experiments in a low current, pulse-counting mode.[23] On the other hand, when performed and interpreted with care, LEED has been shown to yield accurate structures.[24-28] The experimental ease and convenience of the technique has made it quite popular. Clearly, any newly developed technique should be evaluated with these thoughts in mind.

Given these brief introductions to LEED and photoemission, the advent of a new application of both, photoelectron diffraction (PhD), should not seem surprising. While the idea that photoelectrons could be used to perform a LEED experiment was originated by Liebsch in 1974,[29] the experimental verification of the effect was not attained until 1978.[30] A good way of viewing the PhD process is by comparison with LEED. A schematic of both is shown in Fig. 2. In the LEED experiment, an electron impinges on the single-crystalline surface complex and scatters off the various two-dimensionally ordered layers. The wave is diffracted by the surface into angles governed by the two-dimensional momentum conservation relation

$$\vec{k}_{\parallel}' = \vec{k}_{\parallel} + \vec{g}_{\parallel}$$

and the energy conservation condition

$$k_{\perp}' = \left(\frac{2mE}{\hbar^2} - k_{\parallel}'^2\right)^{1/2}$$

where $\vec{k}_{\parallel}, k_{\perp}(\vec{k}_{\perp}', k_{\perp}')$ are the incident (scattered) electron's components of momentum parallel and perpendicular to the surface, E is the kinetic energy of the electron away from the surface, and $\vec{g}_{\parallel}$ is a surface reciprocal lattice vector.[20] In the LEED energy range of $20eV \leq E \leq 200eV$, the elastic component of the reflected electron current is sensitive to the outermost surface layers. Interference between the backscattered waves from the various surface layers leads to structure in the characteristic intensity vs. kinetic energy curves which can be fitted to yield a surface structure. The PhD case is similar except that instead of an electron, an ultraviolet or soft x-ray photon is incident on the surface. If the photon is absorbed by a core electron localized on an adsorbate atom and the kinetic energy of the resultant photoelectron is in the LEED range, it can be elastically scattered off the surface layers, and interference effects will be observed in the same way as in LEED. If the photoemission intensity into a small angular cone is measured as a function of some final state parameter PhD experiments can be performed. For emission normal to the surface, the technique is called normal emission photoelectron diffraction or NPD.[33]

A useful two-step model which clearly indicates the relation of NPD to LEED is illustrated in Fig. 2. The first step is the atomic

excitation of an adsorbate core level which governs the overall emission intensity. In the second step, the electron propagates to the detector either directly or via a final state scattering event. If, after the excitation event, the photoelectron propagates toward the surface with $\vec{k}_{\parallel}$ equal to some surface reciprocal lattice vector, it can be scattered into the normal emission direction via the LEED scattering condition. All of these diffracted components of the outgoing wave must be added to the directly emitted wave coherently, leading to interference. The photoemission final state is said to consist of a time-reversed conerent superposition of several LEED beams.[31-33] A similar idea was initiated by Liebsch.[29] If the photon energy and hence the kinetic energy are varied, the interference condition will change and emission will be either enhanced or decreased. A curve of normal emission cross-section against kinetic energy is expected to show an atomic background modified by characteristic oscillations. The oscillations should, in the same way as for LEED, be sensitive to surface structure. Various studies have been undertaken using this normal emission technique, and it will be of primary emphasis in this thesis.[33]

The experiment need not be performed for emission normal to the surface. Indeed, the photon energy need not be swept at all. Instead, ARP intensity may be measured as a function of some other final state parameter. The details of the LEED beam superposition will depend on all final state parameters. In practice, the best parameter to vary, other than the photon energy, is the azimuthal

emission angle at fixed emission angle relative to both the surface normal and the photon polarization and Poynting vectors. Such azimuthal photoelectron diffracion (APD) experiments have been undertaken and have been used with some success.[35,36]

There are certain important differences between PhD and LEED. First, if one imagines doing a PhD experiment on an isolated adsorbate atom an interference effect would still be observed: there will still be a direct emission wave and waves scattered off the surface which must add coherently, yielding the same characteristic interference effect. The extension to disordered overlayers is obvious: the order in the adsorbate layer required in LEED studies is not predicted to be essential in PhD experiments. The reason for this is that PhD is a more coherent process than LEED due to the difference of boundary condtions: in the two-step model of PhD outlined earlier, the phase of the wave leaving the absorbing atom is fixed, while in LEED the phase of the incident wave is random. This randomness of the phase of the incident wave in LEED is what leads to the coherence length of ~100 Å.[20] In photoemission, such a coherence condition does not arise and, in fact, to speak of a coherence length in PhD does not really make any sense. Related to this prediction is the fact that photoemission is in general sensitive to all of the overlayer rather than just the ordered part. The second important difference between PhD and LEED is in the atom specificity of PhD. The electron source in PhD experiments is localized on a particular atomic species so that, in effect, a structural determination on that species alone can be

undertaken. Every scattering event which leads to the appropriate emission direction contains structural information about the atomic species from which the electron was emitted. The same cannot be said concerning LEED since for that technique a large portion of the scattering events occur from layers which may not be structurally interesting. The structural determination of all atomic species is simultaneous in LEED, leading to the problem sometimes also found in x-ray diffraction of lack of atomic specificity. One obtains atomic positions, but atomic character is generally more difficult to extract from LEED data.

This atomic specificity idea indicates that photoelectron diffraction relates to LEED in much the same way that extended x-ray absorption fine structure or EXAFS relates to x-ray diffraction.[37] In EXAFS, one measures the x-ray absorption coefficient of a material in the energy region near an absorption edge. A typical EXAFS spectrum will show a large increase in absorption at a photon energy corresponding to the binding energy of some core electronic level, followed by small (<5 percent) oscillations in absorption coefficient extending as high as 1000 eV above this edge. The characteristics of these oscillations are dependent, among other things, on the geometry of atoms surrounding the absorbing atom. The origin of the oscillations is described schematically for a diatomic molecule in the right half of Fig. 3. A photon is absorbed by a core electron localized on a particular atomic species. The resulting photoelectron can travel to the neighboring atom and scatter back toward the absorbing atom.

This backscattered contribution to the final state adds coherently to the outgoing contribution, producing interference at the central Since the matrix element governing the absorption event depends on the amplitude of the final state in the region near the central atom nucleus, the x-ray absorption coefficient will be either increased or decreased by this interference. The interference condition will change with energy so that oscillations as a function of energy above threshold are observed. The important result here is that EXAFS is atom specific in the same way as PhD: the EXAFS spectrum of a core level localized on a particular atomic species is measured so that a structural determination of that species alone is possible. Like PhD, EXAFS is a coherent process in that the phase of the wave leaving the absorbing atom is determined only by the kinetic energy. The application of EXAFS to amorphous materials is analogous to the application of PhD to disordered overlayers. The same experimental considerations used to optimize the accuracy of EXAFS can be applied to PhD. Indeed, the similarities between the two - phase coherence and localized nature - in theory make PhD structural determinations as a precise as EXAFS (±.01 Å) and more precise than LEED (±.1 Å). The theoretical complexity of PhD relative to EXAFS, however, may limit PhD's ultimate accuracy.

The relation of PhD to EXAFS should not be overestimated. A simple, single scattering comparison of PhD and EXAFS for a diatomic molecule fixed is space shown in Fig. 3 enlightens the differences between the two processes. As explained earlier, the EXAFS effect is

produced by final state interference occurring at the absorbing atom between the outgoing and nearest-neighbor-backscattered waves.[37] The relative phase of these waves determines whether the interference will be constructive or destructive and hence whether the absorption coefficient will increase or decrease. The backscattered wave accumulates a phase of $2kr$ by traversing the bond length twice. In addition, it undergoes phase shifts due to scattering off the neighboring atom potential ($\delta(\pi)$ in Fig. 3) and to experiencing the central atom potential twice ($2\eta_0$). The important phase factor is the sum of these contributions, shown in Fig. 3.[37,38] It is dependent on internuclear distance, but is independent of angle, at least for single scattering events. For energies greater than 50 eV above the edge, multiple scattering has been found to be unimportant in most EXAFS spectra so that EXAFS oscillation frequencies are determined by this energy dependent phase factor.[38] If the phase shifts are independent of energy, then a Fourier transform of EXAFS oscillations will peak at internuclear distances.[38] Bond lengths are the most readily measured quantities using EXAFS. Unfortunately, the phase shifts are not independent of energy, and it is the determination of these quantities which limits the accuracy of EXAFS in determining bond lengths.[39] η_0, the central atom phase shift, presents particular difficulties since the potential in the region near the absorbing atom is not well defined during the excitation process.[39] In the PhD process, outlined in the left half of Fig. 3, the interference occurs predominantly between the direct and scattered outgoing

waves. This interference is averaged out in EXAFS measurements, a difference which has important consequences. Lee showed in 1976 that a complete 4π steradian angular average of the elastic photocurrent is necessary and sufficient to yield the simple EXAFS formalism.[40] At a crystalline surface, a 2π steradian average is the maximum possible, so that the EXAFS formalism will not in general be applicable to photoemission from crystalline surfaces. The EXAFS effect will, however, be a component of the PhD signal. To the extent that that component is small compared to the outgoing-wave interference (a good approximation) the central atom phase shift which is problematic in EXAFS is absent in PhD.[40] The reason for this is simple when PhD is viewed within the framework of our simple model: the direct and scattered components of the final state will experience the same central atom phase shift on leaving that atom so that the relative phase and hence the interference of the two components will be independent of that phase shift. Hence, it will have no effect on the PhD result. In Fig. 3, the important phase difference in PhD is seen to be independent of η_0. It is dependent on internuclear distance and also on angle, unlike EXAFS. The angular and energy resolution of ARP produces more angular information than EXAFS, as well as largely surmounting the problem of the central atom phase shift. While the information content is potentially higher in PhD than in EXAFS or in surface EXAFS,[41-43] the complexity of the data analysis makes it unclear whether this is an advantage which will ever be realized in practice. The details of this simple single scattering model break

down in the case of PhD: a single scattering formalism is not generally applicable to PhD in the LEED energy range, and to date no simple Fourier transforms have been applied to experimental PhD data with any success. The general conclusions I have drawn, however, should remain intact.

While the emphasis in this thesis is on experiment, some comments on the theoretical considerations of PhD seem appropriate at this point. The scattering processes involved in PhD are very similar to those in LEED. Hence, the successful theoretical treatment of LEED data was a necessary precursor to any treatment of photoelectron diffraction experiments. As mentioned previously, the first theoretical treatment of PhD is due to Liebsch.[29] His effort was to calculate the emission intensity of the sulfur 2s level from a (1x1) monolayer coverage of sulfur on Ni(001). It is to Liebsch's credit that as early as 1974 he was able to predict much of what will be presented in the coming chapters. His results however cannot be experimentally checked since the (1x1) coverage cannot be prepared, and also since the 2s level of sulfur has a very weak cross-section. The more recent theories of Pendry,[45] Tong,[46] and Holland[47] use more current treatments of multiple scattering and have been applied with some success to experimental data on real systems.[33-35,48] We have worked closely with Tong and Li in all of the efforts reported in this thesis, and they deserve a good deal of credit for the successes reported here.

Most of the PhD theories start within the same general framework. The emission amplitude at the detector position $\vec{R}$ is given by[2,29,45-47]

$$\Psi(\vec{R}) = \int G(\vec{R},\vec{r})H'\Psi_i(r)d^3r \qquad (1)$$

which can be derived by straightforward manipulations of the Schrödinger equation.[2] $\Psi_i(r)$ is the initial state wavefunction which, for experimental and calculational ease, is usually taken to be a core level localized on the adsorbate species. H' is the interaction Hamiltonian, and G is the one-electron Green function propagator for the system at $E = h\nu + E_i$. The usual homogeneous term on the right is missing since the initial state will have vanishing amplitude at the detector position. The interaction Hamiltonian for photoemission at a surface has been the subject of much recent and past attention in the literature.[49] In the simple treatments, one assumes that the appropriate gauge may be chosen so that $H' \sim \vec{A}\cdot\vec{P}$, where $\vec{A}$ is the vector potential of the incident radiation, and $\vec{P}$ is the electronic momentum operator. This dipole approximation is good for photon energies below about 10 kV and in regions of constant dielectric function. The spatial dependence of the dielectric function and hence of the vector potential will in general be complicated near a surface. The assumption is usually made that such effects are small and may be neglected. This will be a fairly good approximation for the photon energies well above the substrate plasma energy used in the studies

reported here.[49] In addition, it is usually assumed that the following transformations[46] of the interaction Hamiltonian may be performed without seriously affecting the calculated PhD results:

$$\vec{A}\cdot\vec{P} = \frac{\hbar}{E_f - E_i}\,\vec{A}\cdot\nabla\vec{V} = \frac{m}{\hbar}\,(E_f - E_i)\,\vec{A}\cdot\vec{r} \quad . \tag{2}$$

These transformations are particularly useful when the potential is parametrized in the muffin tin form.[46] They are dependent on the assumption that the same Hamiltonian is used to describe both the initial and final states.

The Green function $G(\vec{r},\vec{R})$ propagates the electron from the surface to the detector after the photoionization step and hence contains the final state scattering details. This can be made clearer by use of the Dyson equation

$$G = G_o + G_o T G_o \tag{3}$$

Substituting into equation 1, we get

$$\Psi(R) = \Psi_D(R) + \Psi_S(R) \tag{4}$$

where $\Psi_D(R) = \int G_o H' \Psi_i d^3r$

and $\Psi_S(R) = \int G_o T \Psi_D d^3r$

are the direct and final-state-scattered contributions to the amplitude at the detector. A similar breakdown into direct and scattered contributions was used by Liebsch.[29] The scattered contribution is seen to be governed by the T matrix describing the scattering in the overlayer-substrate system, in much the same way as in LEED calculations. It is the evaluation of this quantity which makes photoemission theory dependent on LEED theory. After appropriate calculations of Ψ_S and Ψ_D, the photocurrent at the detector may be calculated in the usual way:

$$\vec{j} \propto R^2 \times \mathrm{Im}\left[\Psi(\vec{R})\vec{\nabla}\Psi^*(\vec{R}) \right] \tag{5}$$

Different techniques for evaluating T have been developed and used in LEED and PhD calculations. The beginning of all treatments is in ion core scattering cross-sections. Such scattering profiles in the LEED energy range are strongly peaked in the forward scattering direction,[20,21] and become even more so at higher energies.[36] The essential results of this fact are first that at normal emission the largest effect in PhD will be observed at lower energies where the necessary backscattering amplitude remains appreciable, and that in that energy range multiple scattering paths are important, as in LEED.

It has been shown theoretically that multiple scattering is not as important in PhD as in LEED.[44] Specifically, in both techniques interlayer multiple forward scattering events must be fully treated, but in PhD, only one interlayer backscattering event need be included

in the calculation above 50 eV kinetic energy to obtain the correct, multiply scattered result. In LEED calculations, a more complete treatment of backscattering is necessary.[20,21] In addition, in PhD calculations it has been shown that a single scattering treatment of the intralyer scattering matrices is sufficient.[44] There are two possible explanations for this fact. First, the fact that the final state in PhD is a coherent superposition of several LEED beams leads to a partial angular average. A complete (4π steradian) average leads to the single scattering formalism of EXAFS,[37,40] so that a partial average may make multiple scattering less important. The second possible reason for the simplification is due to the difference in boundary conditions. In LEED, there is a plane wave impingent on a surface. One can imagine each atom scattering some of the amplitude with a resulting spherical wave emanating from each site. Each spherical wave decreases in amplitude as $(r - r_0)^{-1}$x a mean-free-path exponential. This is very similar to the condition which exists after the initial excitation in PhD: an outgoing damped spherical wave. The difference is that there has already been one scattering of the LEED plane wave, while such is not the case in PhD. An amusing result of this analysis is that if LEED were rigorously single scattering phenomenon, we would observe no PhD effect, as the outgoing damped spherical wave would lose flux so rapidly that the amplitude at the scattering centers would be negligible. As is evidenced by the size of this thesis, this is not the case. In any case, the multiple scattering problem is somewhat less complicated in PhD than in LEED.

In addition to these simplifications, our group has recently had some remarkable success in Fourier transforming Tong's theoretical curves calculated at higher energies (100 eV $\leq$ KE $\leq$ 400 eV), yielding structural information directly. If this result were to be generally applicable, it would imply that a much simpler scattering formalism might be applicable in treating PhD data at these higher energies. Unfortunately, experimental verification of this result is not yet available. The present theoretical treatments of both techniques are rather difficult, a fact which limits them to rather simple overlayer systems.

With this brief introduction to PhD and comparison to other structural techniques, I continue with the description of experiments designed to test some of the hypotheses I have made. The design of this thesis is as follows: Chapter II describes the experimental aspects of PhD experiments, including a fairly complete description of a new spectrometer well suited to such studies. Chapter III describes a series of experiments designed to characterize PhD, and Chapter IV provides a summary as well as some thoughts on the future of the technique and its relation to other surface structural techniques.

References: Chapter I

1. Photoemission in Solids, M. Cardonna and L. Ley, Chapter 6, "Angular Dependent Photoemission," N. V. Smith, Springer Verlag, 1978.

2. Photoemission and the Electronic Properties of Surfaces, B. Feuerbacher, B. Fritton, and R. F. Willis, John Wiley, 1979.

3. W. T. Bordass and J. W. Linnett, Nature, 222, 660 (1969).

4. D. E. Eastman and J. K. Cansion, Phys. Rev. Lett., 27, 1520 (1971).

5. J. E. Demuth, Surface Science, 80, 367 (1979), J. E. Demuth and D. E. Eastman, Phys. Rev. Lett. 32, 1123 (1974), J. E. Demuth and D. E. Eastman, Phys. Rev., B13, 1523 (1976).

6. G. Broden and T. Rhodin, Chem. Phys. Lett., 40, 247 (1976), Solid State Commun., 18, 105 (1976).

7. T. E. Fischer, S. P. Kelemen, and H. Bonzel, Surface Sciences, 64, 157 (1977).

8. W. Ebernardt and F. J. Himpsel, Phys. Rev. Lett., 42, 1375 (1979).

9. T. W. Capenart and T. N. Rhodin, J. Vac. Science and Tecn., 16, 594 (1979).

10. S. G. Louie, Phys. Rev. Lett., 42, 476 (1979).

11. P. J. Feibelman and D. R. Hamann, Phys. Rev., B21, 1385 (1980), P. J. Feibelman and F. J. Himpsel, Phys. Rev., B21, 1394 (1980).

12. C. L. Allyn, T. Gustafsson, and E. W. Plummer, Chem. Phys. Lett., 47, 127 (1977).

13. R. J. Smith, J. Anderson, and G. J. Lapeyre, Phys. Rev. Lett., 37, 1081 (1976).

14. G. Apai, P. S. Wehner, R. S. Williams, J. Stöhr, and D. A. Shirley, Phys. Rev. Lett., 37, 1497 (1976).

15. J. Hermanson, Solid State Commun., 22, 9 (1977).

16. J. Davenport, Phys. Rev. Lett., 36, 945 (1976).

17. J. L. Dehmer and D. Dill, Phys. Rev. Lett., 35, 213 (1975); J. Siegel, D. Dill, and J. L. Dehmer, J. Chem. Phys., 64, 3204 (1976); D. Dill, J. Chem. Phys., 65, 1130 (1976); S. Wallace, D. Dill, and J. L. Dehmer, Phys. Rev., B17, 2004 (1978).

18. C. R. Brundle, Surface Science, 48, 99 (1975); J. Vac. Science and Tech., 11, 212 (1974).

19. F. J. Grunthaner, P. J. Grunthaner, R. R., Vasquez, F. Lewis, T. Maserjian, and A. Madhukar, Phys. Rev. Lett., 43, 1683 (1979).

20. J. Pendry, Low Energy Electron Diffraction, Academic Press, 1974.

21. M. A. Van Hove and S. Y. Tong, Surface Crystallography by LEED, Springer Verlag, 1979.

22. F. Jona, Surface Science, 68, 204 (1977).

23. P. Stair, Rev. Sci. Inst., 51, 132 (1980).

24. M. Passler, A. Ignatiev, F. Jona, D. W. Jepsen, and P. M. Marcus, Phys. Rev. Lett., 43, 360 (1979).

25. S. Anderson and J. B. Pendry, Phys. Rev. Lett., 43, 363 (1979).

26. M. Van Hove and S. Y. Tong, J. Vac. Science and Tech., 12, 230 (1975).

27. S. Anderson, J. B. Pendry, B. Kasemo, and M. Van Hove, Phys. Rev. Lett., 31, 595 (1973).

28. F. Frostmann, W. Berndt, and P. Bittner, Phys. Rev. Lett., 30, 17 (1973).

29. A. Liebsch, Phys. Rev. Lett., 32, 1203 (1974); Phys. Rev., B13, 544 (1976).

30. N. V. Smith, P. K. Larsen, and S. Chaing, Phys. Rev., B16, 2699 (1977).

31. P. J. Feibelman and D. E. Eastman, Phys. Rev., B10, 4932 (1974).

32. G. D. Mahan, Phys. Rev., B2, 1334 (1970).

33. S. D. Kevan, D. H. Rosenblatt, D. Denley, B.-C. Lu, and D. A. Shirley, Phys. Rev. Lett., 41, 1565 (1978); Phys. Rev., B20, 4133 (1979).

34. G. P. Williams, F. Cerrina, I. T. McGovern, and G. J. Lapeyre, Solid State Commun., 31, 15 (1979).

35. D. Norman, D. P. Woodruff, N. V. Smith, M. M. Traum, and H. H. Farrell, Phys. Rev., B18, 6789 (1978); D. P. Woodruff, D. Norman, B. W. Holland, N. V. Smith, H. H. Farrell, and M. M. Traum, Phys. Rev. Lett., 41, 1130 (1978); N. V. Smith, H. H. Farrell, M. M. Traum, D. P. Woodruff, D. Norman, M. S. Woolfson, B. W. Holland, Phys. Rev., B21, 3119 (1980).

36. S. Kono, C. S. Fadley, and Z. Hussain, Phys. Rev. Lett., 41, 117 (1978); S. Kono, S. M. Goldberg, N.F.T. Hall, and C. S. Fadley, Phys. Rev. Lett., 41, 1831 (1978).

37. E. A. Stern, Phys. Rev., B10, 3027 (1974); P. A. Lee and J. B. Pendrey, Phys. Rev., B11, 2795 (1975).

38. D. E. Sayers, E. A. Stern, and F. W. Lytle, Phys. Rev. Lett., 27, 1204 (1971).

39. P. A. Lee and G. Beni, Phys. Rev., B15, 2862 (1977).

40. P. A. Lee, Phys. Rev., B13, 5261 (1976).

41. P. H. Citrin, P. Eisenberger, and R. C. Hewitt, Phys. Rev. Lett., 41, 309 (1977).

42. J. Stöhr, D. Denley, and P. Perfetti, Phys. Rev., B18, 4132 (1978).

43. L. I. Johansson and J. Stohr, Phys. Rev. Lett., 43, 1882 (1979).

44. C. H. Li and S. Y. Tong, Phys. Rev. Lett., 43, 526 (1979).

45. J. B. Pendry, Surface Science, 57, 679 (1976); J. Phys., C8, 2413 (1975).

46. C. H. Li, A. R. Lubinsky, and S. Y. Tong, Phys. Rev., B17, 3128 (1978).

47. B. W. Holland, J. Phys., C8, 2579 (1975).

48. S. Y. Tong, C. H. Li, and A. R. Lubinsky, Phys. Rev. Lett., 39, 498 (1977); C. H. Li and S. Y. Tong, Phys. Rev. Lett., 40, 46 (1978); S. Y. Tong and M. A. Van Hove, Solid State Commun., 19, 543 (1976); S. Y. Tong and N. Stoner, J. Phys., C11, 3511 (1978).

49. R.E.B. Mackinson, Proc. Roy. Soc. London, Ser. A, 162, 367 (1937); J. G. Engriz, Phys. Rev., B7, 3464 (1979); P. J. Feibelman, Phys. Rev. Lett., 34, 1092 (1975) and Phys. Rev., B12, 1319 (1975); K. L. Kliewer, Phys. Rev., B14, 1412 (1976) and B15, 3759 (1977); H. Petersen and S.B.M. Hägstrom, Phys. Rev. Lett., 41, 1314 (1978); H. J. Levinson, E. W. Plummer, and P. J. Feibelman, Phys. Rev. Lett., 43, 952 (1979).

Figure Captions: Chapter I

Figure 1. Plot of electron elastic mean-free-path or attenuation length vs. electronic kinetic energy for typical materials. Small mean-free-paths in the LEED energy range result in sensitivity to the outermost layers.

Figure 2. Relation between the LEED and PhD techniques. The PhD final state is the time-reversed coherent superposition of several LEED beams.

Figure 3. Comparison between PhD and EXAFS for a diatomic molecule fixed in space. In EXAFS, the interference effect occurs at the absorbing atom site leading to the importance of the central atom phase shift, while in PhD interference in the outgoing wave dominates for which, to first order, the central atom phase shift is unimportant.

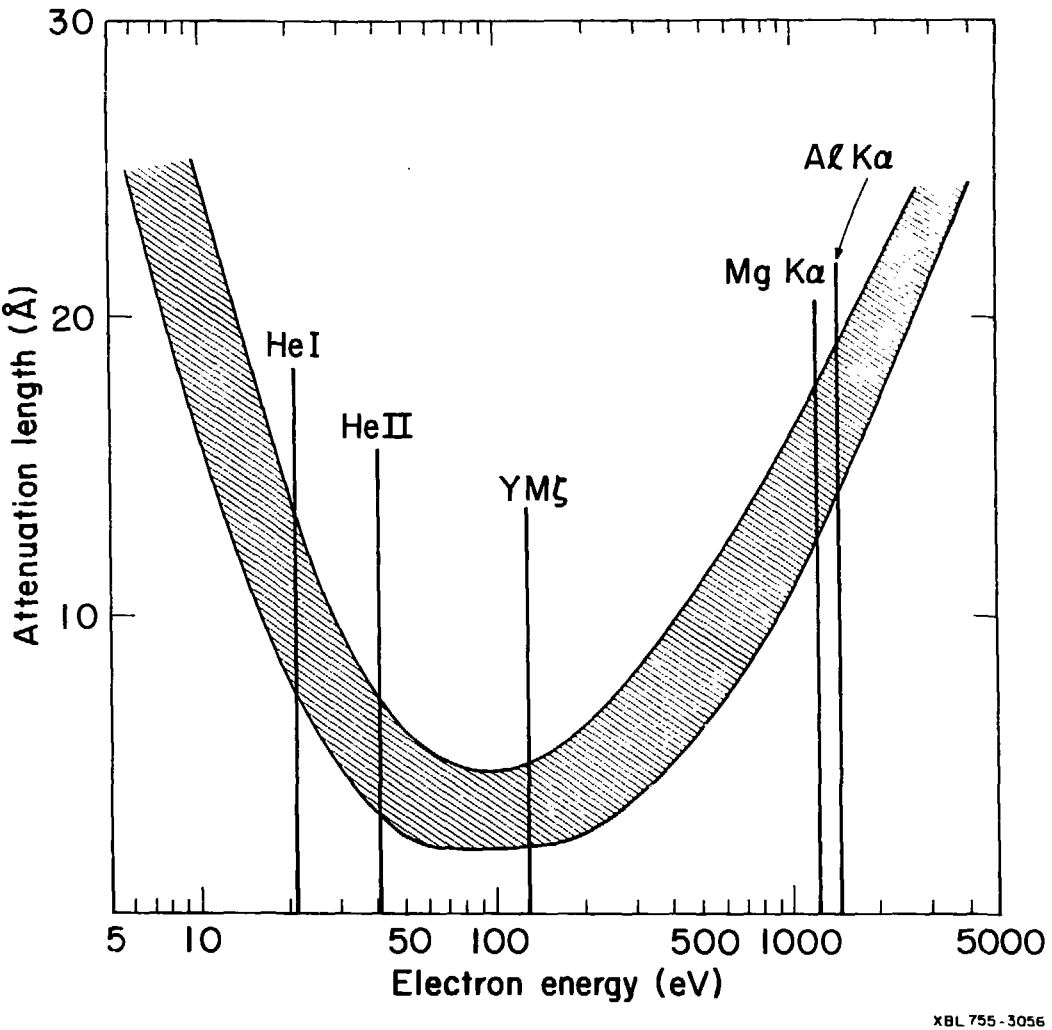
30
20
10
Attenuation length (Å)
HeI
HeII
YMζ
Mg Kα
Aℓ Kα
5
10
50
100
500
1000
5000
Electron energy (eV)
XBL 755-3056

Figure 1

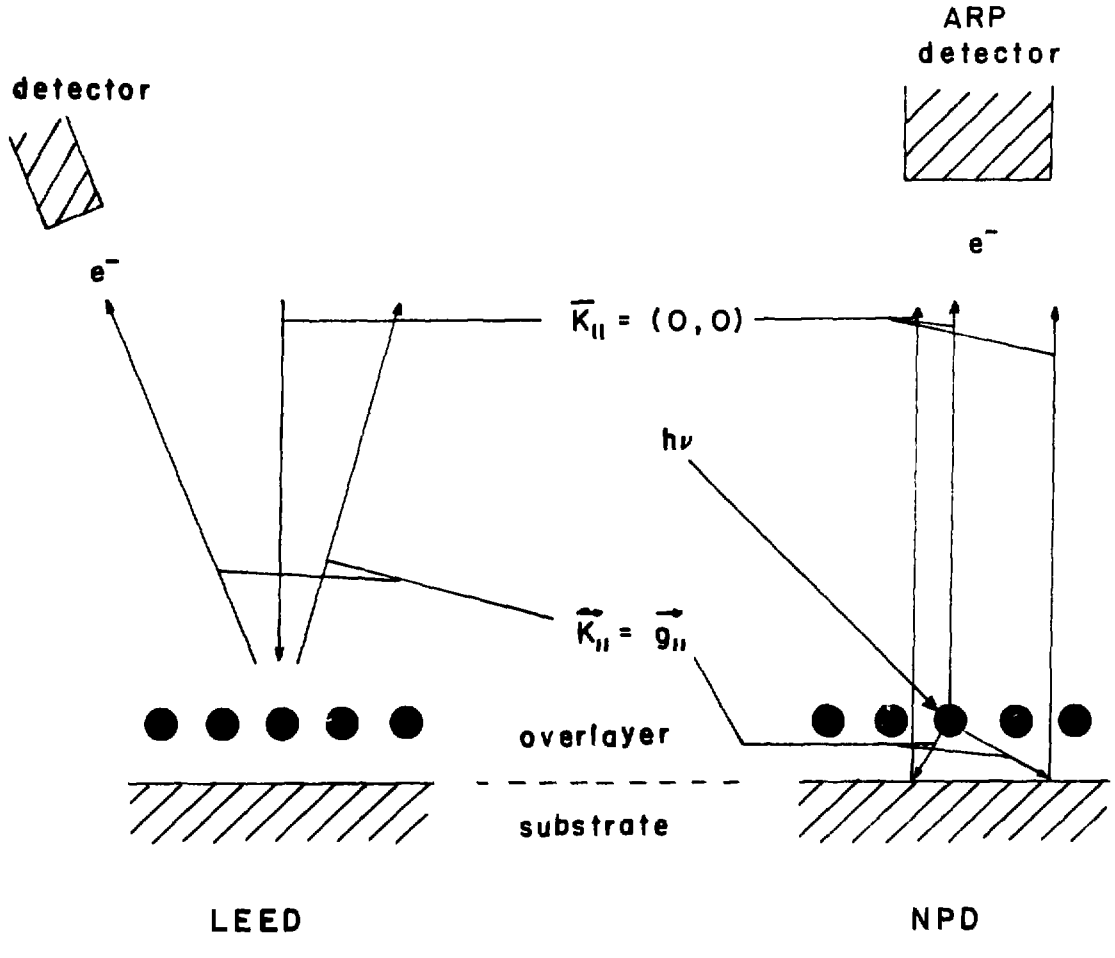

XBL 806-9964

Figure 2

$\Delta\phi = kr(1-\cos\theta) + \delta(\pi-\theta)$ $\Delta\varphi = 2kr + \delta(\pi) + 2\eta_o$

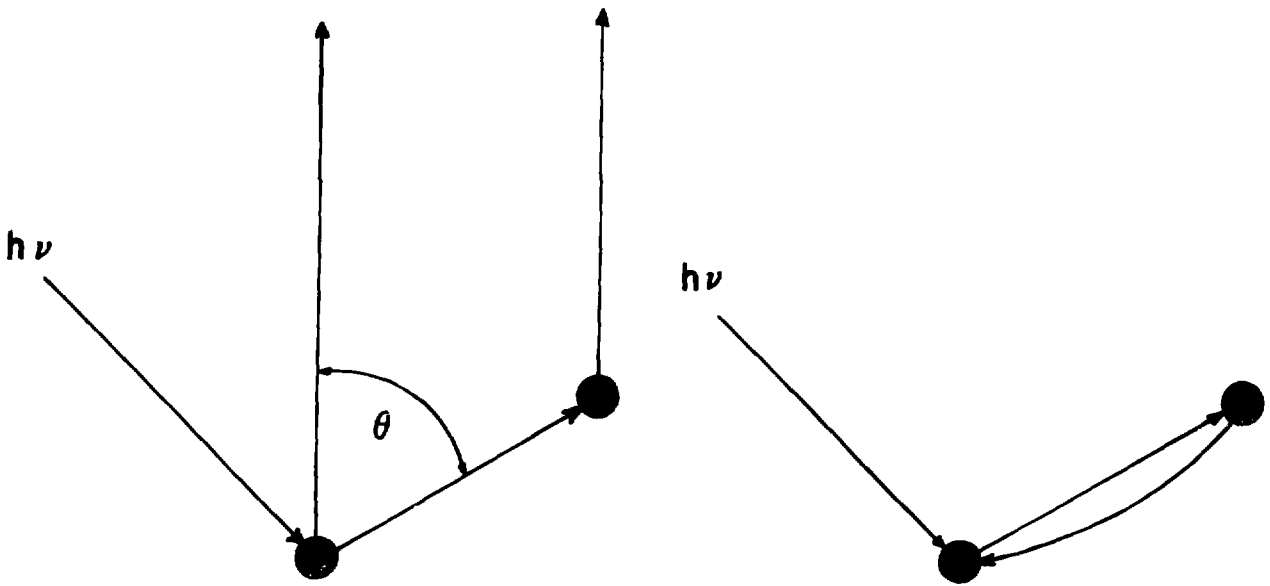

PhD :
outgoing wave interference

EXAFS :
central atom interference

Figure 3

XBL 806-9965

II. EXPERIMENTAL

A schematic of a typical ARP experimental geometry, shown in Fig. 1, demonstrates the many-vectored nature of the technique. In order to attain complete experimental flexibility, one must control both the photon polarization and Poynting vectors as well as the electron emission vectors relative to the sample normal. In addition, since the sample is in general single crystalline, at least one other crystal axis may be important. The scheme which was adopted in the design and construction of a new spectrometer used in all of the experiments described in this thesis was to allow control of the photon beam vectors by rotating the crystal about two orthogonal axes, while the electron emission direction was to be controlled by rotating an energy analyzer in vacuum about two different orthogonal axes. This combination allows nearly complete flexibility in an ARP experiment.

In additon, one would like to perform and control experiments quickly and easily. Various electronic components have aided greatly in attaining these latter desires. An overall schematic of our experimental setup is shown in Fig. 2. The flow in this description of experimental techniques will follow the progress of the ARP experiment shown in Fig. 2 from photon source to electron energy analyzer to data system and electronics.

A. Photon source

As indicated in Chapter I, it is desirable to be able to vary the photon energy and hence electron kinetic energy in a PhD experiment. Moderately intense vacuum ultraviolet and soft x-ray photon sources

are available only by using synchrotron radiation. Such a source is available in the San Francisco Bay Area at the Stanford Synchrotron Radiation Laboratory (SSRL), located on SPEAR, the Stanford Positron Electron Acceleration Ring. If one undertakes the mildly inconvenient transfer of equipment from Berkeley to Stanford, variable photon energy photoemission experiments may be readily performed. A complete descripton of the SSRL facility may be found elsewhere.[1] The valuable characteristic as far as PhD experiments are concerned is that, using the grazing incidence "grasshopper" monochromator, the photon energy may be tuned throughout the soft x-ray region. Many elements have core levels with binding energies in this region of the spectrum, so that PhD experiments are possible. In addition, the light is highly linearly polarized. While the beam is intense relative to conventional Bremsstrahlung sources, the author would like to point out, without going into any great detail, that there is room for substantial improvement in both the flux emanating from the ring as well as in the design of soft x-ray monochromators.

In any cross-section measurement, the incident photon flux is a critical parameter and its measurement is obligatory. We have monitored the incident photon flux at SSRL by measuring the photoyield from a 90 percent transmitting gold mesh. The observed yield was assumed to be proportional to the incident flux and to the gold absorption coefficients measured by Hagemann, Gudat, and Kunz.[2] This latter assumption is subject to some question, but it should introduce at most an error into our data which is a slowly varying

function of photon energy. Such an error will turn out not to be particularly critical. The advantage of using a gold mesh is that photoyield and photoemission experiments may be undertaken simultaneously so that minor fluctuations in beam intensity may be normalized. A complete description of the technique for photoyield measurements maybe found elsewhere.[3]

A plot of photoyield against photon energy taken on the grasshopper monochromator on Beam Line I at SSRL taken under the best possible circumstances is shown at the top of Fig. 3. In this case, a new, 1200 line/mm grating blazed to have maximum transmission at 300 eV was installed in the monochromator. Small absorptions which manifest themselves as decreases in photoyield are observed at the carbon (285 eV) and oxygen (530 eV) K edges. Fairly good intensity is observed as high as 1000 eV. The increase in photoyield for photon energies above 1000 eV is due to the presence of increasing scattered (non-monochromatic) light as one approaches zero order of the monochromator.[4] A correction for this scattered light may be approximated by performing a polynominal extrapolation to lower photon energies as shown in the figure. In this case, the scattered light is as high as 20-30 percent at the oxygen edge. This is a substantial correction which becomes more important at higher photon energies. In order to compare with a case where the situation is less than optimal, Fig. 3 also shows a similar photoyield curve taken using a grating which had been exposed to several months of synchrotron radiation. The curves are not normalized to each other: the flux per unit stored

current in SPEAR is approximately equal at 150 eV photon energy for the two curves. Substantial carbon buildup on the various reflecting surfaces in the beam line is made evident by the large decrease in intensity at the carbon edge.[4] In this case, experiments at photon energies above 280 eV are nearly impossible due to the low monochromatic intensity and consequent high percentage of scattered light. The range of PhD experiments is substantially reduced.

Aside from these scattered light and intensity problems encountered in the soft x-ray regime using the grasshopper monochromator, PhD experiments are substantially limited by the photon energy resolution. The approximate experimentally derived resolution is $\Delta E = 1.8 \times 10^{-2} \times E^2/n$, where E is the photon energy in eV and n is the number of lines per millimeter on the grating. For n = 600, E = 550 eV, the resolution is about 9 eV. Such poor resolution makes it exceedingly difficult even to see a photoemission peak, much less to measure the peak intensity. Again, the accessible energy range is limited at higher energies by this resolution problem. Photoemission experiments above the oxygen edge are at present possible only with new optics in the beam line and using at least a 1200 line/mm grating.

Such experimental constraints should not, however, lead to the demise of the PhD technique. New storage rings soon to be completed at the University of Wisconsin and at Brookhaven National Laboratory dedicated to the production of synchrotron radiation combined with new monochromator designs[5] should surmount these problems.

B. Energy analyzer detector

As mentioned previously, the considerations which have gone into the design and construction of the present ARP spectrometer are flexibility and speed. These considerations have led us to employ a 180° hemispherical sector energy analyzer for two main reasons. First, the hemispherical analyzer can be made small enough to be fairly easily manipulated in vacuum while retaining the advantages of both good luminosity due to its two-dimensional focusing properties as well as its inherently good resolution. The second consideration in our choice of the hemispherical design was the fact that it lends itself easily to a multichannel detection scheme which provides substantial improvements in counting rates. The path of the photoelectrons through the electron lens, energy analyzer, and detector will be followed sequentially in this description.

The electron lens, shown schematically in Fig. 4, was designed to focus electrons of a prescribed range of kinetic energies emitted from the sample onto the entrance slit of the hemispherical analyzer at a fixed median analyzer pass energy. The lens consists of two stainless steel Einzel lenses of the aperture type. In practice, the sample is placed at the focal point of the first lens. The electrons are then uniformly accelerated between the lenses by the amount PE-KE, where PE is the median analyzer pass energy and KE is the kinetic energy. The second lens then focuses the electrons onto the molybdenum entrance slit of the analyzer. The lens system was tested using a ray tracing program prior to construction. A table of voltages for the various lens and analyzer elements is given in Appendix I.

Two molybdenum collimators are added to define the angular acceptance of the analyzer. The exact acceptance angle is determined by these collimators in conjunction with the Helmholtz-Lagrange law of electron optics:[6]

$$\theta_1 E_1^{1/2} \Delta y_1 = \theta_2 E_2^{1/2} \Delta y_2.$$

Here, θ_1 and θ_2 are the entrance and exit angles at axial points x_1 and x_2, Δy_1 and Δy_2 are the linear dimensions of the beam at x_1 and x_2, and E_1 and E_2 are the energies at x_1 and x_2. If we assume unit linear magnification (good to approximately 20 percent), then Δy_1, and Δy_2 are equal so that

$$\theta_2 \quad \theta_a \, (PE/KE)^{1/2}$$

where θ_s is the half angle of electron accepted off the sample and θ_a is the half angle of electrons input to the analyzer. θ_s is constrained to be less than 3° by the first collimator, and θ_a is constrained to be less than 2° in one dimension and 4° in another. In all of the work reported in this thesis, θ_s is limited by the first collimator and is hence a 3° half angle.

A cross-section of the complete lens and analyzer is shown in Fig. 5, and three different views of the assembled system may be seen in Figs. 6-8. The analyzer mean radius is 5.4 cm. and the gap between

hemispheres is 1.25 cm. From these numbers the energy window viewed by the analyzer is calculated to be 1.6 percent of the median analyzer pass energy. The calculated resolution for the .015" entrance slit used in all of the studies reported in this thesis is .4 percent of the pass energy.[6] The actual resolution is .6 percent, the difference presumably being due to fringing effects as well as other inhomogeneities. The hemispheres were constructed from stainless steel for ease in machining as well as mechanical and vacuum stability. The choice was probably the worst possible as far as analyzer surface patch effects and tendency to absorb stray electrons are concerned. For these reasons, a thin coating of Aquadag[7] graphite compound was applied to the hemispherical surfaces, and small improvements in resolution and ineleastic background were observed with no degradation of vacuum integrity.

At the exit end of the analyzer are a series of field terminating wires designed to help preserve the r^{-1} field to the exit plane. There is allowance for five equally spaced wires which, in the usual configuration, would be at voltages dividing the sphere voltages with a r^{-1} functional distributon. The resulting field distribution in the region of the exit plane was optimized by computer calculations. In actual practice, the wires are configured as shown in Fig. 9. The middle wire is removed completely, and the second and fourth wires do not extend completely across the exit aperture. The philosophy behind this configuration is that the field will terminate reasonably well in the middle of the gap without the wires, so that less field termination is required there. This reduces the signature on the area

detector which will be described shortly. After the field termination strips, a grid at the mid-plane (V_2 from Appendix I) voltage is positioned to protect the analyzer field from the high voltages applied to the channel plate. A double channel plate electron multiplier is positioned .050" from the grid, and electrons exiting the analyzer are swept into the front of the plates by a 100V potential. The channel plate voltage of 2kV is divided across the two separate plates, and a gain of 10^6 is attained.

A schematic of the detector assembly and electronics is shown in Fig. 10. The charge exiting the channel plate is swept to a ceramic disk upon which a thin, uniform graphite film of 200 KΩ/square resistance has been evapoarated (see Fig. 11). Aluminum contacts are made at either end of the graphite. The charge is divided by the resistance; depending on where the charge lands, more or less signal will be observed at one contact relative to the other. The two signals are amplified and compared, yielding position sensitivity in one dimension. By observing image charges in a similar fashion on the back of the ceramic plate, position sensitivity may be attained in a perpendicular dimension. This two-dimensional area detector allows a range of kinetic energies to be simultaneously analyzed and provides a factor of 20-30 increase in counting efficiency over a single channel counting mode. Without this increase, most of the experiments described in this thesis would not have been possible. The amplification-digitization circuit will be described in Section D of this chapter. The idea of such an area detector and its application to a channel plate electron multiplier is not new; several similar efforts have been reported.[8]

C. Analyzer drive mechanism and vacuum chamber

The desired flexibility in choice of electron emission angles was attained by mounting the analyzer described in the last section on a two circle goniometer which has proven to be both useful and rugged. The analyzer is mounted as shown in Figs. 6-8 on a carriage which rides on eight wheel bearings along a vertical track through 100°. The track was designed so that at no point in the rotation does anything accepting the analyzer and lens rise to within 2 cm. of the horizontal plane in which the photoemission event occurs. This is convenient when adding ultilities to that plane. The vertical motion is driven by a rotary motion feedthrough located in the center of the mounting flange. The axis of rotation is rotated by 90° using a bevel gear box. The resulting axis is in the horizontal plane and is used to drive two gears, one of which drives a matching gear mounted on the analyzer carriage. Which of these two gears is actually driving the analyzer depends on the position of the anlyzer, as demonstrated by comparing Figs. 6 and 8. Since the drive mechanism is always loaded, there is no backlash and the reproducibility and accuracy after laser allignment is better than 1/4°.

The vertical track is mounted on a horizontal turntable which allows for rotation of ±180° in a horizontal plane. The drive is provided by a rotary motion feedthrough mounted off center on the mounting flange. A gear mounted on the rotary feedthrough couples directly to an internal gear on the underside of the turntable (Figs. 12 and 13). Bearing races are machined directly into the

mounting flange and the turntable, and 1/4" stainless steel bearings provide mechanical lubrication for the horizontal motion (Fig. 13). All moving parts have been treated with a UHV compatible disulfide compound to reduce galling in vacuum.[9] There has been no problem with galling and we have observed no wear after numerous bakes to 200°C and equally numerous shipments between Stanford and Berkeley.

The process of moving eighteen wires with the analyzer in vacuum is a feat which deserves some comment. Movable contacts are required to accomodate the horizontal and vertical motions. Previous experience with sliding contacts led us to avoid that particular solution. The solution which we decided to use employs two sets of inconel X-750 springs[10] which are non-magnetic, bakeable, and compatible with our ultrahigh vacuum requirements. They provide electrical contact with little chance of shorting or opening. Those on the vertical motion (see Figs. 6-8) are nearly at rest midway through the vertical arc, and fan out on either side of that position. The springs on the horizontal motion are located radially about the center of the bottom flange. The eighteen high voltage UHV feedthroughs are welded on the periphery of a 6" Conflat flange (Fig. 14). Wires are routed up the center of the chamber and make contact with the springs at a grooved ceramic spool. The springs fan out radially from the spool to a ring mounted on the turntable (Fig. 15). As the turntable rotates, the springs extend and wrap orderly around the ceramic spool (see Fig. 16), limiting the horizontal motion to ±180°. The springs have a resistance of 30 ohms each and an inductance of about 50 microhenries. Both of

these values are negligibly small for our application. We have had little problem with shorting and none with open contacts, and the springs have shown little wear after two years of use. All contacts are ensured with gold plated set screws to prevent galling.

The rest of the vacuum chamber is standard UHV equipment. There are three horizontal planes of interest shown in Fig. 17. The uppermost plane provides several sample preparation utilities: LEED/Auger optics, argon ion sputtering gun, a gas doser, and facilities for sample fracture and cleaving. Ample ports have been provided for expansion. The middle plane is dubbed the source plane and is the plane in which photoemission experiments are performed. The bottom plane is a utility plane containing ionization gauges, windows, and a pumping port. The chamber can be baked to temperatures in excess of 200°C, and is pumped by a 220 liter/sec. ion pump, a titanium sublimation pump, and a helium cryopump, to pressures as low as $1\text{-}2\times10^{-10}$ torr.

The sample is mounted on axis on a Varian manipulator which has been modified to allow the sample to be cooled to 100K and resistively heated to 1300K. Rotations of the sample normal through 270° in one plane, and azimuthal rotations of 100° about the sample normal are possible. More than one sample may be mounted at once at the cost of some flexibility. An extended z-axis motion allows for transfer of the sample between the photoemission and sample preparation planes.

D. Detector electronics and data system

In section B of this chapter an electron detector was described which allowed for simultaneous analysis of a range of kinetic

energies. In this section I describe briefly the electronics which take the pulses from opposite ends of the graphite resistor, amplify and compare them, and then produce a digital word which describes where the electron exited the analyzer. In addition, the path of the resulting data is traced through a buffer memory and into the microprocessor dedicated to controlling the counting system.

A schematic of the digitization circuit is shown in Fig. 18. Only the circuit for one dimension is shown, but the other is identical. The first step consists of two charge sensitive amplifiers with a balanced gain of 2.5×10^{-6} volts/electron for the "real charge" circut and 10×10^{-6} volts/electron for the "image charge" circuit. The higher gain for the image charge circuit is necessitated presumably by dielectric loss in the ceramic disk. As mentioned previously, the real charge circuit operates in the energy analysis dimension or radially in the hemispherical analyzer exit plane, while the image circuit operates in the perpendicular dimension. The peaks of the pulses output from the amplifiers are latched by sample and hold circuitry. The two voltage levels from the sample and hold for the real charge circuit are labelled x_1 and x_2. We actually wish to obtain $x_1/(x_1+x_2)$ to normalize differences in gain on different areas of the multiplier. Hence, the sum (x_1+x_2) is formed by a straightforward analog summing junction and is used as the reference voltage for what is essentially an 8-bit analog-to-digital converter (ADC). The analog input to the ADC is x_1, so that the output is x_1 relative to (x_1+x_2), with eight bit precision.

The ADC circuitry works on the successive approximation principle. A successive approximation register (SAR) initiates with the binary value 10000000. That value is input to a fast eight bit digital to analog converter (DAC) along with the reference voltage (x_1+x_2). The analog output from the DAC is compared with x_1, and the next bit of the SAR is tested in a similar fashion. After eight iterations, the value $x_1/(x_1+x_2)$ is determined with eight bit precision. Simultaneous with this real charge digitization, the image charge circuit produces $y_1/(y_1+y_2)$. The two resultant digital words are latched and sent in parallel to the control circuit box called the "one-dimensional digitizer." The y data word could be treated on the same footing as the x data word producing a two-dimensional area detector. In our application, however, the y data are less important than the x data since the x data contain electron energy information. It was convenient to use the y data to form a window which defines the range of data to be counted in a direction perpendicular to the energy dimension. This allows a reduction in dark count by about a factor of 5, and also allows the angular resolution of the analyzer to be reduced in one dimension. The "y-window" so formed is variable and tuned electronically. In addition to this window function, the y data word is used along with the x data word to drive an x-y oscilloscope, producing a real time picture of where the electrons hit the channel plate. For each valid count, the appropriate channel in a 256 word, 12 bit buffer memory is incremented. The total amplification-digitization process requires at present 9-10 microseconds, allowing a

most difficult area to provide continuity from one student to the next in a research group is in the "novel programming approaches" used by the first. Hence, a more complete description of the foreground program including a flow chart can be found in Appendix II.

E. Experimental techniques

In any surface science research effort, a substantial amount of preparative effort is expended prior to the rather limited time spent actually accumulating data. A surface experimental thesis would not be complete without some explanation of the techniques used in producing an oriented, single crystalline, clean surface, in preparing and characterizing submonolayer coverages of some foreign material, and finally in carrying out photoelectron diffraction experiments.

All single crystal samples were cut from 99.999 percent purity nickel single crystal stock. The stock was first oriented with Laue x-ray backscattering to within 1° of the desired orientation, and then approximately 1 mm x 8 mm x 8 mm slabs were spark cut perpendicular to the desired axis. The faces were polished to 1 micron smoothness and etched in a solution of 30 percent nitric acid, 10 percent sulfuric acid, 10 percent orthophosphoric acid, and 50 percent glacial acetic acid. The polished crystals were mounted in the spectrometer, which was then pumped by standard techniques to a base pressure as low as 2×10^{-10} torr and as high as 7×10^{-10} torr. The crystals were cleaned by the standard treatment of argon ion etching followed by annealing to 600-800°C to remove surface damage caused by the etching. While the resulting surfaces always displayed sharp (1X1) LEED

patterns indicative of long range (~500 Å) order in two dimensions, residual surface impurities, mostly carbon and sulfur, were often observed using Auger electron spectroscopy. Residual sulfur was found to migrate to the surface of the hot sample and could thus be efficiently removed by simply heating the sample to 600°C and sputtering for extended periods. Once removed from any crystal, sulfur contamination was never again a problem. Carbon, on the other hand, produced greater difficulties as it moves into the bulk of a hot crystal and migrates to the surface as the sample cools after annealing. The most efficient way of removing residual carbon was to cycle the heating while sputtering. After enough cycles, the carbon contamination was undetectable.

After producing a clean and ordered Ni surface, controlled exposures to the appropriate gaseous species were performed. We have found that the most reproducible exposures were obtained by directing an effusive beam at the sample for a certain amount of time. Our gas handling system, outlined in Fig. 19, is designed with flexibility and utility in mind. Several gases are available on the same line. the typical procedure for exposing the sample to a particular gas is as follows. The sample is first positioned 1 cm. from the .003" diameter aperture. The appropriate gas is introduced to the region behind the aperture at a pressure of about 1 micron. The sample is exposed to the resulting effusive beam at an equivalent pressure as much as two orders of magnitude higher than the ambient pressure during dosing. The advantage over simply backfilling the chamber to a higher pressure

is that the chamber remains somewhat cleaner. There are two other important aspects to the effusive beam dosing method. First, the gas behind the aperture need not be exposed to a hot ion gauge filament, as the pressure there is proportional to the ambient chamber pressure for an effusive beam. This is important when exposing to reactive gases such as H_2Se or H_2S as these gases decompose on contacting a hot filament. Second, the 30 liter/second ion pump allows both the region behind the variable leak valve and behind the aperture to be quickly pumped to a pressure of less than 1×10^{-6} torr. The fact that the variable leak valve can be pumped from both sides is important in reducing the valve's memory when changing from one gas to another. Pressures below 1×10^{-6} torr are sufficiently low that the pressure in the chamber is not adversely affected, and also that a good ambient base pressure behind the aperture before dosing is provided. A complete mathematical description of the doser is given in Appendix III.

Exposures for the various gases were typical of those quoted in the literature for similar coverages.[12] Selenium and sulfur overlayers were formed by decomposing H_2Se and H_2S on the clean surface. The c(2X2) overlayers of Se and S on Ni(001) and Ni(011) required 20-30 Langmuirs (1 Langmuir = 1L = 1×10^{-6} torr-sec), while the p(2x2) structures on Ni(001) required 5-6L. The gases were found to decompose slowly on contacting the copper gaskets used in making UHV seals, so that it was important to replenish the gas behind the variable leak valve before every exposure. Exposures on Ni(111)

deserve special comment and will be described more thoroughly in the next chapter. CO exposures were usually quite small (1-2L). In general, the minimum exposures necessary to produce the desired structure were used in order to avoid higher compression, multiple-site coverages.

There are several possible modes of actually carrying out photoelectron diffraction experiments. As mentioned in Chapter I, the experiments described in this thesis amount to differential cross-section measurements as a function of photon energy at fixed angle. One could in principle measure the ARP peak height of some adsorbate core level while sweeping the photon and kinetic energies. This technique suffers from the problem that peak shape and height are functions also of the monochromator resolution and hence of the photon energy. The main features of this constant-initial-state mode would be correct, but inaccuracies would arise in the relative intensities.

One could improve on this technique by integrating over a small energy width and possibly also subtracting a background derived by averaging count rates above and below the peak energy. Such a procedure has been used in other photoelectron diffraction studies with some success.[13] The safest albeit most time consuming way of measuring core level cross-sections is to measure the ARP spectrum in the region of the peak binding energy at a series of photon energies and then to subtract a smooth background before calculating a peak area. The peak area is then corrected for incident photon flux and for analyzer efficiency. This is the procedure we have adopted in all

of the studies described in this thesis. The corrections for photon flux and analyzer transmission have been performed in the following ways. The integrated gold photoyield is measured over the course of the spectrum. The photoyield is divided by the gold absorption coefficient at the corresponding photon energy giving a number proportional to the integrated photon flux, and the peak area is divided by the result. This procedure clearly will not normalize rapid changes in photon flux, but such changes are unusual and would be difficult to normalize in any case. The analyzer and lens transmission, for fixed median pass energy, is predicted to be proportional to $(KE)^{-1}$. Hence, the peak areas are also multiplied by the kinetic energy at the peak. Such a data acquisition mode is the slowest possible, but the low fluxes available at SSRL warrant such care. The newer synchrotron radiation sources, and perhaps even SSRL when dedicated to the production of synchrotron radiation, should make the more rapid and efficient modes acceptable. The result of the various techniques is of course the same: the measurement of differential cross-section as a function of photon energy.

References: Chapter II

1. K. O. Hodgson, H. Winnick, and G. Chu, eds., Synchrotron Radiation Research, SSRP Report 76/100.

2. H.-J. Hagemann, W. Gudat, and C. Kunz, DESY Report SR-74/7, May, 1974, (unpublished).

3. D. Denley, Ph.D. thesis, University of California, Berkeley, Lawrence Berkeley Laboratory Report No. 9482.

4. D. A. Shirley, Lawrence Berkeley Laboratory report No. 7632, Conference Proceedings, Workshop on X-ray Instrumentation and Synchrotron Radiation Research, SSRL, April, 1978. D. Denley, P. Perfetti, R. S. Williams, D. A. Shirley, and J. Stohr, Phys. Rev., B21, 2267 (1980).

5. M. R. Howells, Brookhaven National Laboratory report No. 2663, Proceedings, Conference on Synchrotron Radiation Instrumentation, Gaithersburg, Md., June, 1979.

6. E. M. Purcell, Phys. Rev., 54, 818 (1938); see also C. E. Kuyatt, "Electron Optics Notes," unpublished.

7. Acheson Colloids Co., Port Huron, Mi.

8. M. Lampton and C. W. Carlson, Rev. Sci. Inst., 50, 1093 (1979), W. Parkes, K. D. Evans, E. Mathieson, Nuc. Inst. and Methods, 121, 151 (1974), E. Kellog, P. Murray, and L. Speybroeck, Rev. Sci. Inst., 47, 282 (1976).

9. Northwest Dycronite, Inc., Mountain View, Ca.

10. Lee Spring Co., Brooklyn, N.Y.

11. W. J. McG. Tegart, The Electrolytic and Chemical Polishing of Metals, Pergamon Press, London (1959).

12. H. D. Hagstrom and G. E. Becker, J. Chem. Phys., 54, 1015 (1971).

13. See Chapter I, refs. 34-5.

Figure captions: Chapter II

Figure 1. Schematic of and definition of angles involved in a typical ARP experiment. Polarization of the incoming photon (not shown) may also be important.

Figure 2. Overall schematic of our ARP setup. Photons provided by SPEAR are focused onto the entrance slit of a grazing incidence grasshopper monochromator. The resulting monochromatic photons are then focused onto our sample and the photoelectrons produced are energy analyzed and counted.

Figure 3. Gold photoyield as a function of photon energy on the grasshopper monochromator at SSRL. The top curve was taken with all new optics, while in the lower curve the optics had been exposed to at least several months of synchrotron radiation. The two curves are not normalized; see text.

Figure 4. Cross-section of the electron lens designed to focus electrons from the sample of a given kinetic energy onto the entrance slit of the analyzer at a fixed analyzer pass energy. The first three elements comprise the first Einzel lens. This is followed by a two-stage decelerator and the second Einzel lens which focuses the electrons onto the entrance slit.

Figure 5. Cross-section of the energy analyzer, lens, and multiplier-detector assemblies.

Figure 6. Analyzer and drive mechanism after assembly before insertion into the vacuum chamber.

Figure 7. Illustration of the horizontal motion of the analyzer drive.

Figure 8. Illustration of the vertical motion of the analyzer drive. The two motions are continuous, but the vertical motion is coupled to the horizontal.

Figure 9. Configuration of the field terminating electrodes in the analyzer exit plane.

Figure 10. Schematic of the resistive anode multichannel detector and electronics.

Figure 11. The resistive anode made of graphite evaporated onto a ceramic substrate with aluminum contacts on the end. The reverse side is identical except that it is rotated by 90°. Evaporations were as uniform as possible and were performed on a heated substrate to insure temperature stability.

Figure 12. Underside of the horizontal motion turntable showing the lubricated gear, bearing race, and springs to make electrical contacts.

Figure 13. Bottom flange with turntable and analyzer removed showing the location of the horizontal motion drive gear and bearing race.

Figure 14. Electrical feedthrough flange and first wiring.

Figure 15. Bottom flange with turntable mounted, showing contact springs in the relaxed position.

Figure 16. Bottom flange and turntable with contact springs in extended position.

Figure 17. Schematic of the vacuum chamber showing the three major planes of interest.

Figure 18. Schematic of the digitization circuit. See text for description.

Figure 19. Schematic of our gas handling system.

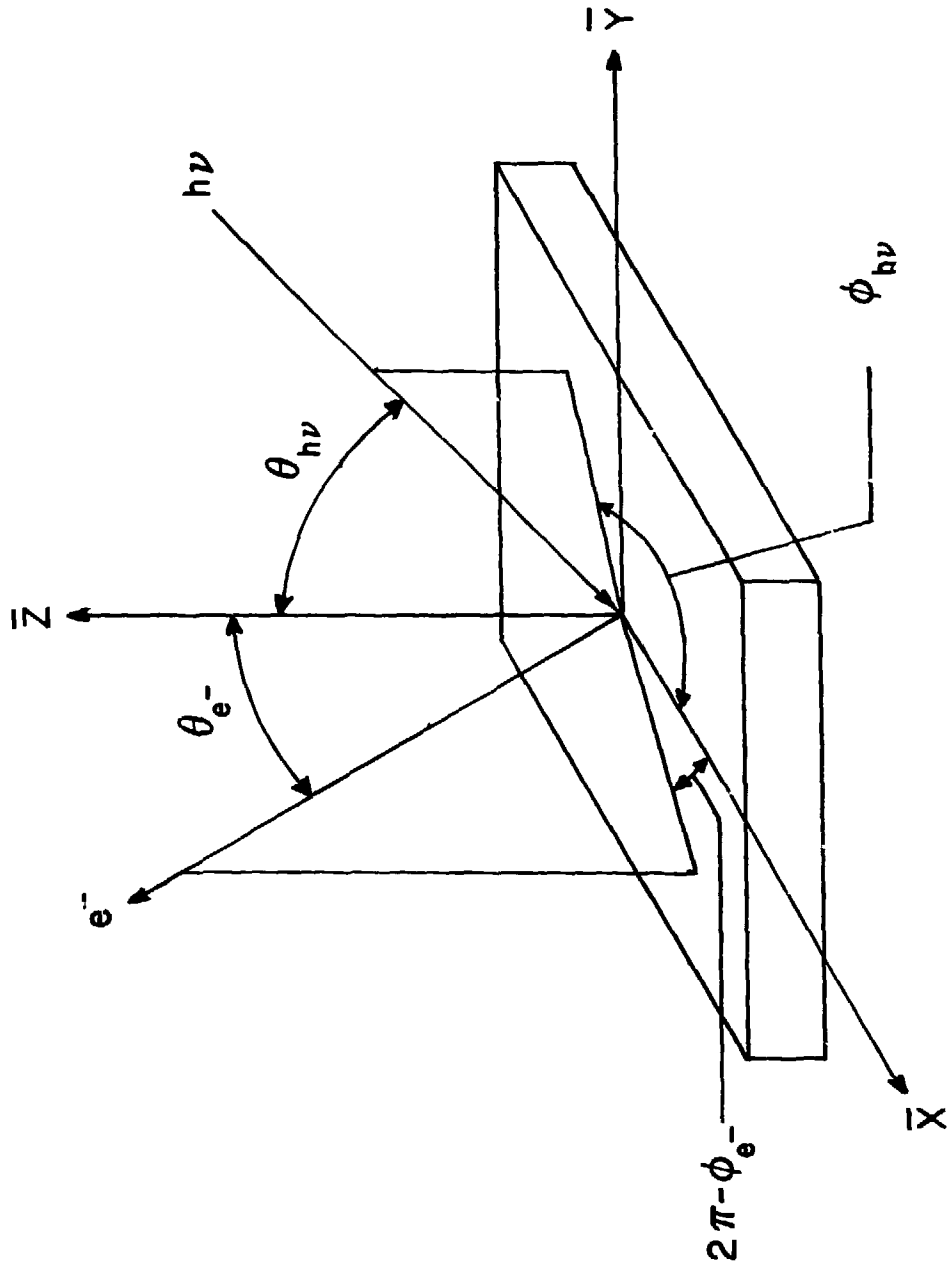

XBL 806-9958

Figure 1

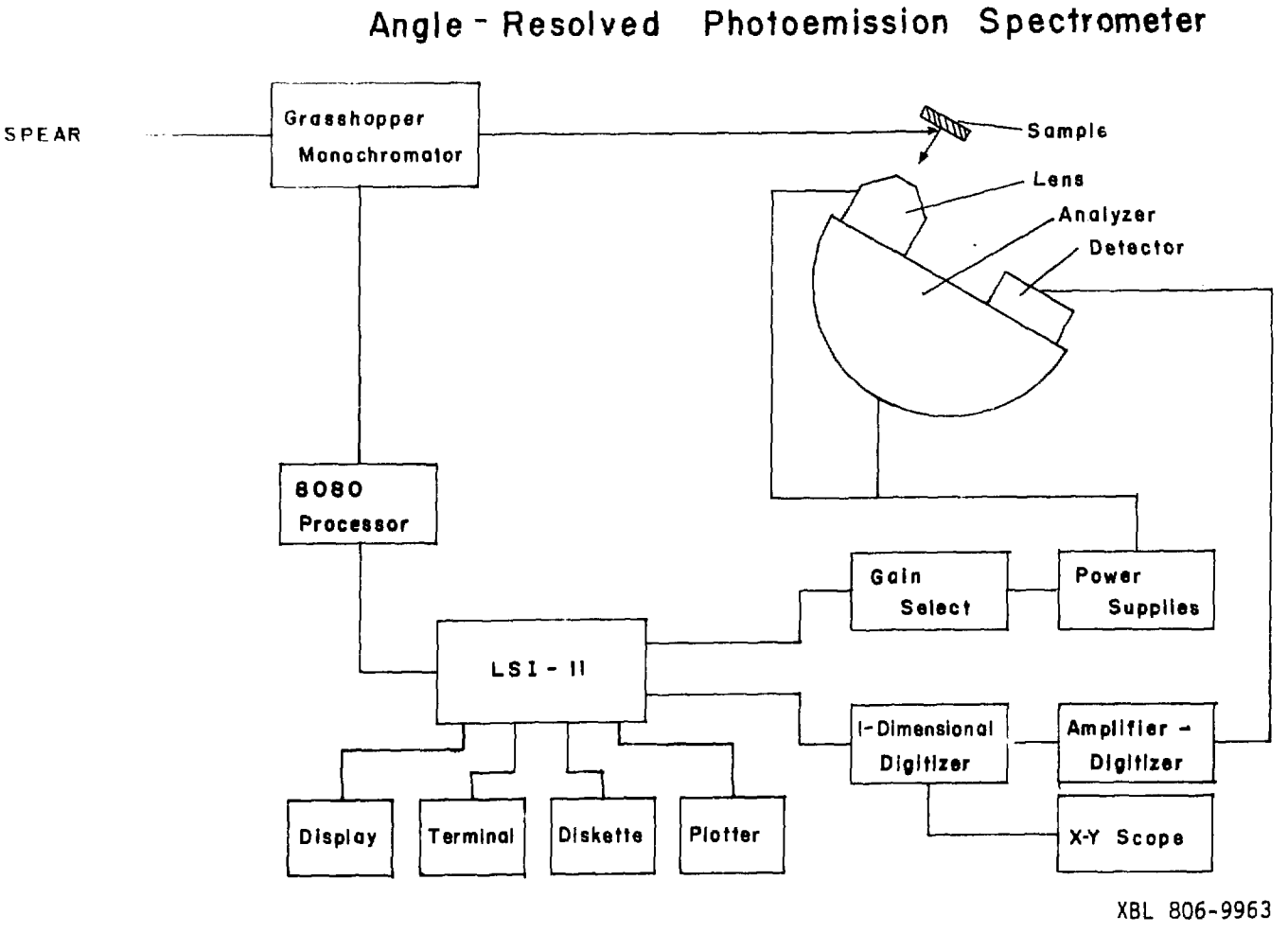
Angle - Resolved Photoemission Spectrometer
SPEAR
Grasshopper Monochromator
Sample
Lens
Analyzer
Detector
8080 Processor
Gain Select
Power Supplies
LSI - 11
1-Dimensional Digitizer
Amplifier - Digitizer
Display
Terminal
Diskette
Plotter
X-Y Scope
XBL 806-9963

Figure 2

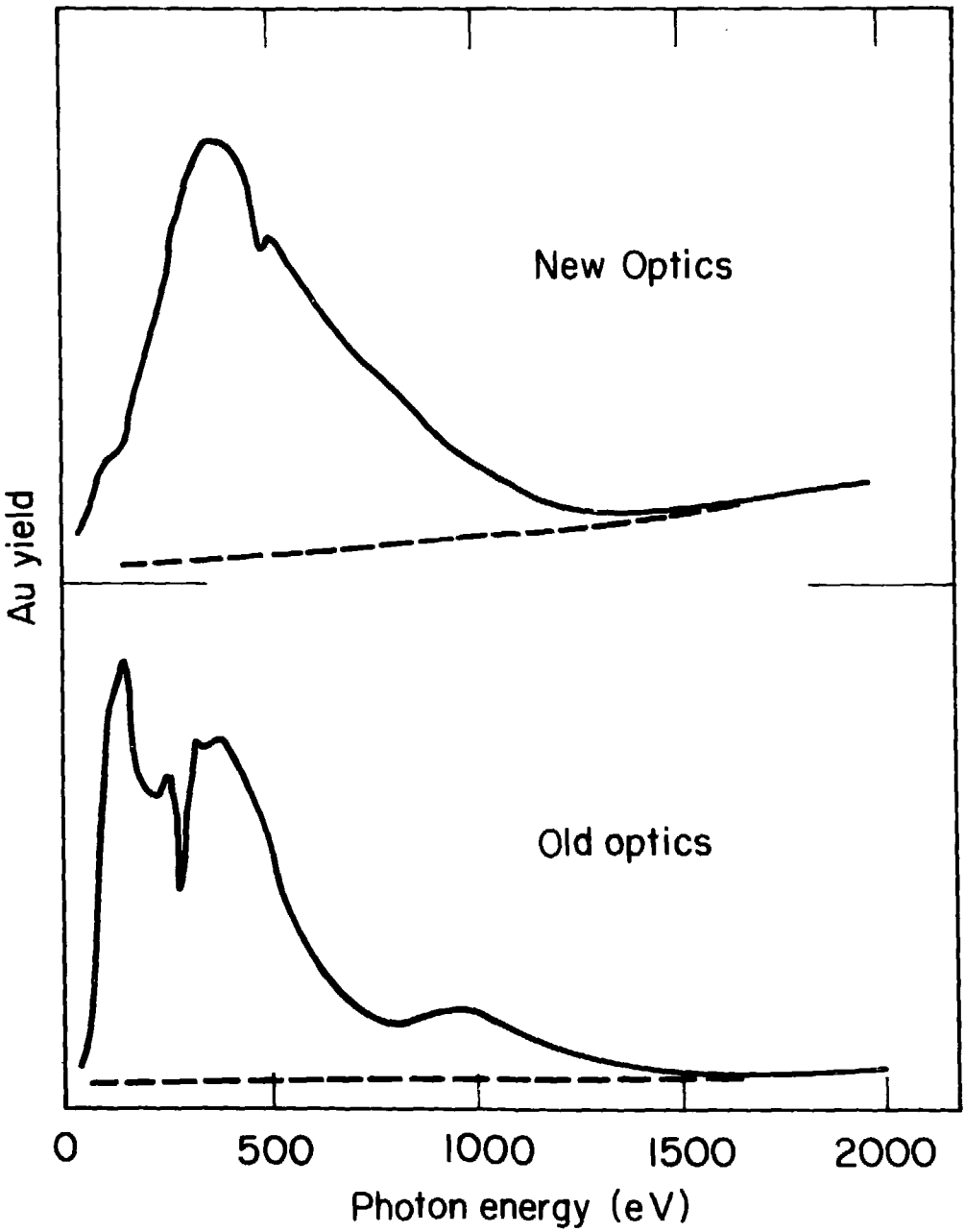

XBL-806-1357

Figure 3

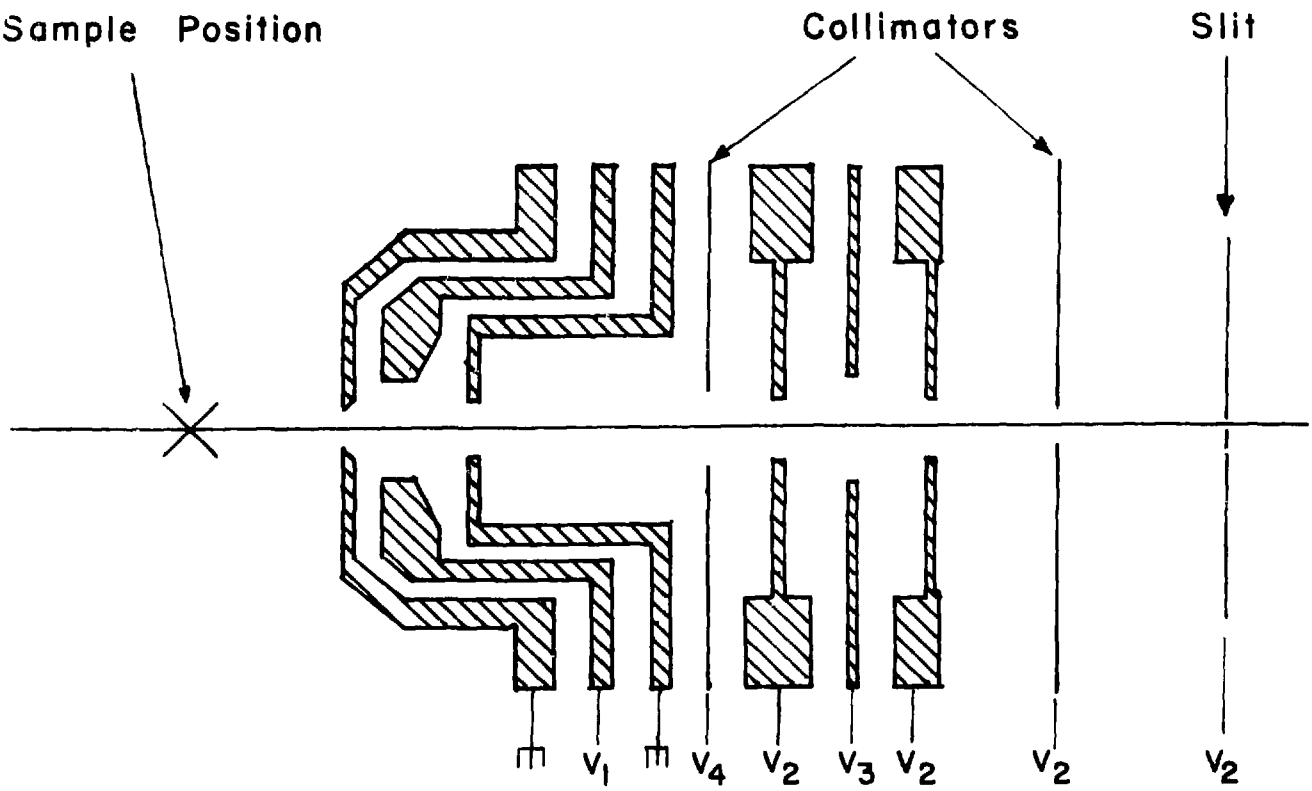

Electron Lens Schematic

XBL 806-9957

Figure 4

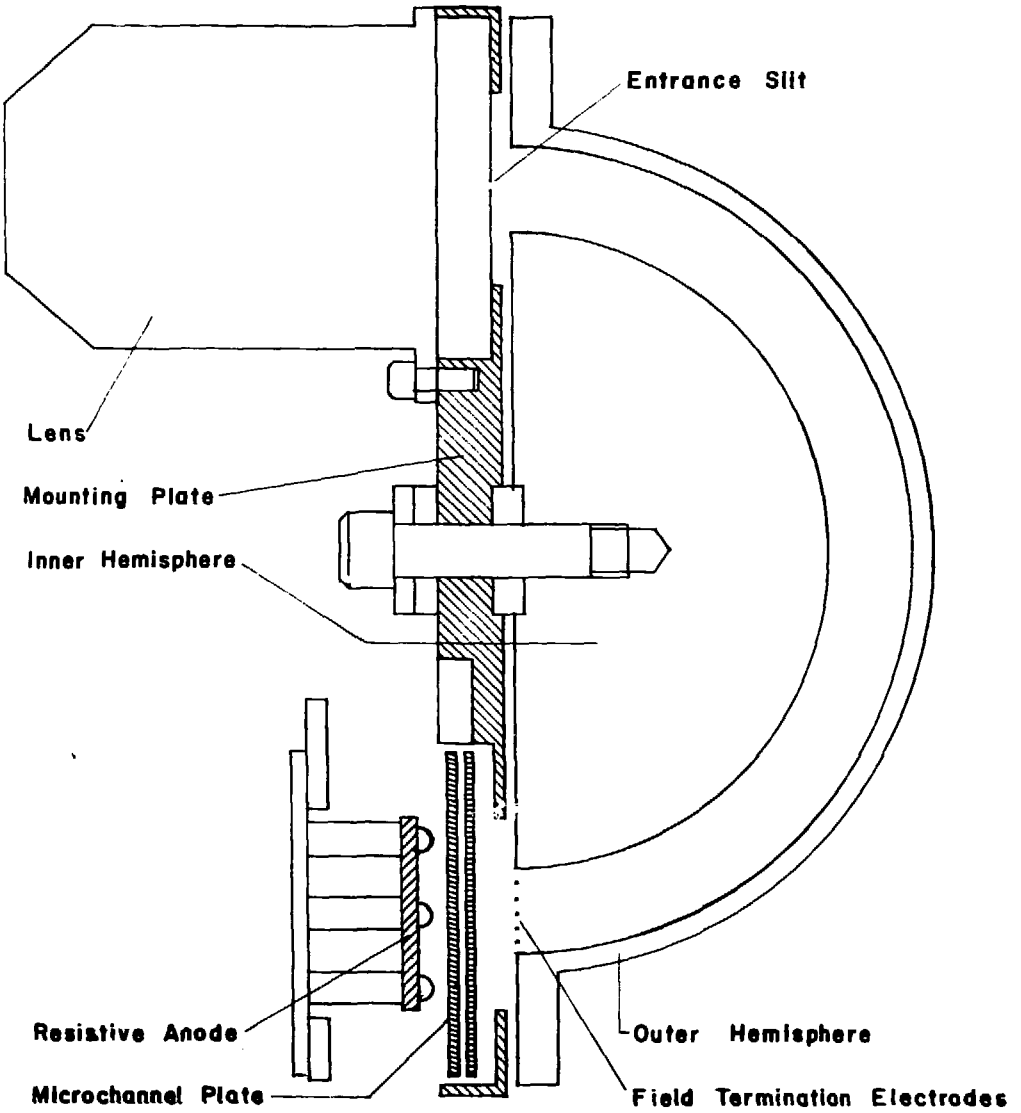

ARPES Energy Analyzer

XBL 806-9959

Figure 5

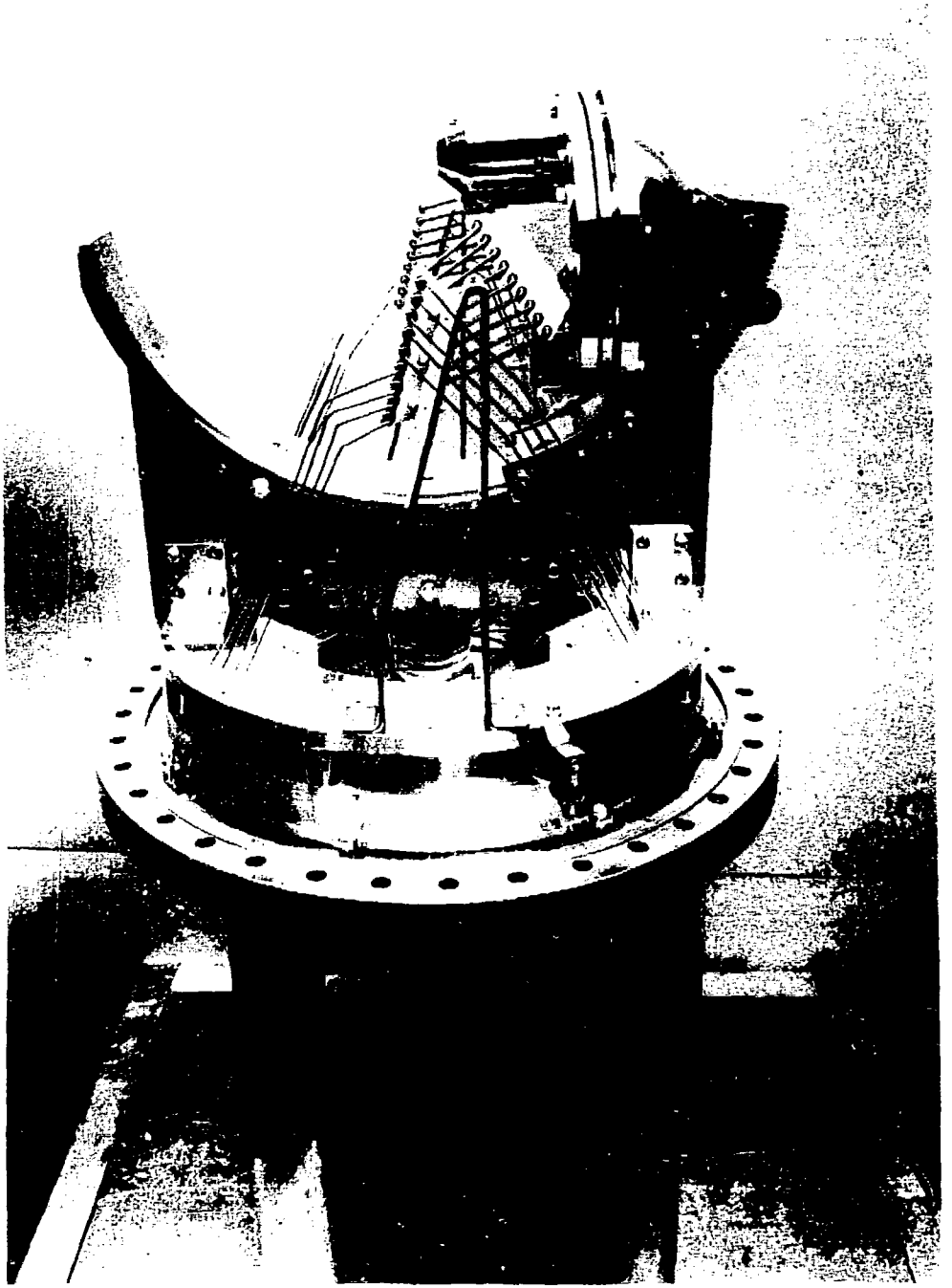

CBB 785-5300

Figure 6

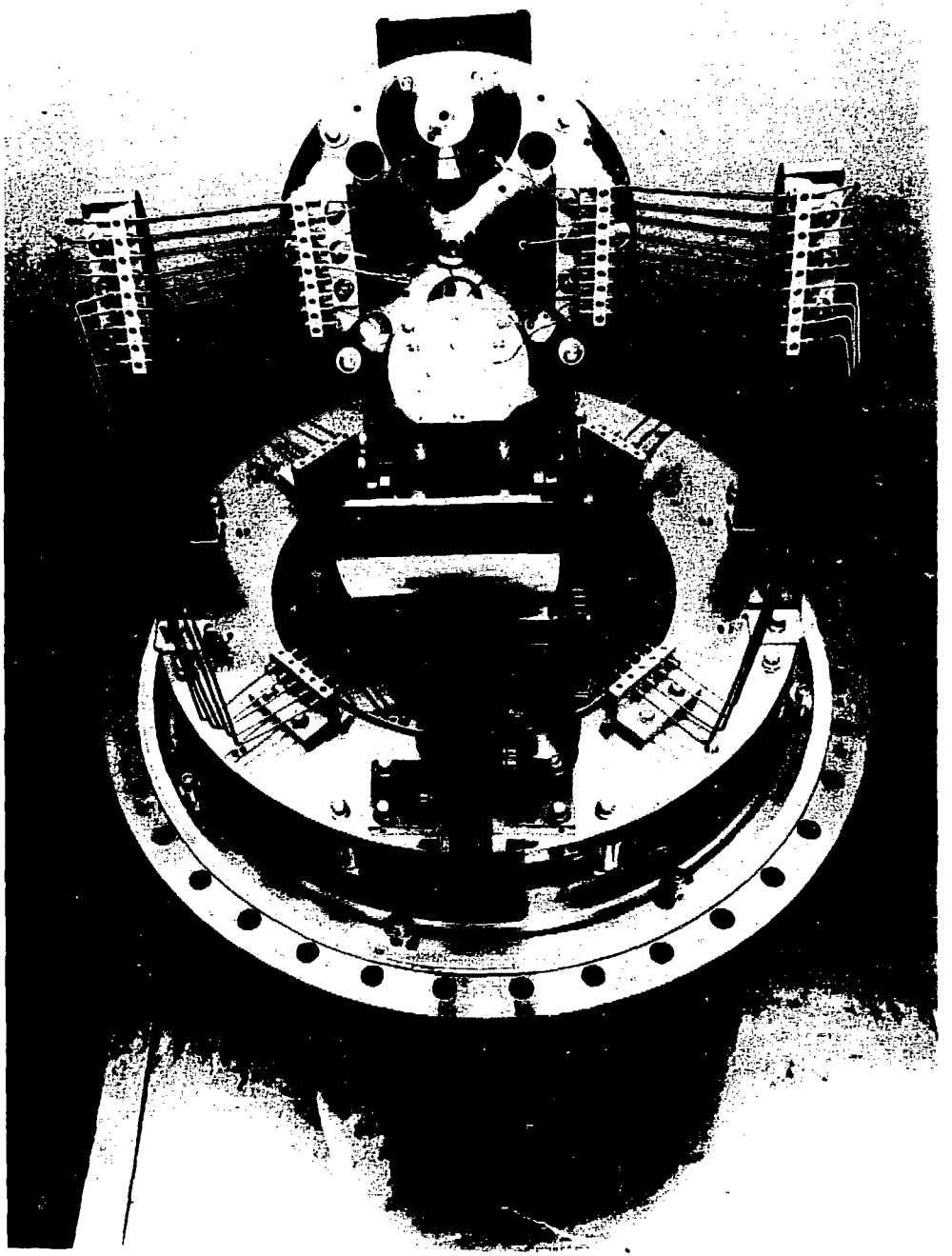

CBB 785-5304

Figure 7

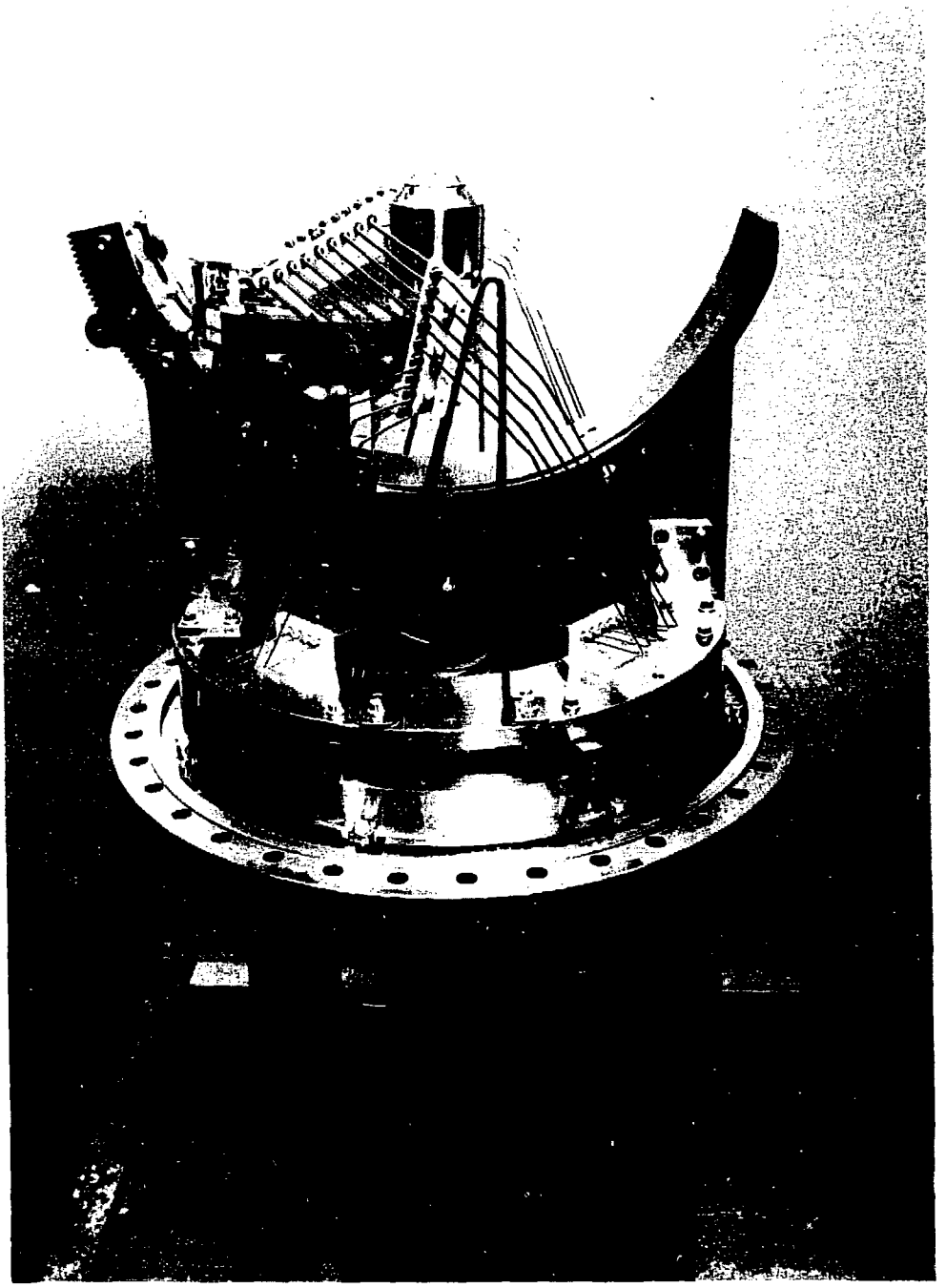

CBB 785-5302

Figure 8

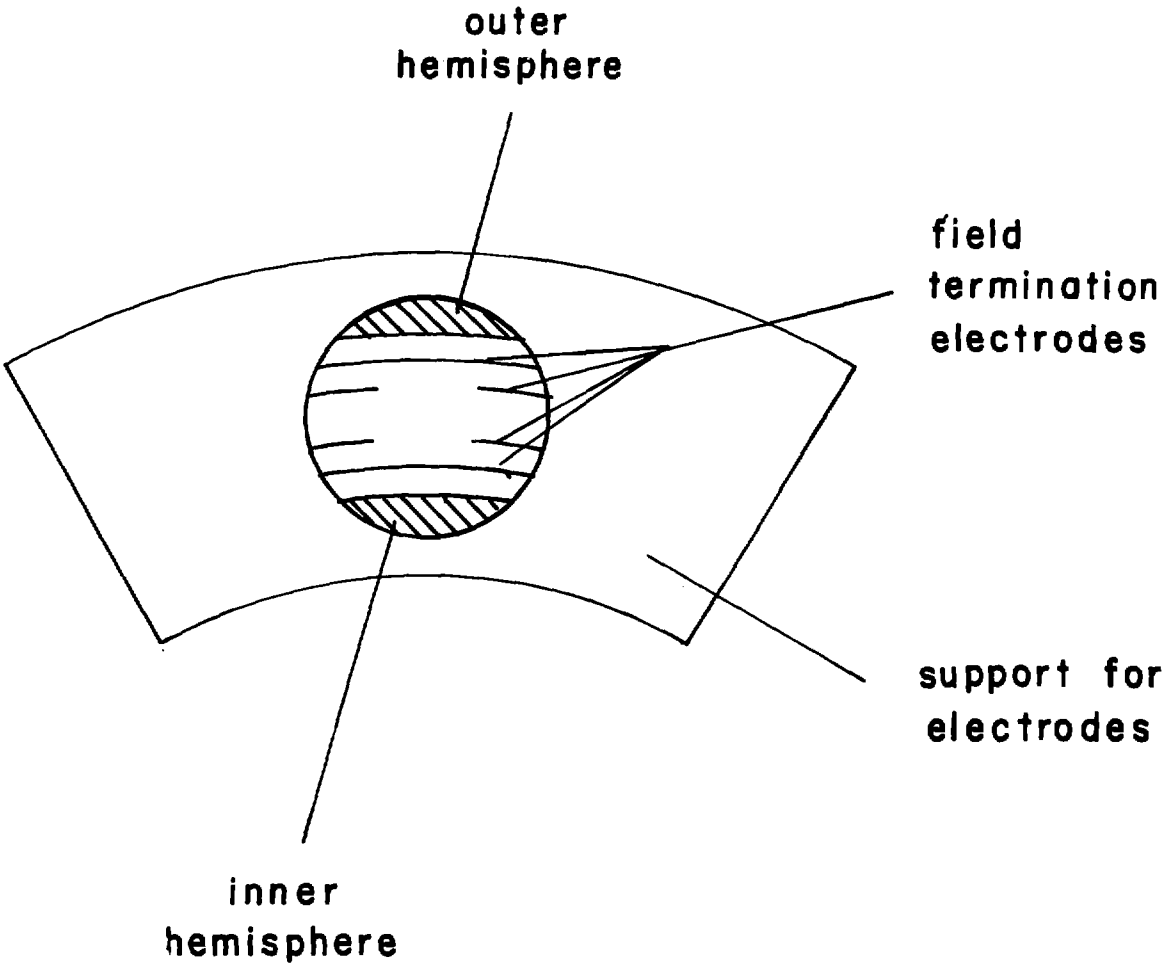

XBL 806-9949

Figure 9

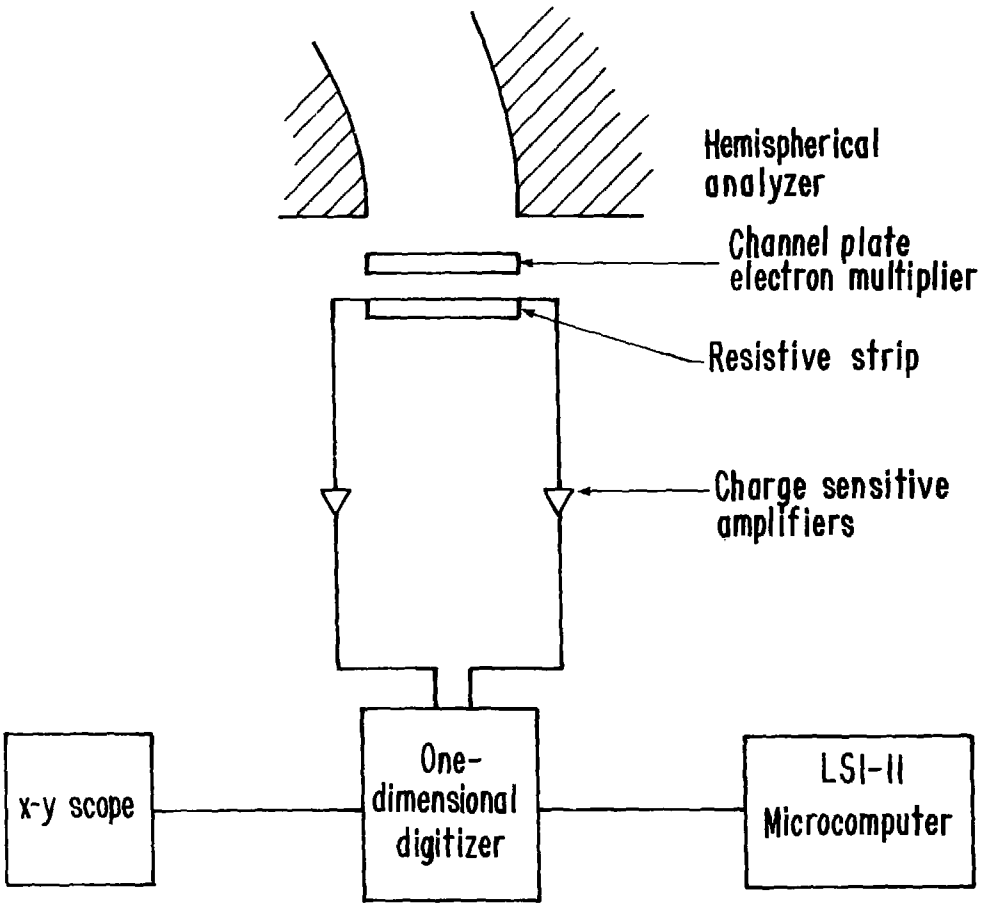

ARPES Detector electronics

XBL7810-6548

Figure 10

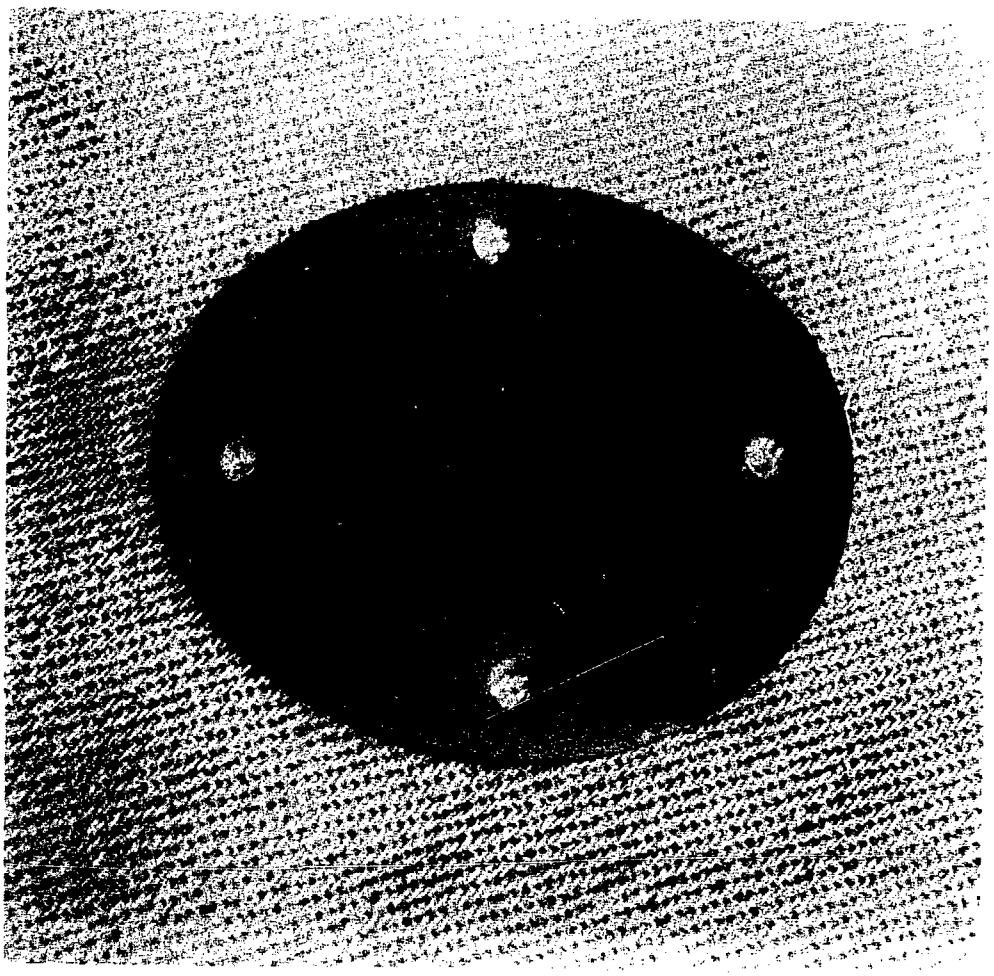

CBB 803-3538

Figure 11

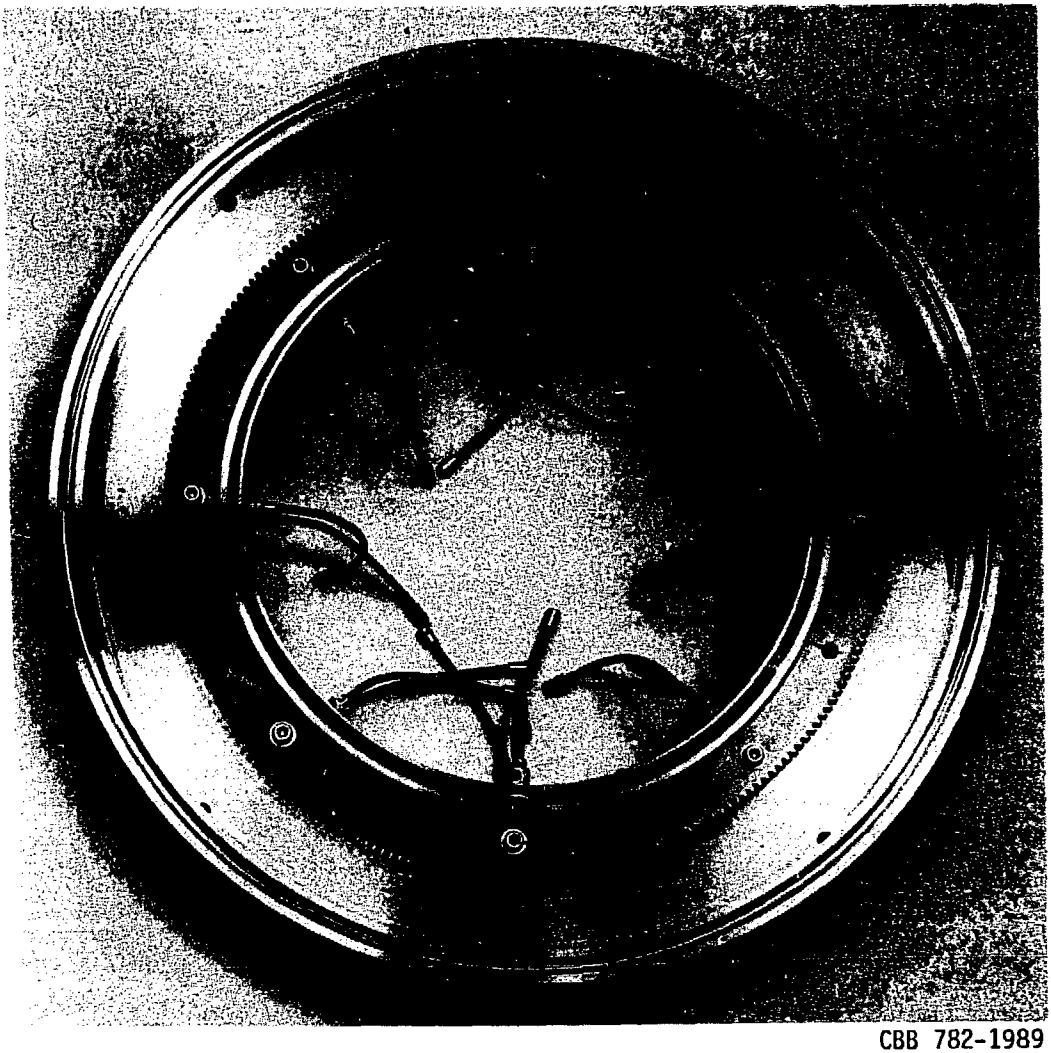

CBB 782-1989

Figure 12

CBB 782-1983

Figure 13

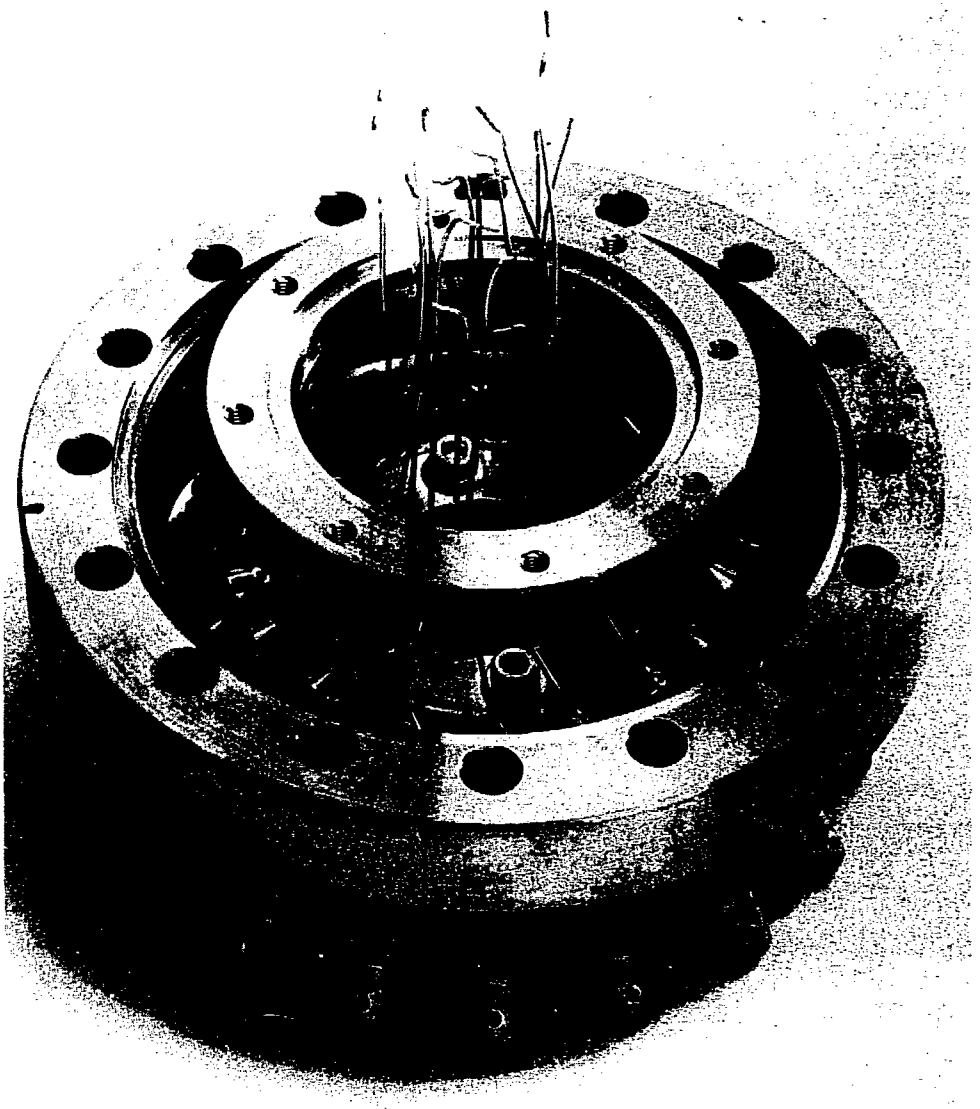

Figure 14

CBB 782-1981

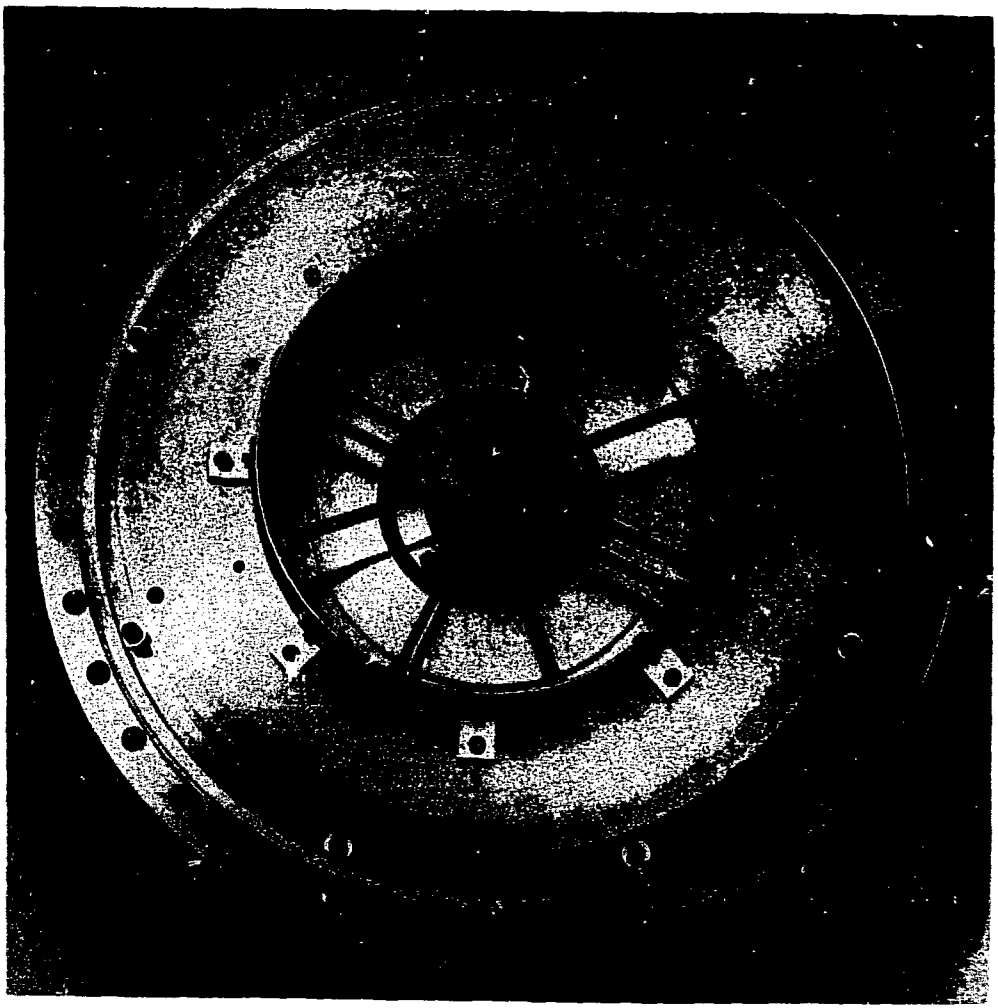

CBB 782-1985

Figure 15

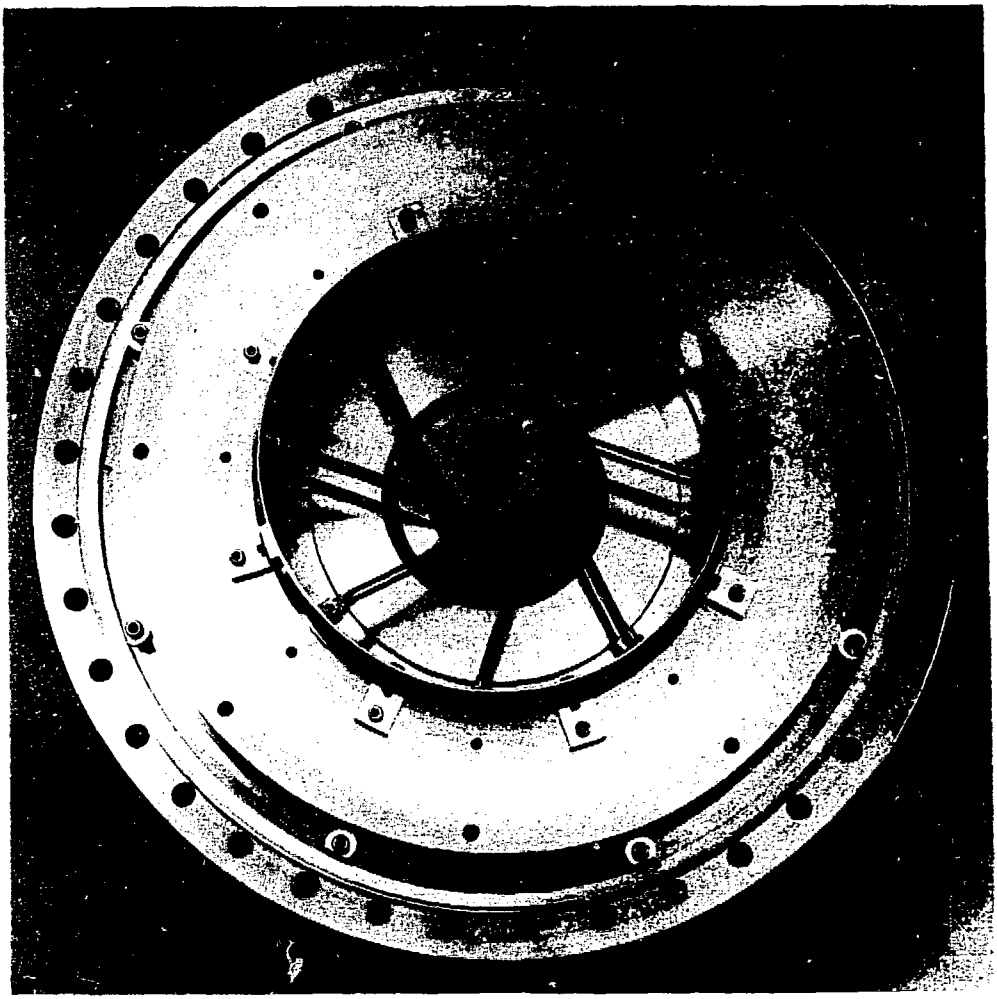

CBB 782-1987

Figure 16

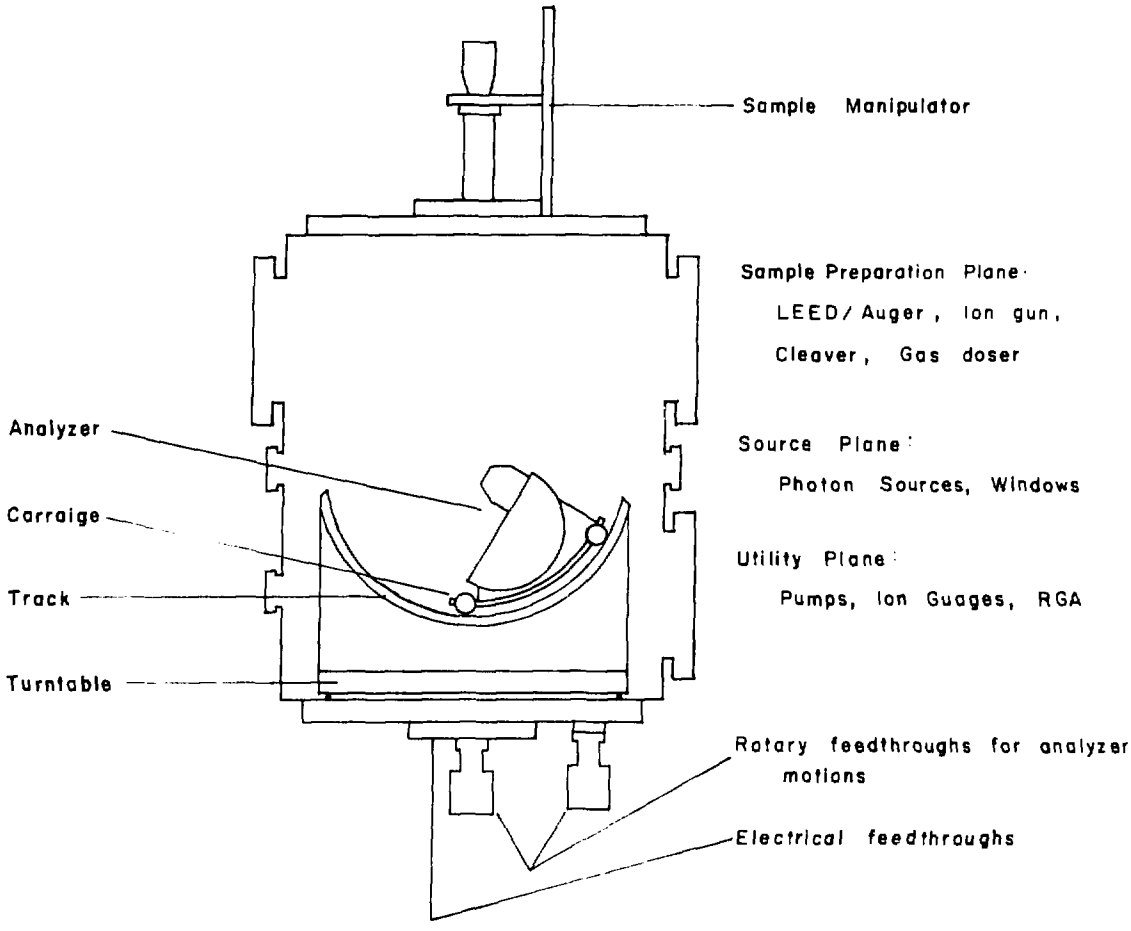

XBL 806-9960

Figure 17

Digitizer Circuit Schematic

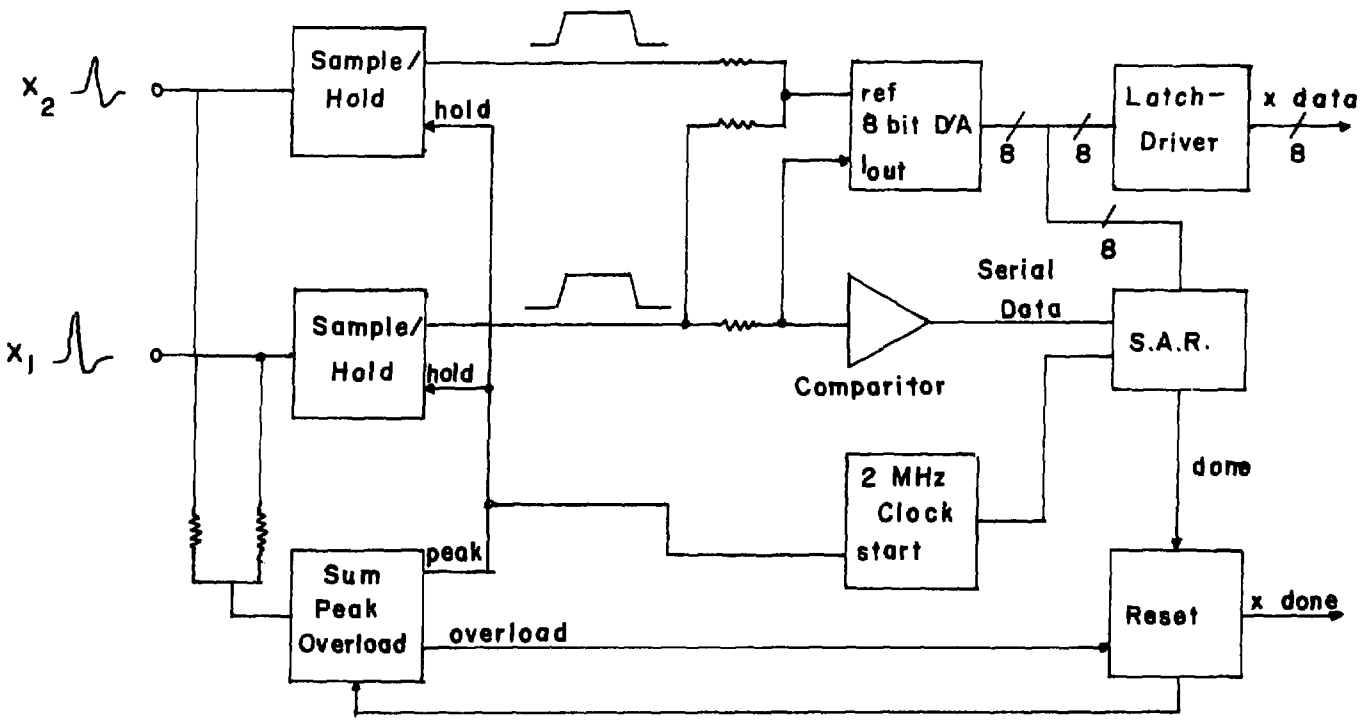

XBL 806-9966

Figure 18

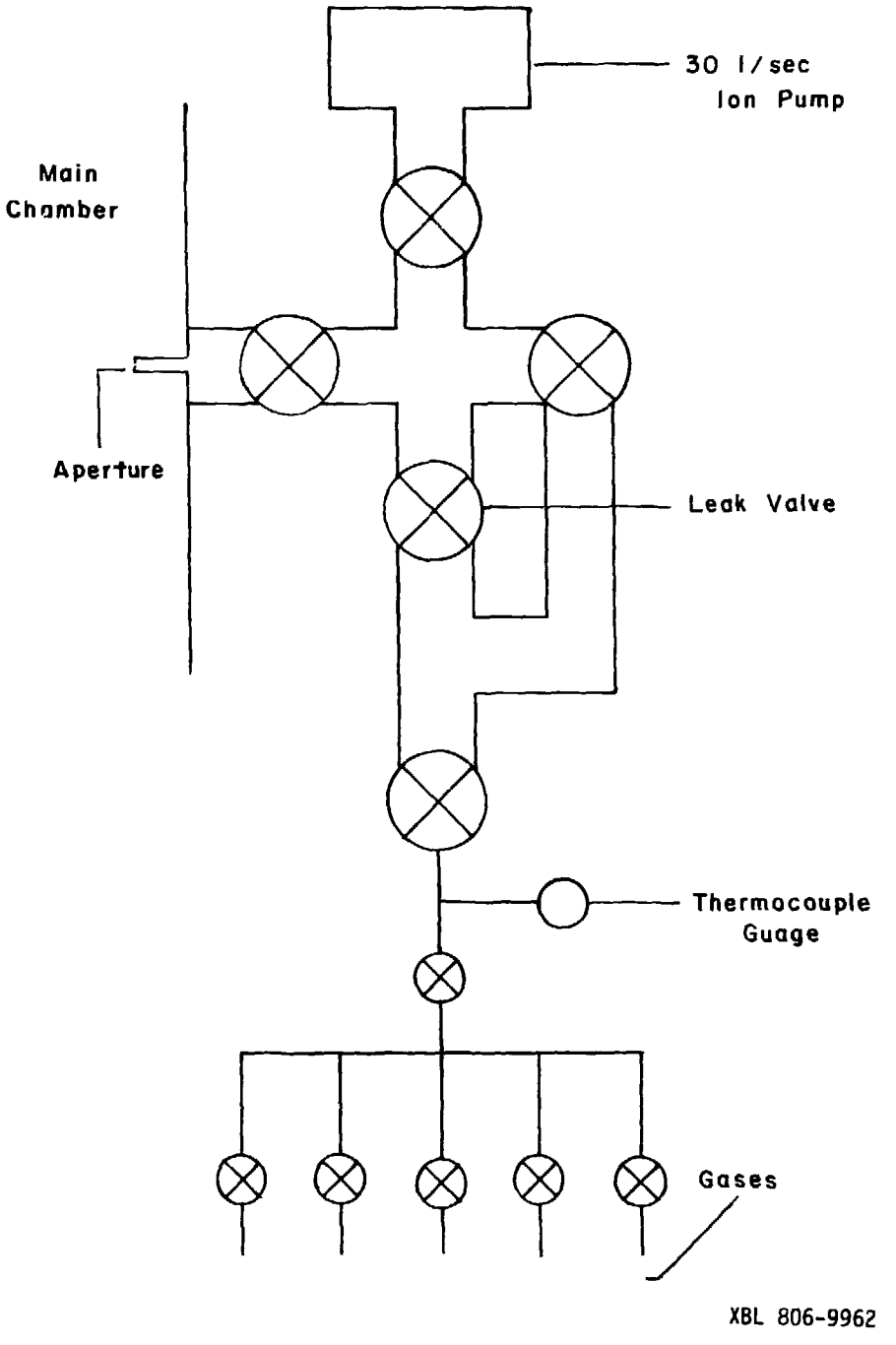
30 l/sec
Ion Pump
Main
Chamber
Aperture
Leak Valve
Thermocouple
Guage
Gases
XBL 806-9962

Figure 19

III. RESULTS AND DISCUSSION

As outlined in the introduction, the goal of the experiments described in this thesis has been to characterize the application of photoelectron diffraction to surface structure determination. Clearly, it is a good idea to test a new structural technique by studying model systems of known structure. Ordered chalcogen overlayers on the low Miller index faces of nickel have been studied by numerous techniques and, in several cases, reasonably accurate structures have been determined by LEED. For this reason, we have initiated our effort using these systems. The Se/Ni(001) system was studied first because it is generally accepted that selenium bonds in the fourfold coordinated hollow site,[1] and also because the Se(3d) core level at a binding energy of 57 eV is well placed and gives good intensity for the purposes of cross-section measurement. The overall plan, then, was first to use that system to observe the PhD effect and to yield a preliminary characterization of the structural sensitivity of photoelectron diffraction. We then performed experiments on other chalcogen-nickel systems to check conclusions derived from the Se/Ni(001) system.[2] Finally, we undertook the study of some less well-characterized molecular overlayer systems with which LEED has had some difficulty in the past.

Before beginning the description of experiments, the author would like to point out that the technique of photoelectron diffraction is still in its infancy. By this I mean that very few systems have been studied. While there is cause for some enthusiasm, the literature is

filled with descriptions of "promising new techniques" which have been subject to infant mortality. While it is obviously my hope that photoelectron diffraction will find its place as a surface structural tool, it must stand the test of time and of many more experiments than those described in this thesis.

A. The model system: Se/Ni(001)

In Fig. 1 we show a wide band energy distribution curve N(E) (EDC) of the c(2X2) Se/Ni(001) system which exemplifies our reasons for choosing this system first. The photon energy of 150 eV, for which the kinetic energy is about 100 eV, is the region where there is normally a good deal of monochromatic flux emanating from the grasshopper monochromator. The Se(3d) level manifests itself as a large peak at 57 eV binding energy relative to the Fermi level. That a half monolayer of selenium contributes to the elastic photoemission signal nearly as much as the substrate itself is due both to the short electron mean-free-path in this energy range as well as the inherently good cross-section of the 3d level. Note that the peaks in Fig. 1 measure elastic (or at least quasielastic) photoemission intensity, and hence originate from the top few layers. The broad continuous background arises from inelastic processes and is characteristic of photoemission spectra in general.

The EDC shown in Fig. 1 is taken for electron emission normal to the surface so that if the cross-section of the three peaks were to be measured as a function of photon energy, a normal photoelectron diffraction (NPD) curve could be generated for each level. The

clearest demonstration of the NPD effect is shown in Fig. 2 where a set of EDC's for the p(2X2) Se/Ni(001) system is plotted together in three-dimensional photon energy-binding energy-intensity space. The various EDC's have been adjusted for incident photon flux and analyzer transmission as explained earlier. Oscillations in peak intensity in the Se(3d) level as well as in the substrate 3d and 3p levels are clearly visible. These oscillations cannot be due to any atomic effects, since the atomic cross-sections are expected to be smooth in this energy range.[3] They must therefore be manifestations of final state inteference effects or photoelectron diffraction.

If one takes a cut through the three-dimensional surface in Fig. 2 at binding energies for the three peaks, one generates the more standard cross-section vs. kinetic energy curves shown in Fig. 3. The semblance to LEED intensity vs. voltage curves is obvious, except that the region near zero kinetic energy is inaccessible due to the large photoemission inelastic tail combined with the small atomic cross-section. It is interesting to note that the substrate levels, even the "delocalized" valence band, show diffraction effects as well as the overlayer. The theoretical interpretation of these substrate PhD curves would be difficult due to the multilayer initial states, but if such a treatment were performed, structural information in the form of a nickel lattice constant would probably be available. These data are clearly not particularly interesting in this case, and I leave the subject of substrate diffraction effects at this point noting only that ARP intensities cannot be accurately calculated from crystalline

materials to accuracies better than 30 percent without including multiple scattering effects. Similar results have been reported in recent azimuthal photoelectron diffraction studies.[4]

Of much greater interest in this thesis is the Se(3d) cross-section curve from which we wish to derive structural information. Tong and Li have recently calculated the Se(3d) emission intensity as a function of kinetic energy for the experimental geometry and coverage of Fig. 2.[5] Some of their results are shown in the top three curves of Fig. 4. Before making comparisons to our experimental curve, there are several interesting features in the calculated results themselves. The three curves correspond to different values of the parameter $d_\perp$, defined as the interplanar spacing between the outermost nickel layer and the selenium layer. If one fixes $d_\perp$ in the calculation and varies the lateral position of the selenium layer relative to the nickel surface, the calculated results change slightly in that the relative intensities of the peaks in the cross-section curve vary somewhat, but the peak energy positions are remarkably constant to within a few eV. This result is shown in Fig. 5 for $d_\perp$ values of 2.34 and 1.55 Å. On the other hand, as evidenced in Fig. 4, the peak positions and intensities are very sensitive to $d_\perp$. Specifically, there is a systematic shift of the peaks to higher kinetic energy as $d_\perp$ decreases. This observation is characteristic of interference phenomena in general. The similarity to EXAFS oscillations is obvious, except that here the determining parameter is $d_\perp$ rather than nearest neighbor distance. If one assumes a fixed nickel-selenium bond length, then $d_\perp$

is directly related to surface structure. For instance, if the selenium atoms bond directly on top of the nickel atoms (atop site geometry), the value of $d_\perp$ derived by adding the covalent radii of selenium and nickel would be 2.34 Å. On the other hand, if the four-coordinated hollow site geometry is preferred, $d_\perp$ is reduced to 1.55 Å. These results are summarized in Fig. 6. The two-coordinated bridge site and an infinite number of other asymmetric site geometries would correspond to intermediate values of $d_\perp$. Clearly the assumption of using covalent radii can be relaxed if a symmetric adsorption site is preferred, since the three $d_\perp$ values for the atop, bridge, and hollow sites are widely separated and well within our experimental accuracy.

Let us now compare the theoretical curves to experiment. The first thing one observes is that the experimental peak intensities are not particularly well matched by any of the theoretical curves. The predicted peak-to-valley oscillation amplitude is as much as a factor of five, while the experimentally observed oscillation is a factor of two. This descrepancy could be due to several experimental factors such as finite sample temperature, finite spectrometer angular resolution, and an atomically imperfect surface in which not all selenium atoms are in similar environments. In any case, the problem of oscillation amplitude is not of major concern; it is typical of LEED and EXAFS studies as well. Of greater concern is that the relative peak intensities are not well fitted. Again, there are experimental factors which could explain this: unstable photon flux over the period of the experiment (as much as severl hours) and problems with

correcting for the photon flux and analyzer transmission. As explained in Chapter II, these problems could give rise to smooth errors in our data which would disturb the match to theoretical intensities. In addition to these experimental problems, there is the theoretical problem of accurately calculating atomic photoionization cross-sections in open shell systems. Such problems continue to occupy atomic theorists.[3,6] For these reasons, one would not necessarily expect to match accurately the peak intensities in our NPD curves. On the other hand, the systematic way in which the calculated peak positions shift as a function of $d_\perp$, the insenstitivity of the energy peak positions to smoothly varying errors, and the fact that the oscillatory part of the PhD calculatons is on a reasonably firm base all indicate that a match to the peak energy positions alone (aside from a uniform shift of 2-3 eV due to the usual uncertainties concerning the inner potential) might enable extraction of structural information in spite of the misfit in peak intensities. Such does indeed seem to be the case in this system; the peak positions of our experimental data are accurately matched by those in the curve calculated for $d_\perp = 1.55$ Å, the value derived from previous LEED studies.[1]

This observation is tempered by the misfit in the region 0 eV$\leq$ KE $\leq$ 50 eV, where the match in peak position is marginal. This seems to be the case in most of the systems we have studied, especially in the case of 3d levels which experience a delayed onset in atomic cross-section, and is probably an artifact of computational and experimental difficulties at those low kinetic energies. The

theoretical results become very model-dependent in this lower energy regime, being greatly affected by changes in atomic-scattering phase shifts as well as by differences in the treatment of the photoionization step and central atom potential.[7] Misfits in the first 50 eV above the edge are familiar from EXAFS studies where that energy range is neglected in all simple treatments.[8] Apparently, the theoretical difficulties with this energy range will make it less useful in PhD surface structure determinations. The importance of working to higher kinetic and photon energy cannot be overemphasized.

The apparent insensitivity to absolute registry is of interest. The observation that NPD is senstitive to $d_\perp$ alone indicates that for a complete structural determination a combined surface EXAFS - NPD effort might be in order. The nearest neighbor distance is the most readily available parameter in EXAFS, and its combination with $d_\perp$ will lead to a precise structural determination. The exact reason for NPD's insensitivity to absolute registry is as yet uncertain but an interesting hypothesis is available. The observation tends to imply that the 180° backscattered wave is the dominant contribution to the NPD final state. In this case no lateral sensitivity would be expected. More credence is lent to this single beam idea when one considers that the 00 LEED beam is usually 4-5 times more intense than the other beams. One might in fact expect the NPD curve to show some semblance to the 00 beam. Such comparisons must be made with some caution, however, since the NPD process is coherent and one really wants to compare amplitudes, rather than LEED intensities. In any

case our NPD data are shown in Fig. 7 along with the LEED 00 and 01 beams published by Demuth and Rhodin.[9] In this system, the general structure and peak position of the NPD curve is similar to that seen the 00 beam. While the comparison is of some interest, in general the situation is more complicated and the rest of the NPD data in this thesis show little semblance to the corresponding LEED 00 beam. This of course does not refute the idea that the directly backscattered wave is the dominant contribution to the NPD final state. More will be said concerning NPD's sensitivity to d_1 in the next chapter.

At this point a preliminary estimate of the accuracy of d_1 as determined by NPD is of interest. This estimate must be preliminary because only a very limited set of data and of theoretical curves is available. For the same reason it must be conservative. I note a typical peak energy reproducibility and match to theory for this and other data of ±1.5 eV, and an rms shift of 50 eV/Å in the peak positions calculated by Tong and Li (Fig. 4) between the two-fold bridge and four-fold hollow site geometries. Division yields ±0.03 Å. On this basis it is realistic to estimate the error of NPD as ±0.05 Å in d_1, which compares favorably with LEED accuracies. As the NPD experimental and theoretical techniques are improved and in particular as the energy range of NPD experiments increased, it is not unreasonable to expect the accuracies of ±.01-.02 Å, more typical of EXAFS studies. Some recent calculations indicate that at higher energies, peaks disperse at rates in excess of 100 eV/Å.[5,10] The importance of working to higher energies is seen to be very important. As explained

in Chapter I, the improvement in accuracy over those typical of LEED studies would be due to the greater degree of coherence in PhD and also to its localized nature relative to LEED.

After this initial encouraging result, we wished to use the Se/Ni(001) system to characterize further the photoelectron diffraction process. The easiest and perhaps most obvious question to answer concerns the polarization dependence of our NPD curves. The polarization vector of the incoming light enters the PhD process only in the photoionization step through some sort of generalized asymmetry parameter familiar from gas phase photoelectron spectroscopy.[3,6] In this oriented crystalline system, the usual equation governing the polarization dependence of gas phase photoelectron spectroscopy is not expected to be rigorous but, for simplicity, if we assume that the emission intensity from the core state is peaked along the polarization vector, it is clear that we should be able to change the relative contributions of the various LEED beams to the superposition which forms the photoemission final state. These changes might be expected to manifest themselves as changes in both the peak position and intensity.

Figure 8 shows all of our NPD results on the c(2x2) Se/Ni(001) system. The top two curves are taken for identical experimental geometries, but during different running periods using different Ni(001) crystals. Remarkably consistent results are obtained. Peak positions are identical to within 1 eV usually, and the peak intensities are quite similar. The third curve demonstrates the effect of

changing the angle of incidence to 80° along the same [100] azimuth, so that the macroscopic A vector is only 10° off normal. There is a small shift in peak positions and intensities. Finally, curve d shows the effect of changing the azimuthal incidence of the light to the [110] azimuth. The general shape and peak structure of all four curves is observed to be quite similar. I conclude that at the level of accuracy with which the curves in Fig. 8 were measured, the peak positions and intensities are quite reproducible and are not particularly sensitive to the azimuthal or polar orientation of the photon polarization vector of the incident radiation in the energy range we have studied. A tabulation of the peak positions in these curves is included in Table I. The polarization changes included in Fig. 8 are relatively minor. However, calculations predict little effect in making the rather substantial change from p- to s-polarization.[9,10] This lack of sensitivity to the polarization vector implies that the relative contributions of the various beams to the NPD final state is not particularly important in determining the NPD peak intensity positions.

There is another pleasing common characteristic of the four curves in Fig. 8. If the diffraction maxima and minima could be eliminated by some sort of averaging process, the remaining curves would have the functional form expected for the energy dependence of the photoionization cross-section for a nodeless 3d initial state. That is, the intensity would rise slowly above threshold due to the delayed onset, reach a broad maximum centered about 100 eV above threshold, and then

decrease.[3] This observation supports the view of photoelectron diffraction given in the introduction as a two-step process. There is first an atomic-like excitation followed by scattering in the final state which introduces intensity oscillations as a function of energy. The photoemitting atom acts as an electron gun, with an "emission current" given by the atomic cross-section. The observed intensity oscillation can then be taken as a product of an atomic cross-section term $I_0(h\nu)$ and an oscillatory function $(1+f(h\nu))$ which describes *final state scattering:*

$$I(h\nu) = I_0(h\nu)(1 + f(h\nu)) \quad .$$

The cross-section is written in this way to emphasize the relation to EXAFS oscillations. This picture is consistent with recent theoretical predictions that initial states possessing radial nodes exhibit NPD curves with one major sharp peak, the position of which is insensitive to d_1.[12] The peak is merely an artifact of a Cooper minimum in the atomic cross-section, which sharply attenuates the cross-section a few hundred eV above threshold, and keeps it at a low value for a long range of energy.[3,6] Although the diffraction oscillations are expected to be present at higher energies, they will be difficult to observe because the entire elastic peak in the photoemission spectrum will be very weak and will be obscured by noise arising from the inelastic background. It is clearly advantageous to use core levels with nodeless initial states for NPD studies in order to simplify the separation of atomic from scattering effects.

Liebsch showed that this separation into atomic and scattering effects is only rigorous for s initial states.[11] In this case, in the non-relativistic limit, the wave emitted from the atomic core has only the L = 1 p partial wave component.[13] For higher angular momentum initial states both the $\Delta L = +1$ and $\Delta L = -1$ partial waves contribute and the separation into atomic and scattering contributions is made non-rigorous by interference between these partial waves. When one wave dominates the cross-section, the separation is a good approximation. This is the case for nodeless initial states away from threshold (KE $\geq$ 30 eV),[3] and a two-step model is a good approximation for the Se(3d) level throughout most of the energy range we have studied.

The same is clearly not true in a recent NPD study reported on the c(4x2) Te/Ni(001) system.[14] In that effort, the cross-section of the Te 4d level was measured and a smooth, but not experimentally derived, atomic cross-section was divided out with the intention of obtaining the final state scattering contribution. The data were accumulated at and below the Cooper minimum where the rapidly changing relative contributions from the p- and f- partial waves produce a pathological atomic background. The authors found rather poor agreement with recent calculations by Tong and Li[12] and concluded that the structural sensitivity of NPD was suspect. Their study contains several features which make that conclusion erroneous, the worst of which was the assumption of separability of atomic and scattering components for the 4d initial state in the energy range in which they were working.

To provide a further characterization of constant-initial-state photoelectron diffraction, off-normal emission studies of the c(2x2) Se/Ni(001) system were also carried out. In Fig. 9a, I show results for emission into the $(\bar{1}00)$ mirror plane at various polar emission angles, while Fig. 9b shows similar data for emission into the $(0\bar{1}\bar{1})$ mirror plane. The curves are rich in structure, and if they could be interpreted quantitatively, they would probably yield a good deal of information. It is also clear that the intensity modulations are not nearly as pronounced off normal as they are at normal emission. Indeed, at some angles little structure is observed at all. This can be understood as arising from the reduction in symmetry of the off-normal final states and the consequent removal of degeneracies in the various time-reversed LEED beams contributing to the final state. This is probably also one reason for the smaller oscillations observed in the APD studies.[15] In contrast to the behavior of the LEED 00 beam, there is no obvious systematic shift of peak energies with polar emission angle. In fact the curves seem to evolve more by reduction in the intensities of some peaks and increases in others. The curves in Fig. 9 were taken at a rather coarse angular mesh and do not represent as complete a study as would be desirable. A more complete study is needed to assess more thoroughly the information contained in off-normal photoelectron diffraction curves.

One of the original incentives for these off-normal studies was to explore whether the intensity-voltage curves become simple at particular non-zero combinations of the polar and azimuthal emission angles.

For example, the combinations of (45°, 180°) and (54°, 225°) correspond to emission normal to the ($\bar{1}01$) amd ($\bar{1}\bar{1}1$) planes, respectively. Some sensitivity might be expected in these curves to the d_1 values of overlayer selenium relative to these two planes, although complicating factors abound; e.g., low symmetry, energy dependent refraction, etc. In fact no obvious relationships between the forms of the off-normal curves in Fig. 9 and the known adsorbate-substrate geometry are noted. This question must be left open pending further experimental and theoretical work. There is, however, one unexpected feature of the off-normal curves that deserves comment. The three lateral pairs of curves in Fig. 9 show a fair degree of resemblance to one another. This is most pronounced in the middle pair, whicn is also the pair which shows the largest modulation. In Fig. 10 these two curves are compared on a common energy scale. Several of the most prominent peaks fall at similar energies, with similar intensities, in the two curves. The pairwise similarity of the curves in Fig. 9 for similar polar but different azimuthal angles suggests in a very tentative way that the polar angle alone may be the critical variable in determining the structure in the PhD curve. This would be true, for example, if the substrate surface were effectively an isotropic scattering plane. It should be noted that the curves in Fig. 9 are not normalized to each other so that the above observations make no implications about azimuthal photoelectron diffraction studies.

We wished next to characterize the application of NPD to disordered overlayer systems. In the introduction I argued that PhD

should not be limited to the study of overlayer structures which are ordered on the LEED scale. Figure 11 presents data which indicates that this is indeed the case. The top curve in Fig. 11 shows NPD data for a coverage of approximately 0.1 monolayer, while the middle curve shows data for 0.2 monolayer. Neither surface gave a LEED pattern indicative of an ordered overlayer, but both show substantial photoelectron diffraction effects. Indeed, the amplitude of oscillation is nearly as large in these two disordered overlayers as in the bottom curve, which shows the c(2x2) results for comparison. The similarity of these three curves to each other and to the previous p(2x2) results indicates that NPD is not particularly sensitive to the degree or type of order in the overlayer itself.

The significance of this result should not be underemphasized. It shows first that the dominant scattering mechanism in NPD is definitely off the substrate and not off the overlayer itself; otherwise the effect in the disordered overlayer would not be so large. It also confirms the claim made in the introduction that NPD, like EXAFS, can deal quite effectively with two-dimensionally disordered overlayer systems which are common in surface studies. Again, the localized nature of PhD relative to LEED is evident. This is a significant advantage over LEED, in which 00 beam intensity variations are the only changes useful in making a structural determination on disordered overlayers. The application of NPD to systems possessing three-dimensional disorder (multiple binding sites) will be discussed in the next section.

It is of further interest to compare these results to recent azimuthal photoelectron diffraction (APD) studies of disordered overlayers. There has been some discussion concerning the structural sensitivity of APD. In some cases, the calculated APD patterns show little dependence on d_1 or any other parameter describing overlayer-substrate geometry.[5] Indeed, in these cases, essentially the same APD pattern is calculated for a monolayer of adsorbate species isolated in space, implying that the dominant scattering mechanism is clearly within the overlayer itself, in obvious contrast to our NPD results. On the other hand, for other photon energy-polar emission angle combinations, substantial sensitivity to adsorbate-substrate structure has been observed and used. Recent experimental APD results on low, disordered coverages of iodine adsorbed onto Ag(111) indicate that the APD pattern is generally reduced in modulation intensity for the disordered overlayer relative to ordered overlayer results, and also that the two patterns do not show the same general features.[16] Both of these observations are different from what we have observed in the NPD case, and are consistent with the idea that APD is generally more sensitive to order in the adsorbate layer and less sensitive to adsorbate-substrate geometry than NPD. I leave this as an empirical and interesting observation which requires further experimental and theoretical study for a complete explanation.

The final aspect of interest concerning the Se/Ni(001) model system was the effect of temperature. It is hypothesized that PhD studies might be particularly sensitive to temperature due to the

vibrational motion of the photoemitting species. In view of the fact that several theories predict substantially enhanced vibrational motion of the surface layer relative to the bulk layers, its surface-localized nature makes the PhD technique potentially more sensitive to temperature than LEED and also potentially more useful in studying surface vibrations.

The treatment of the temperature dependence of PhD data has received little theoretical attention. Tong and Li include temperature effects in their PhD calculations in much the same way as is done in LEED calculations. The T-matrix describing the final state scattering is made temperature dependent[17,18] so that the amplitude scattered into each beam of the final state is a monotonically decreasing function of temperature. The effect of vibrational motion on d_1, however, is neglected. The functional form of the temperature dependence of LEED I-V curves is experimentally found to be exponential,[19] implying that the intensity is governed by a Debye-Waller factor:

$$I \sim \exp - \langle(\Delta\vec{k}\cdot\Delta\vec{r})^2\rangle$$

with $\Delta\vec{r}$, the instantaneous displacement the surface atoms. A similar result is familiar in x-ray diffraction studies.[20] Unfortunately, the effective Debye temperature determined in such an analysis of LEED data is a function of $\Delta\vec{k}$, indicating that multiple scattering precludes any simple theoretical framework.[19] The apparent lessening of the importance of multiple scattering in PhD implies that a simple

Debye-Waller treatment might be a better approximation, especially at higher energies.

The neglect of the vibrational motion on $d_\perp$ is probably one of the main reasons for NPD's amplitude mismatch between experiment and theory. The effect of the $d_\perp$ vibrational distribution on the NPD amplitude is analogous to the effect of temperature on the EXAFS amplitudes. The latter has been shown theoretically[21] and experimentally[22] to follow a Debye-Waller functional form. One might expect a similar effect in PhD.

There are only a few experimental and theoretical studies of the effect of temperature on angle-resolved photoemission. Shevchik showed theoretically that, using an augmented-plane-wave final state and a tight-binding initial state, the direct transition amplitude from ARP studies of valence bands should follow a Debye-Waller functional form.[23] Subsequent experimental studies have attained a reasonable amount of success in applying his result, although two studies noted an anomalously non-linear effect at higher temperature.[24-26] This could be an indication of enhanced surface vibrational amplitudes, or else of problems in the application of the Debye-Waller functional form. The applicability of such a simple formalism as Shevchik's to PhD studies is at best dubious.

With these thoughts in mind, we undertook to measure the NPD curves of the c(2x2) Se/Ni(001) system as a function of temperature between 120K and 800K. Three of the resulting curves are shown in Fig. 12. Only the region between 130 eV and 210 eV photon energy was

measured for most of the temperatures in order to speed the acquisition process, since this is the region where the best statistics are most easily attained, and also since this is the region where one partial wave dominates the atomic excitation step. The effect of temperature is seen to be large, as expected. It is interesting to note that the loss of contrast is most pronounced at higher energies, in qualitative agreement with the form of the Debye-Waller factor. In order to treat the data numerically, one wants to produce an EXAFS like plot of $(I-I_0)/I_0$, where I_0 is the atomic contribution. As explained earlier, it is a reasonably good approximation to separate the intensity into atomic and scattering contributions for the 3d initial state in this energy range. In practice, the separation is not straightforward. The atomic contribution can be determined in different ways, but the results here are rather insensitive to the details of the technique as long as the various curves are treated consistently.

I have linearly scaled the curves so that they all intersect to within one volt of 142, 159, 186, and 210 eV photon energy, and determined a smooth background through these points which also smoothly joins the high and low energy data taken at T = 120K and T = 300K. The resulting plots of I_0 are shown as dashed lines in Fig. 12 and actually resemble one another closely, providing a good self-consistency check. Plots of $(I-I_0)/I_0$ for these temperatures are shown in Fig. 13, and a dramatic effect is again observed. Unfortunately, the subtraction of two nearly equal numbers (I and

I_0) at high energies leads to rather substantial (not explicitly shown) error bars on these curves.

In Fig. 14, I show the dependence of $\ln (I-I_0)/I_0$ on temperature for the two photon energies corresponding to the peaks in Fig. 12. Aside from the substantial random uncertainties shown, an approximately linear plot is obtained. The same result is obtained at the photon energy corresponding to the minimum at 174 eV photon energy. If effective Debye temperatures are derived from the slopes of linear least squares fits of these data, the results are θ_D = 135K, 124K, and 133K for photon energies of 149, 174, and 192 eV, respectively. there are several points of interest. First, the fact that the plots are fairly linear implies that some simple model might be derived to explain the results. Of course, logarithmic plots are not a very sensitive way of proving a functional form. The second general comment is that the effective Debye temperatures are all rather low compared to typical bulk Debye temperatures. This is consistent with the idea of enhanced surface vibrational motion. Finally, and perhaps most interestingly, the effective Debye temperatures for the three photon energies are, within statistical errors, identical. Such is not the case in LEED studies. Further work on other systems is needed to support these conclusions, but if they are valid, NPD might be valuable technique for studying surface vibrational characteristics.

B. Other Se, S/Ni systems

The initial encouraging results on the Se/Ni(001) system led us to extend our studies to other chalcogen overlayers on low Miller index

nickel surfaces. For the reasons outlined in Chapter II, Section A, we were not (until recently) able to study oxygen overlayers because the only good core level, the O(1s), is too tightly bound to be studied under normal operating circumstances. In addition, the experimental problem of the Cooper minimum on the Te(4d) cross-section led us to avoid that adsorbate as well. Neither constraint should be binding in the long run when better photon sources become available. We were left with studying selenium and sulfur overlayers. The binding energy of the S(2p) spin-orbit split doublet (164, 166 eV) is reasonably well placed for our purposes.

The first system we studied was the c(2x2) S/Ni(001), and the experimental results are shown in Fig. 15 along with calculations by Tong and Li.[10] The structure of the experimental curve is similar to that seen in the selenium case, although the peak positions are somewhat different. The similarity is not surprising when one considers that the binding site for sulfur and selenium is the same, and $d_\perp$ differs by only .2 Å. The best fit to theory is for $d_\perp$ = 1.30 Å, in good agreement with the accepted value.[1] In this case, the fit to peak intensity is also rather good with the exception of the lowest energy peak. The intensity of that peak is very sensitive to non-structural parameters dealing with the atomic excitation step.[10] It is interesting to note that for this p-level, the fit at lower energies is somewhat better than it was for the selenium 3d. This might be due to the experimental and theoretical difficulties brought about by the delayed onset in the 3d cross-section. Further work is needed to clarify this point.

The next systems we studied were the c(2x2) sulfur and selenium overlayers on Ni(011). The experimental results are shown in Fig. 16. Although a large effect is observed in both cases, no theoretical treatment is available at present. It is interesting to note that neither curve shows much resemblance to the LEED 00 beam intensity.

The final chalcogen-nickel system we have been able to study is Se/Ni(111). As it turns out,some of the most interesting results arose from this system and the lines of investigation it suggested in our most recent running time at SSRL. Most of the data have yet to be completely interpreted, but I choose to include Se/Ni(111) here since it provides some interesting tests and applications of what has been said so far.

Figure 17 shows experimental NPD results for low coverage, disordered and quarter monolayer (2x2) overlayers of selenium on Ni(111). Both surfaces had previously been heated to 500K either during or after the exposure, but were cooled during data acquisition. The (2x2) overlayer was observed over a coverage range of $\theta \sim .15-.25$ corresponding to exposures of 2-6L, and was quite sharp. As for the Se/Ni(001) system, the same general structure is observed in the two curves. The extra structure in the low coverage curve at 130 eV photon energy might be real, but more likely is a result of the experimental difficulties involved in working with lower coverages.

The next result of interest is the $(\sqrt{3}x\sqrt{3})R30^\circ$ coverage of Se/Ni(111). Unfortunately, we have yet to produce a really sharp LEED pattern with this structure. The $\theta \sim .5$ coverage surface yielded a

weak ($\sqrt{3}x\sqrt{3}$)R30° pattern with a substantial diffuse background. Such a surface was prepared by exposing the crystal at 500K to ~15L of H_2Se. The NPD result obtained after cooling to 120K is shown in Fig. 18 along with the (2x2) result. While the (2x2) surface showed large oscillations, the higher coverage produced a rather small NPD effect. It is interesting to note that the main peaks in the (2x2) curve also appear in the ($\sqrt{3}x\sqrt{3}$)R30° curve. There are, however, new peaks in the latter whose origin is as yet a subject of question. One possibility is that the two curves really are very different. Assuming the same site is preferred on the two surfaces, this idea is contrary to the results on the Se/Ni(001) system and the earlier results on the Se/Ni(111) system which implied that the NPD result is rather insensitive to the degree and type of two-dimensional order in the overlayer. On the other hand, the (111) and (100) surfaces might be expected to be different in this regard: on the (100) surface, the c(2x2) LEED beams form a subset of the p(2x2) beams, while the same is not true of the ($\sqrt{3}x\sqrt{3}$)R30° and (2x2) beams on Ni(111). Another possible explanation for these results is that on the $\theta = .5$ surface, multiple binding sites are populated. In this case more than one $d_\perp$ would contribute to the NPD signal with the consequent degrading of the oscillation amplitude. The peaks at 115, 144, and 192 eV photon energy would then correspond to the preferred low coverage site geometry, while the other peaks would correspond to one or more other values of $d_\perp$. Other photoemission results indicate that this multiple site idea at higher coverages might well be the case in this system.[27] Such a situation is not uncommon in surface science.

Credence is lent to this hypothesis by a temperature dependence study of the (2x2) Se/Ni(111) system. It has been reported[28] that high quality LEED patterns for the Se/Ni(111) system can be obtained by performing exposures to H_2Se with the sample cooled to 200K. We decided to try such a procedure. The results for a surface prepared at 120K and then studied before warming are shown in Fig. 19 along with the previous (2x2) results. In actual fact, the two curves were taken with the same surface, the only difference being that for the lower curve the sample had been heated to 500K and then cooled again to 120K. Both samples gave (2x2) LEED patterns, though that of the annealed surface was of higher quality. Little or no selenium was desorbed upon heating. The result was reproducible on three separate surface preparations: we are very confident that the effect shown in Fig. 19 is real. As with the higher coverage result, the "frozen" surface gave peaks at the same positions as those observed on the annealed surface, but there is additional structure on the frozen surface at 105, 135, and 175 eV photon energy, which is absent in the annealed surface NPD curve. Indeed, the annealed surface yielded cross-section minima at these energies. Warming the sample to room temperature seems to give a curve intermediate between the annealed and frozen results, though this result needs to be checked. The initial hypothesis in this case is that the Se can be frozen into multiple binding sites by performing exposures at low temperatures, and that by heating the surface the preferred site is populated exclusively. The interplay between kinetic and thermodynamic factors

is not unusual in other fields of chemistry, and to observe such an effect here is not overly surprising. What is significant is that NPD seems very well suited to the study of such multiple site effects because of its substantial sensitivity to $d_\perp$: each site would in general be expected to have a unique $d_\perp$ and would hence contribute a unique frequency to the NPD curve. By comparison, surface EXAFS would not be particularly valuable here since the nearest neighbor distance is not expected to change substantially from one site to another and each site would contribute the same EXAFS frequency. LEED could in theory treat two-dimensionally ordered multiple site systems, but the analysis by NPD proceeds in a much more straightforward manner. NPD might well become the accurate technique of choice for studying multiple site systems.

Having observed this freezing effect on Ni(111) we decided that an analogous study on Ni(001) was in order. The results of a before-and-after study on the p(2x2) Se/Ni(001) system similar to that shown in Fig. 19 for (2x2) Se/Ni(111) are shown in Fig. 20. While the oscillation amplitude of the frozen surface is less than that of the annealed one, the same general structure is observed in both curves: there are no additional peaks observed for the frozen surface. Presumably, the four-fold hollow site is preferred in both cases. A systematic shift of the peaks to lower energy is observed, however, and the shift becomes progressively larger at higher energy. This is exactly what one would expect if $d_\perp$ were increased by approximately 0.1 Å on the frozen surface. If one assumes that the H_2Se does not disdociate on

the cold surface there are at least two reasons why such an increase might be expected to occur. The first is simply a steric effect: the added bulk of the hydrogens precludes the selenium atoms from fitting as far down into the four-fold hollow site. The other reason is an electronic effect. Nickel is an electropositive metal: it is energetically stabilized by receiving electrons, thus filling its d-shell. The presence of hydrogen bonded to the selenium atom will lessen the ability of the selenium to donate electrons, producing a weaker and perhaps longer nickel-selenium bond. Both this system and the Se/Ni(111) system would benefit from studies by hydrogen-sensitive probes.

C. The molecular overlayer systems: CO/Ni(001) and CO/Ni(111)

In the past, photoemission has often been viewed as a technique to be used to give a preliminary characterization of the surface structure of molecular adsorption complexes. The least that was expected was that the number of structural possibilities to be used in a more accurate determination using a LEED analysis would be limited by a preliminary photoemission effort.[29,30] In Chapter I, reference was made to studies which went beyond that by characterizing some other aspect of surface structure, e.g., bond axis orientation.[31] It might be clear by now that photoemission can go even a good deal further than that in dealing with molecular adsorbate systems. I will show in this section some results which indicate that NPD might simplify the problem over LEED. The reason for this is due to the localized nature of PhD relative to LEED: essentially, the structure

of each atomic species may be determined independently. We have chosen the CO/Ni system to initiate our efforts since it is a system which has become somewhat of a model in surface science, and also since it is one with which LEED has had some difficulty in the past. Unfortunately, for the reasons laid out in Chapter II, Section A, carbon monoxide is a difficult species for us to study since the only two useful core levels (oxygen and carbon 1s levels) are rather tightly bound and hence lie in a region where our photon flux is low and the monochromator resolution is poor. The interest in the experiment, however, as well as the advent of substantial amounts of running time at SPEAR dedicated to the production of synchrotron radiation, convinced us to proceed in spite of these experimental difficulties. I reiterate here that the newer synchrontron radiation sources should largely surmount these problems.

The c(2x2) CO/Ni(001) system has given LEED studies a fair amount of difficulty in the past. The earliest study suggested that CO bonded in the fourfold coordinated hollow site.[32] Later, a high resolution electron energy loss study showed convincing evidence that the CO molecules in fact preferred the singly coordinated site geometry.[33] A subsequent LEED study found best agreement for that adsorption site, but with a rather small (.95 Å) vertical separation between the carbon and oxygen layers.[34] The conclusion was drawn that the molecular axis was inclinded by ~34° from the surface normal to accomodate this small separation. Several photoemission studies[31,35,36] contradicted this conclusion, asserting that to

within their resolution, the equilibrium position of the CO bond axis was perpendicular to the surface. One theoretical study attempted to rectify the disagreement by showing that the bond axis might be expected to contract upon chemisorption.[37] Finally, two LEED studies were nearly simultaneously reported which obtained results consistent with each other and with the photoemission studies.[38,39] The present belief is that the atop site is preferred with the carbon-nickel bond length ($d_{CNi}^{\perp}$) being 1.8 Å and the CO bond length ($d_{CO}^{\perp}$) being 1.1 Å.[38,39]

Traditionally, one of the major problems in studying this and other molecular[40] chemisorption systems with LEED is that the primary electron beam tends to damage - either by desorption or dissociation - the molecular overlayer. A simple calculation shows the problem clearly. A LEED electron gun typically has a focus size of ~$1mm^2$, or the equivalent of ~10^{13} surface layer atoms. Typical primary LEED beam currents are 10^{-6} Amperes, or 10^{13} electrons/sec. In other words, on the average every surface atom is being bombarded by one electron every second. Radiation damage cross-sections for electrons in this energy range are rather high, and an obvious problem arises. Substantially lower currents are possible by using pulse counting techniques and an area detector, and the author strongly feels that the future successes of LEED surface structure determinations on molecular systems depend on the use of such techniques.

Photoemission, on the other hand, is usually thought to be a non-damaging technique, although unpublished results indicate that even

with this technique one must be careful in studying labile systems.[41] The reasons for the non-damaging nature of photoemission are straightforward. We work with 10^{10} photons/second maximum, focused into a spot of 3-4 mm^2. In addition, to this 3-1/2 order of magnitude decrease in primary flux density over typical LEED measurements, photons are several orders of magnitude more penetrating (hence, less damaging) than electrons in this energy range. While the latest LEED studies[38,39] went to great lengths to lower their primary currents, to accumulate I-V curves rapidly, and even to move their sample slowly so as to sample different parts of the surface (a very questionable procedure), we have found such procedures to be unnecessary in our studies. Time-dependent (12-24 hours) degradation has been apparent, but its relation to the incident beam is uncertain and probably nonexistent.

To date, we have studied both the carbon 1s and oxygen 1s core levels in the c(2x2) CO/Ni(001) and the $(\sqrt{3}x\sqrt{3})R30^\circ$ CO/Ni(111) systems. I wish to reiterate that both core levels are very difficult for us to study, and the quality of our data at present is substantially poorer than that on the selenium systems reported earlier. The oxygen 1s level presents particular difficulties, and it has not been until quite recently that we have obtained reproducible data over a rather limited energy range.

We have studied the carbon 1s level in the c(2x2) CO/Ni(001) most and therefore have the most confidence in our NPD data on that level. These data are shown in Fig. 21 along with recent calculations by Tong

and Li for $d^{\perp}_{CNi}$ in the vicinity of 1.8 Å and $d^{\perp}_{CO}$ fixed at the free molecule value of 1.13 Å. The overlayer was situated in the atop position. This is the registry and carbon-nickel distance range where the best fit exists. The fit for the structure determined from the most recent LEED studies ($d^{\perp}_{CNi}$ = 1.8 Å, $d_{CO}^{\perp}$ 1.13 Å), considering the difficulty of our experiment, is exceptional. The peak energy positions are matched quite well for all four peaks in our data, as shown in Fig. 22. The fit to peak intensities is not particularly good, but a significant part of the discrepancy can be accounted for as being due to loss of contrast due to the increase in scattered relative to monochromatic light.

It is particularly interesting to test the sensitivity of the carbon 1s calculated NPD curve to the CO bond length. Calculations by Tong and Li shown in Fig. 23 indicate that the carbon 1s level gives us no sensitivity to that bond length: the calculated carbon 1s NPD curve is the same for all $d^{\perp}_{CO}$. The reason for this is simple[43] and is indicated in Fig. 24. I assume that CO stands up perpendicular to the surface with the carbon end down. If one wants to measure the CO bond length by using the carbon 1s NPD curve, the structural sensitivity must arise from a forward scattering event off the oxygen atom.[42] The relative phase of the direct and forward scattered waves, however, is independent of the CO bond length:[43] the forward scattering event adds phase to that wave, but it adds essentially the same amount, independent of where the oxygen is situated.[43] Hence, the NPD interference is independent of distance for a forward scattering event. The situation for a reverse scattering event, on the other

hand, is manifestly different. This would be the case in this system, for example, if one measures the oxygen 1s photoelectrons which scatter off the carbon layer. In this case, the electron must traverse the CO bond length twice, accumulating the phase $2kd_{CO}^{\perp}$ along the way. The oxygen is NPD results should be sensitive to the CO bond length as well as to all deeper perpendicular distances.

The significance of this result is substantial. It implies that in doing structural determinations on molecularly adsorbed species, using NPD one can proceed from the inside out, determining the smallest $d_{\perp}$ atomic species first and then proceeding to those located further away from the surface. This will in the long run make such determinations much easier since the iteration to the best calculational fit should be a much shorter process. Again, we find the localized, atom-specific nature of PhD relative to LEED to be very important. It should be noted that this ability to determine $d_{\perp}$ for each atomic species individually is characteristic of NPD, but is probably less true of APD as the added phase argument breaks down away from normal emission.

For reasons which are now obvious, we wanted very badly to measure the oxygen 1s level. In our latest running period, we have accumulated such data, and they are shown for the c(2x2) CO/Ni(001) system in Fig. 25. There is as yet only an incomplete calculational effort for this level,[43] but a reasonable fit seems a distinct possibility.

We have also accumulated NPD curves for the carbon and oxygen 1s levels in the $(\sqrt{3}x\sqrt{3})R30^{\circ}$ CO/Ni(111) system. Our interest in this

system is that CO is thought to prefer the twofold coordinated site.[44] The chances for an accurate LEED study on this system, however, are remote since mediocre LEED patterns are prevalent.[45] We have obtained only very faint and diffuse superstructure spots which would make LEED measurements impossible. Presumably the average two-dimensional domain size in this system is small. NPD, however, has been shown to be rather insensitive to the degree of two-dimensional order so that systems such as this are obvious candidates for the technique.

Figure 26 shows our NPD data on the carbon 1s level along with calculations by Tong and Li[10] for the two-fold bridge-bonded site with $d^{\perp}_{CNi}$ = 1.27 Å. With the exception of the region near 90-100 eV kinetic energy, a reasonably good fit is observed. This is by far the best fit for any value of $d^{\perp}_{CNi}$. We conclude that the bridge site is indeed preferred at these low coverages.

As yet, only a preliminary calculational effort exists on the oxygen 1s level for this system. In spite of this fact an acceptable fit is found for the free molecule bond length of 1.13 Å and the previous $d^{\perp}_{CNi}$, 1.27 Å, as shown in Fig. 27. This observation is tempered by an apparent misfit near 55-60 eV kinetic energy. However, this is the energy range where the constant kinetic energy nickel Auger peak interferes with our normally smooth background. I have dashed the experimental curve in this region since vastly different results can be obtained with rather minor changes in our background subtraction. This problem is most severe for the oxygen 1s level since

the photoemission peak is broad and weak. Considering the experimental difficulties involved and the limited accessible energy range, I view the fit in Fig. 28 as quite good.

References: Chapter III:

1. S. Anderson, J. B. Pendry, B. Kasemo, and M. Van Hove, Phys. Rev. Lett., 31, 595 (1973); M. Van Hove and S. Y. Tong, J. Vac. Sci. and Technol., 12, 230 (1975).

2. This chapter is based in part on work published in the following papers: S. D. Kevan, D. H. Rosenblatt, D. Denley, B.-C. Lu, and D. A. Shirley, Phys. Rev. Lett., 41, 1565 (1978); Phys. Rev. B20, 4133 (1979).

3. S. T. Manson, Advances in Electronics and Electron Physics, 44, 1 (1977). F. Combet Farnoux, J. Phys. (Paris) 32, (C4), 227 (1972).

4. N. V. Smith, P. K. Larsen, and S. Chaing, Phys. Rev., B16, 2699 (1977).

5. S. Y. Tong and C. H. Li, Phys. Rev., B19, 1769 (1979).

6. M. O. Krause, Electron Spectroscopy of Atoms and Molecules, in Synchrotron Radiation Research, S. Doniach and H. Winnick, eds., Plenum Press (1979).

7. C. H. Li and S. Y. Tong, Phys. Rev. Lett., 43, 526 (1979).

8. E. A. Stern, Phys. Rev., B10, 3027 (1974); some success in treating the near edge structure in EXAFS has been reported using multiple scattering calculations, (J. Pendry, private communication to be published).

9. J. E. Demuth and T. N. Rhodin, Surface Science, 45, 249 (1979).

10. S. Y. Tong, private communication.

11. A. Liebsch, Phys. Rev. Lett., 32, 1203 (1974); Phys. Rev., B13, 544 (1976).

12. C. H. Li and S. Y. Tong, Phys. Rev. Lett., 42, 901 (1979).

13. H. A. Betne and E. E. Salpeter, Quantum Mechanics of One and Two Electron Atoms, New York, Academic Press, 1957.

14. I. T. McGovern, W. Ebernardt, and E. W. Plummer, Solid State Commun., 32, 963 (1979).

15. D. Norman, D. P. Woodruff, N. V. Smith, M. M. Traum, and H. H. Farrel, Phys. Rev., B18, 6789 (1978); D. P. Woodruff, D. Norman, B. W. Holland, N. V. Smith, H. H. Farrel, and M. M. Traum, Phys. Rev. Lett., 41, 1130 (1978); N. V. Smith, H. H. Farrell, M. M. Traum, D. P. Woodruff, D. Norman, M. S. Woolfson, and B. W. Holland, Phys. Rev., B21, 3119 (1980).

16. N. V. Smith, private communication, to be published.

17. D. W. Jepsen, P. M. Marcus, and F. Jona, Phys. Rev., B5, 3933 (1972).

18. C. B. Duke and G. F. Laramore, Phys. Rev., B2, 4765 (1970); Phys. Rev., B2, 4783 (1970).

19. J. Pendrey, Low Energy Electron Diffraction, Chap. 6, Academic Press, 1974.

20. B. E. Warren, X-ray Diffraction, Addison-Wesley, 1969.

21. V. V. Schmidt, Bull, Acad. Sci. USSR, Ser. Phys. 25, 988 (1961); 27, 392 (1963).

22. J. D. Hanawalt, Z. Phys., 70, 293 (1930), and Franklin Inst., 214, 569 (1932); F. W. Lytle, Developments in Applied Spectroscopy, (Plenum, New York, 1963), Vol. 2, p. 285.

23. N. J. Shevchik, Phys. Rev., B16, 3428 (1977).

24. R. S. Williams, P. S. Wenner, J. Stohr, and D. A. Shirley, Phys. Rev. Lett., 39,. 302 (1977).

25. Z. Hussain, S. Kono, R. E. Connelly, and C. S. Fadley, Phys. Rev. Lett., 44, 895 (1980). Z. Hussain, C. S. Fadley, and S. Kono, submitted to Phys. Rev. B.

26. S. D. Kevan and D. A. Shirley, Phys. Rev., BXX, XXX(XXXX).

27. T. N. Rhodin, private communication.

28. T. W. Capehart and T. N. Rhodin, J. Vac. Sci., and Technol., 16, 594 (1979).

29. J. J. McCarrol, Surface Science, 53, 297 (1975).

30. C. R. Brundle, Surface Science, 48, 99 (1975).

31. See refs. 12-14 of Chapter I.

32. J. C. Tracy, J. Chem. Phys., 56, 2736 (1972).

33. S. Andersson, Solid State Commun., 21, 75 (1977).

34. S. Andersson and J. B. Pendry, Surface Science, 71, 75 (1978).

35. R. F. Davis, S. D. Kevan, D. H. Rosenblatt, J. G. Tobin, and D. A. Shirley, to be published.

36. L.-G. Petersson, S. Kono, N.F.T. Hall, C. S. Fadley, and J. B. Pendry, Phys. Rev. Lett., 42, 1545 (1979).

37. J. K. Norskov, H. Helmberg, and B. I. Lundqvist, Solid State Commun., 28, 899 (1978).

38. M. Passler, A. Ignatiev, F. Jona, D. W. Jepsen, and P. M. Marcus, Phys. Rev. Lett., 43, 360 (1979).

39. S. Andersson and J. B. Pendry, Phys. Rev. Lett., 43, 363 (1979).

40. L. L Kesmedel, P. C. Stair, R. C. Baetzold, and G. A. Somorjai, Phys. Rev. Lett., 36, 1316 (1976).

41. The cyanogen (C_2N_2)/Ni(111) system is such a system; the carbon-carbon bond seems to cleave slowly on irradiation with a helium resonance lamp.

42. The contribution of paths involving two interlayer backscattering events would produce sensitivity to the CO bond length in this case, but such paths have been shown to make a negligibly small contribution to the NPD result. (See Ref. 43).

43. C. H. Li and S. Y. Tong, Phys. Rev. Lett., 43, 526 (1979).

44. J. C. Campuzano and R. G. Greenler, J. Vac. Sci. and Technol., 16, 445 (1979).

45. H. Conrad, G. Ertl, J. Kuppers, and E. E. Latta, Surface Science, 57, 475 (1976); W. Erley, K. Besocke, and H. Wagner, J. Chem. Phys., 66, 5269 (1977).

Table I. NPD Peak Energies (in eV) for c(2x2)Se(3d)/Ni(001)

Data set[a]	Peak 1	Peak 2	Peak 3	Peak 4
8a	37[b]	53	86	130
8b	37	52	86	131
8c	37	52	89	136
8d	37	54	87	130

[a] Refers to curves a - d in Fig. 8.

[b] All entries are electron kinetic energies referred to the nickel vacuum level.

Figure Captions: Chapter III

Figure 1. Energy distribution curve of the c(2x2) Se/Ni(001) system at 150 eV photon energy showing the three elastic photoemission peaks arising from the nickel valence band and 3p levels and the selenium 3d level. Note the extreme surface sensitivity evidenced by the large selenium peak for just a half-monolayer coverage.

Figure 2. Three-dimensional plot of the NPD effect. Note the non-atomiclike oscillations in the various peak intensities.

Figure 3. Relative cross-sections of the three peaks in Fig. 1 as a function of kinetic energy.

Figure 4. Top three curves: calculated selenium 3d intensity as a function of electron kinetic energy for three different values of d_1 as defined in the text. Bottom curve: experimental result.

Figure 5. Comparison of the calculated selenium 3d intensity as a function of kinetic energy for constant d_1 but for different registries relative to the nickel surface. Note that rather small changes are predicted when one changes registry compared to those observed in changing d_1.

Figure 6. Definition of d_1 and its relation to coordination number for the Se/Ni(001) system.

Figure 7. Comparison of the NPD experimental result to the LEED 00 and 01 beams for the p(2x2) Se/Ni(001) system.

Figure 8. Results of NPD studies of the c(2x2) Se/Ni(001) system for various polarizations of the incident radiation. Only small changes are observed.

Figure 9. Intensity vs. photon energy curves for the c(2x2) Se/Ni(001) system for various polar-azimuthal exit angle combinations.

Figure 10. Comparison between two intensity-energy curves taken at nearly the same polar angle of emission but different azimuthal angles. Note the remarkable similarity of the main features in the two curves.

Figure 11. NPD results for two low coverage, disordered selenium overlayers on Ni(001) compared to the c(2x2) results.

Figure 12. NPD results taken at three temperatures for the p(2x2) Se/Ni(001) system. Dashed lines indicate an approximate atomic background as explained in the text.

Figure 13. Plots of $(I-I_0)/I_0$ for the three tempratures in Fig. 12. Curves are smoothed versions of the real data.

Figure 14. Plots of $\ln((I-I_0)/I_0)$ vs. absolute temperature for 149 and 192 eV photon energy.

Figure 15. NPD calculations for the three symmetric adsorption sites of sulfur/Ni(001) compared to experimental data. Best fit is for the accepted value of $d_\perp = 1.3$ Å.

Figure 16. Experimental NPD results for the c(2x2) sulfur and selenium overlayers on Ni(011).

Figure 17. Experimental NPD resuls for low coverage disordered and quarter monolayer (2x2) coverage of Se/Ni(111). Note the similarity in the main features of the curves.

Figure 18. Comparison of NPD curves for the high coverage ($\sqrt{3}$x $\sqrt{3}$)R30° Se/Ni(111) and (2x2) Se/Ni(111).

Figure 19. Comparison of NPD curves for frozen and annealed (2x2) Se/Ni(111).

Figure 20. Comparison of NPD curves for frozen and annealed p(2x2) Se/Ni(001). Note the systematic shift of peak energies from one curve to another.

Figure 21. NPD results for the c(2x2) CO/Ni(001) system. Top three curves: calculation for various carbon-nickel separations and fixed CO bond length with the atop site occupied. Bottom curve: experimental result.

Figure 22. Comparison between the optimum calculated result and the experimental result for the carbon 1s NPD curve for the c(2x2) CO/Ni(001) system.

Figure 23. Calculatons showing the effect of varying the CO bond length on the carbon 1s NPD result for the c(2x2) CO/Ni(001) system.

Figure 24. NPD scattering mechanisms and structural sensitivity. The relative phase of the direct and scattered waves is independent of atomic separation for forward scattering events, but not for reverse scattering.

Figure 25. NPD data for the oxygen 1s level in the c(2x2) CO/Ni(001) system. Only a preliminary calculational effort exists for this system. Dashed region of curve is where the substrate Auger peak interferes with our data.

Figure 26. Experimental and theoretical NPD results for the carbon 1s level in the $(\sqrt{3}x\sqrt{3})R30^\circ$ CO/Ni(111) system. Best fit is found for the bridge bonded site.

Figure 27. Experimental and theoretical NPD results for the oxygen 1s level in the $(\sqrt{3}x\sqrt{3})R30^\circ$ CO/Ni(111) system. Dashed region of the experimental curve is where the substrate Auger peak interferes with our data.

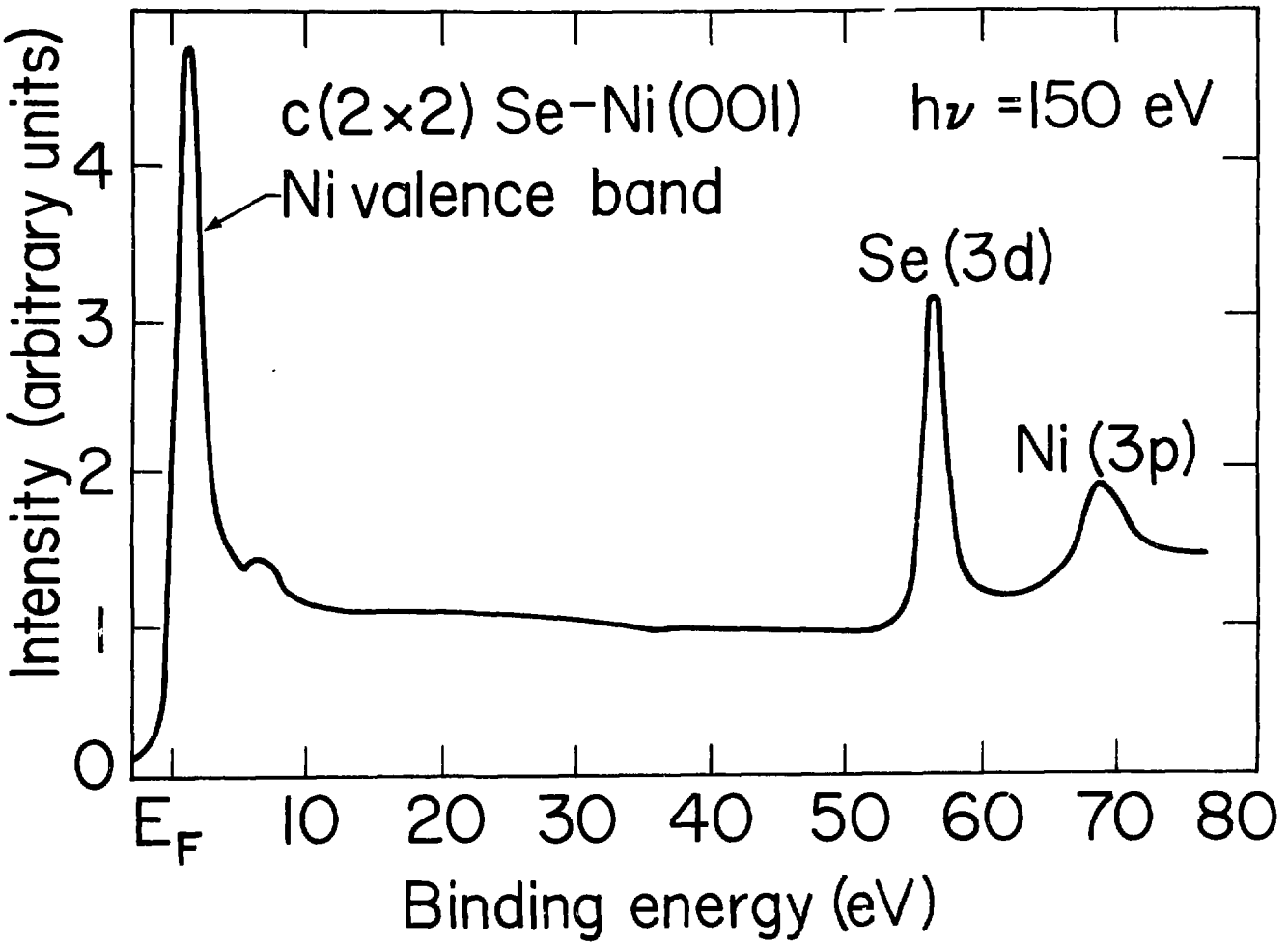

Figure 1

XBL 794-1372

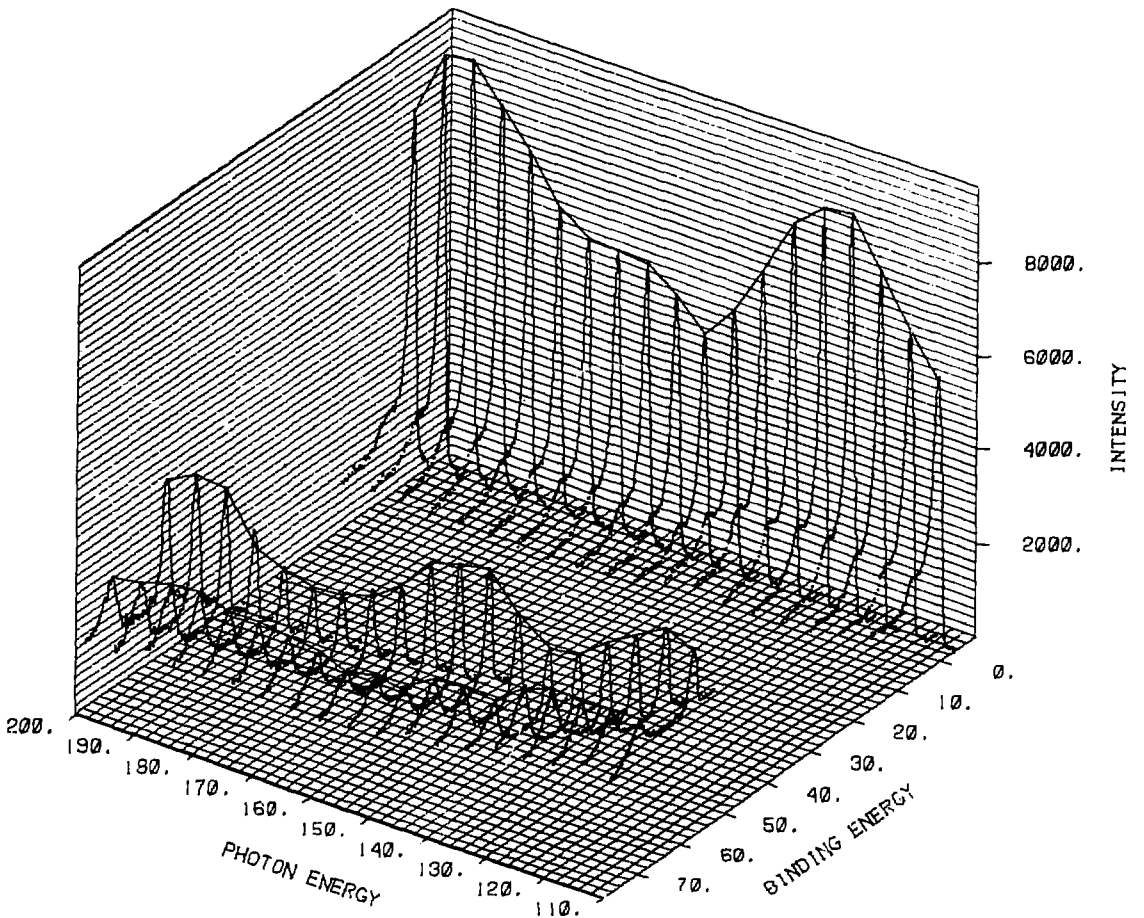

Figure 2

XBL 798-10842

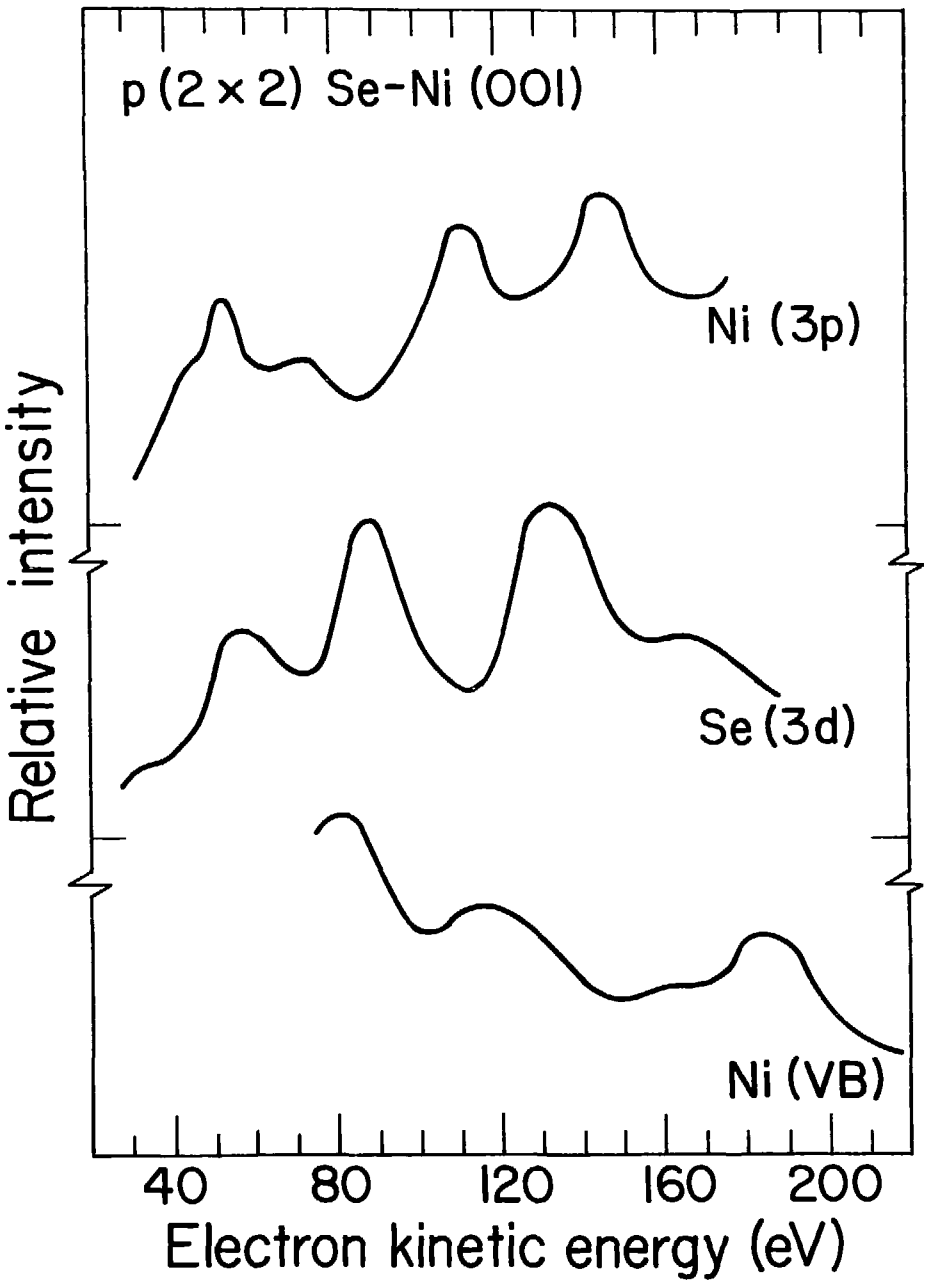

XBL 794-1374

Figure 3

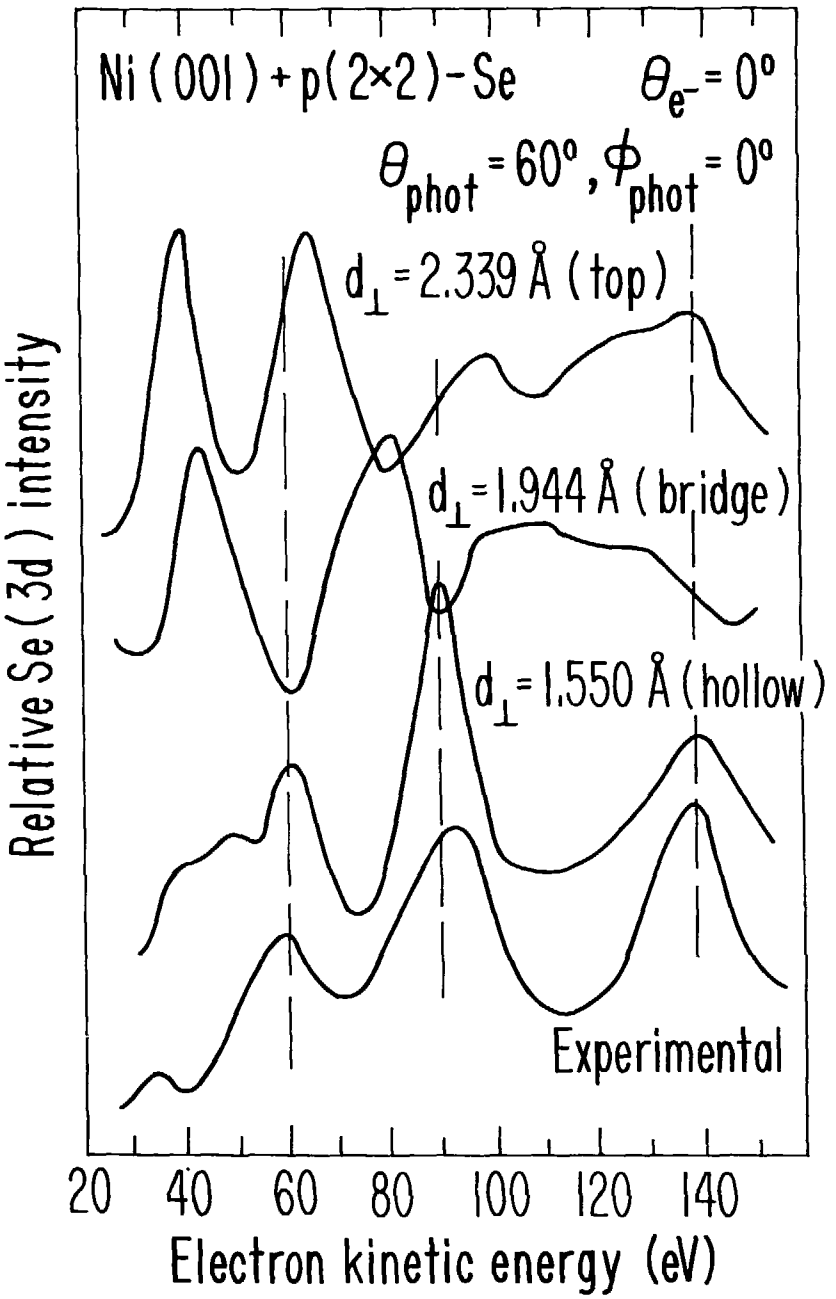

XBL7911-13241

Figure 4

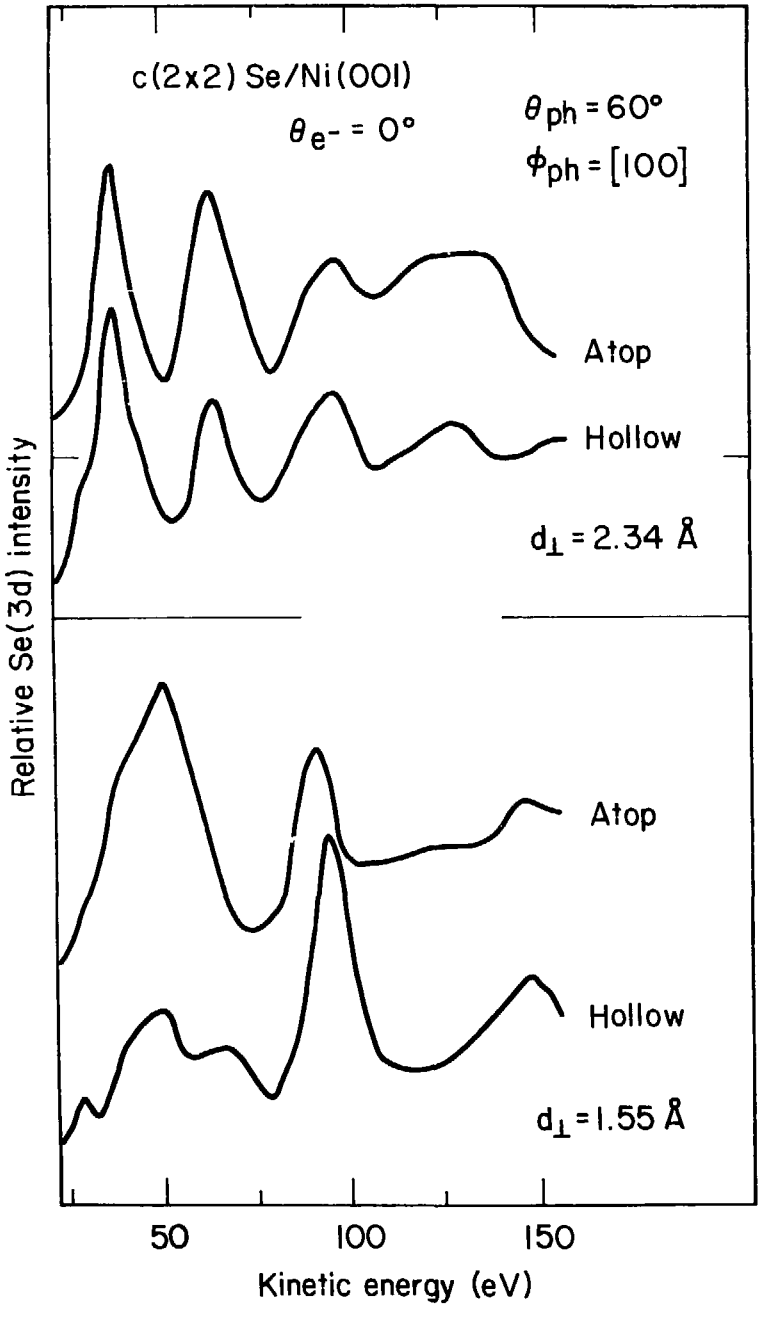

XBL-806-1358

Figure 5

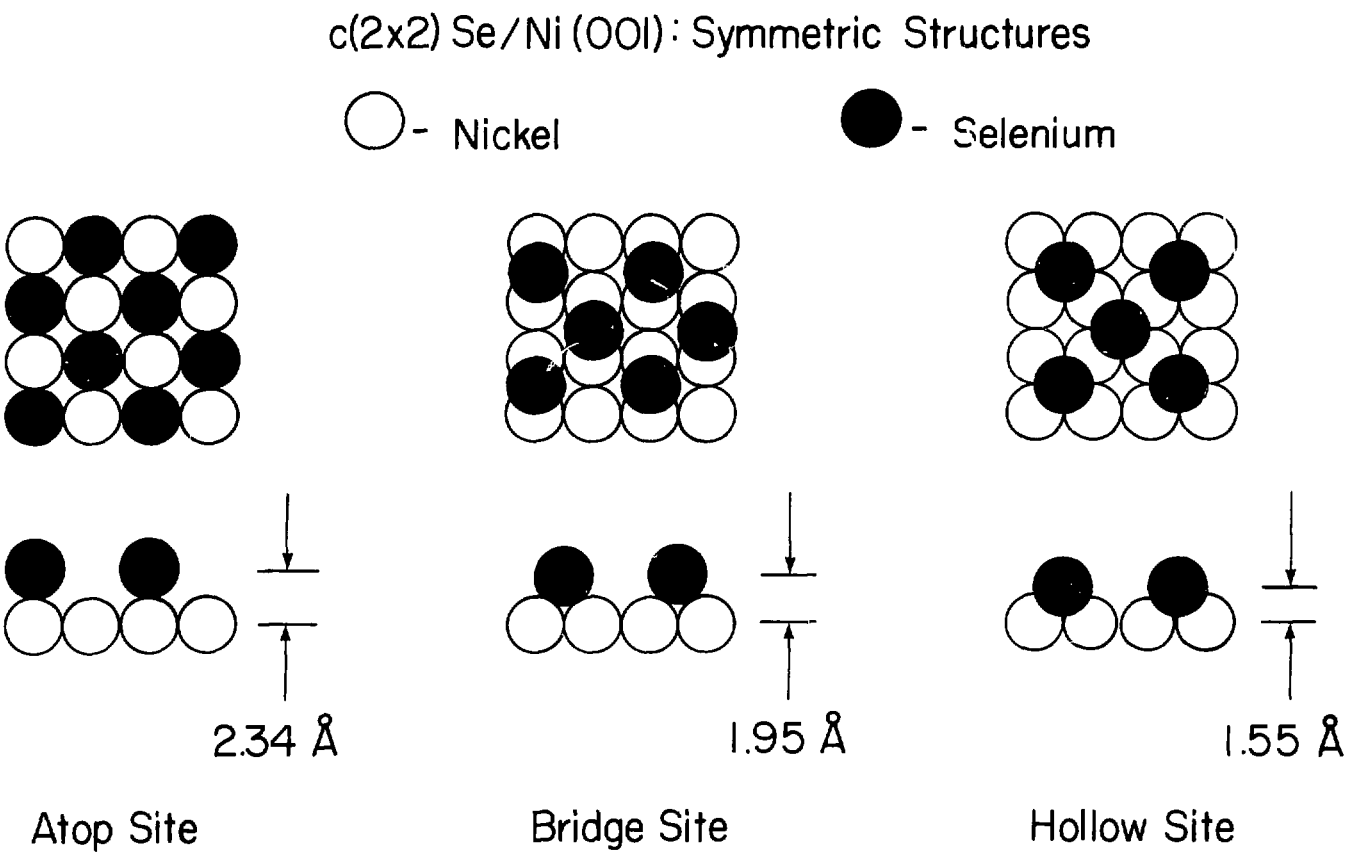

Figure 6

XBL-806-1361

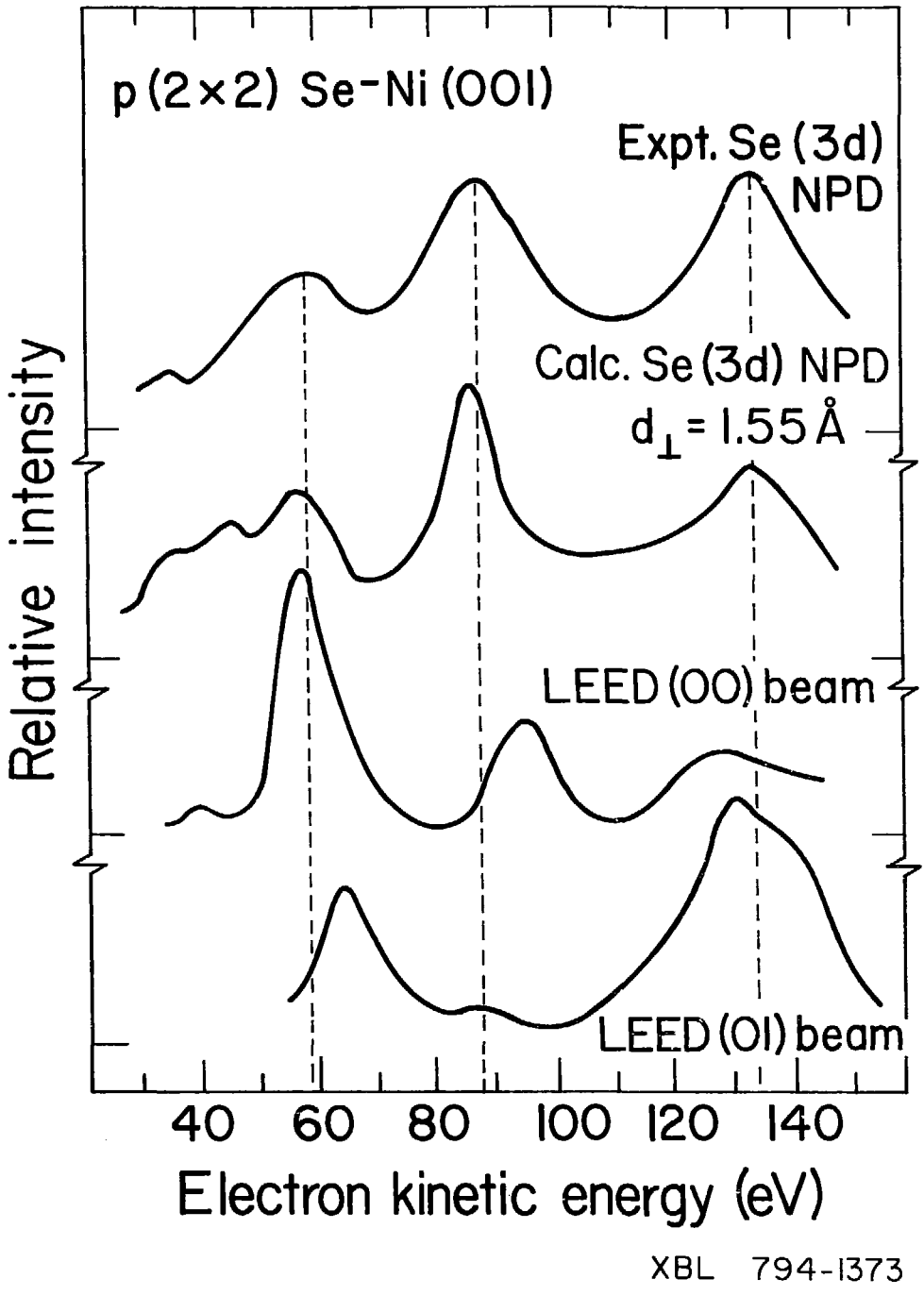
p(2×2) Se-Ni(001)
Expt. Se(3d) NPD
Calc. Se(3d) NPD
$d_\perp$ = 1.55 Å
LEED (00) beam
LEED (01) beam
Relative intensity
40
60
80
100
120
140
Electron kinetic energy (eV)
XBL 794-1373

Figure 7

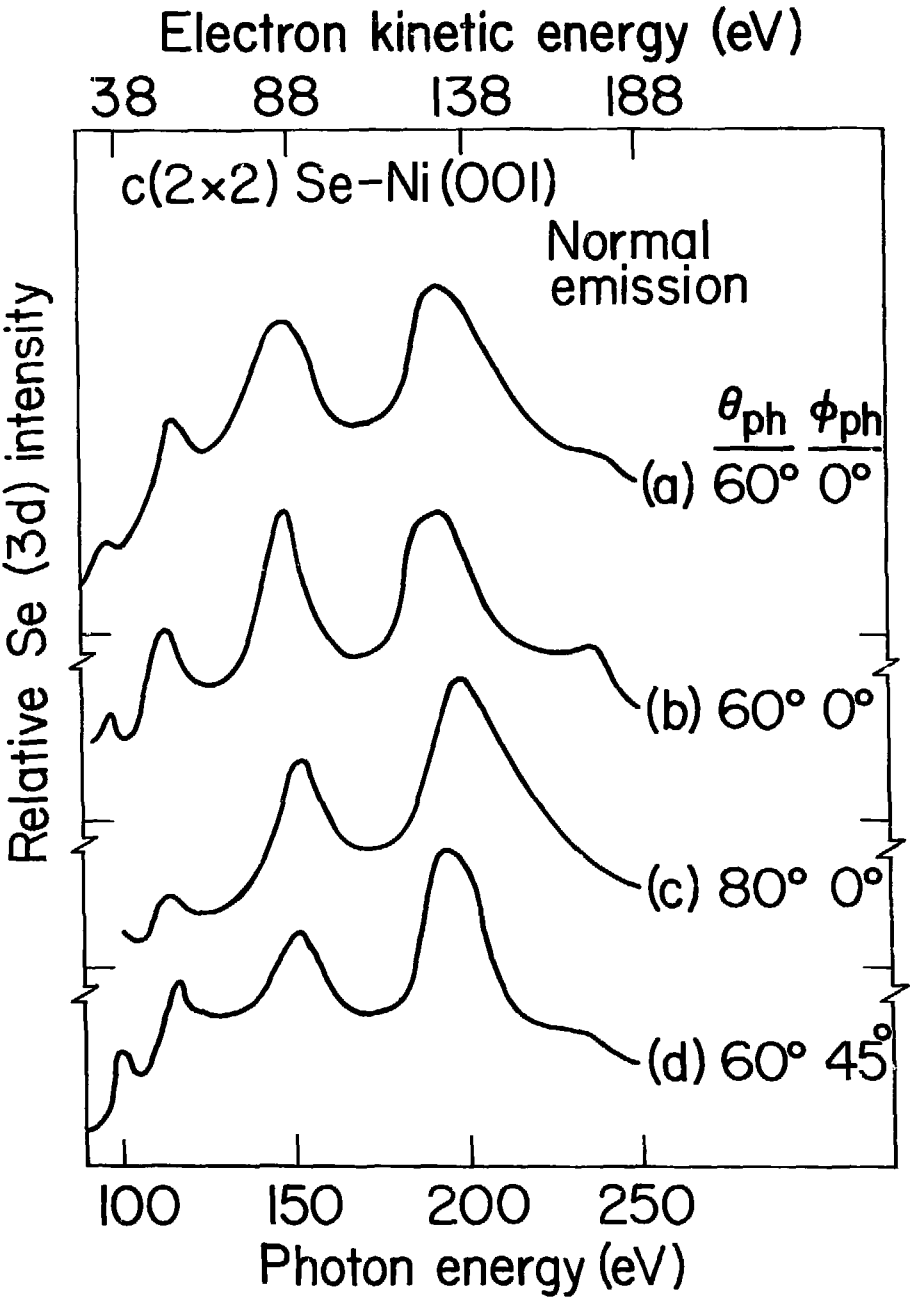

XBL 794-1371

Figure 8

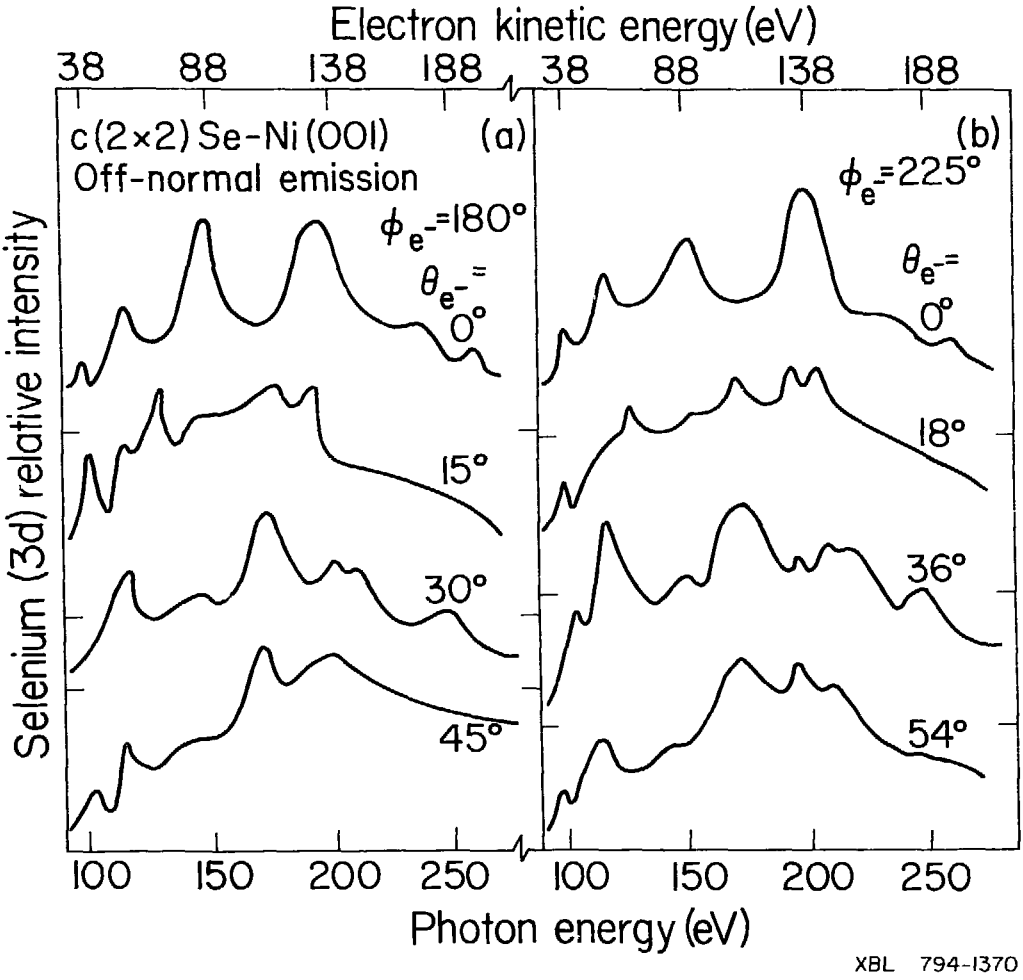
Electron kinetic energy (eV)
38
88
138
188
38
88
138
188
c(2×2) Se-Ni(001)
Off-normal emission
(a)
(b)
ϕ_e=180°
θ_e=
0°
15°
30°
45°
ϕ_e=225°
θ_e=
0°
18°
36°
54°
Selenium (3d) relative intensity
100
150
200
250
100
150
200
250
Photon energy (eV)
XBL 794-1370

Figure 9

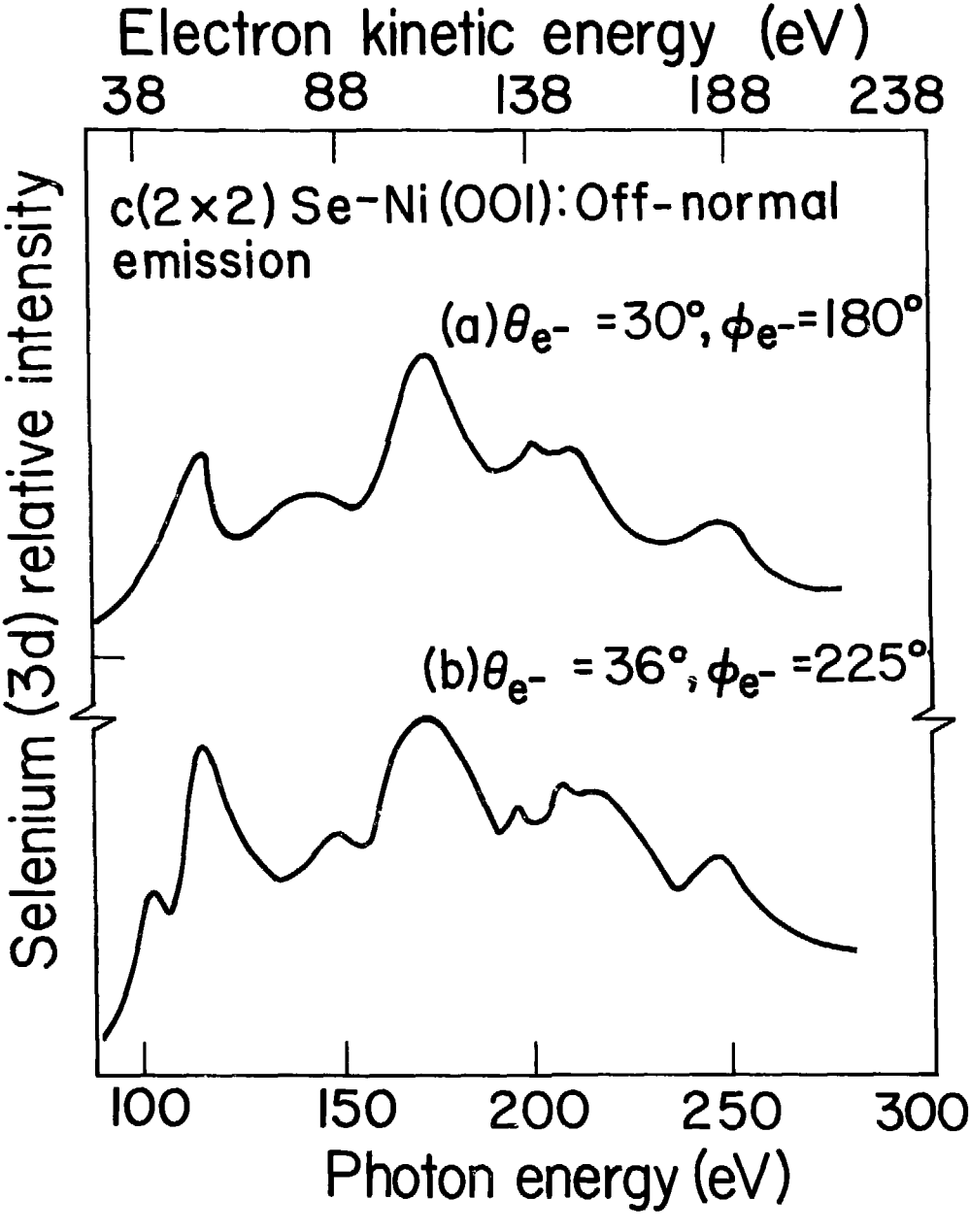

XBL 794-1369

Figure 10

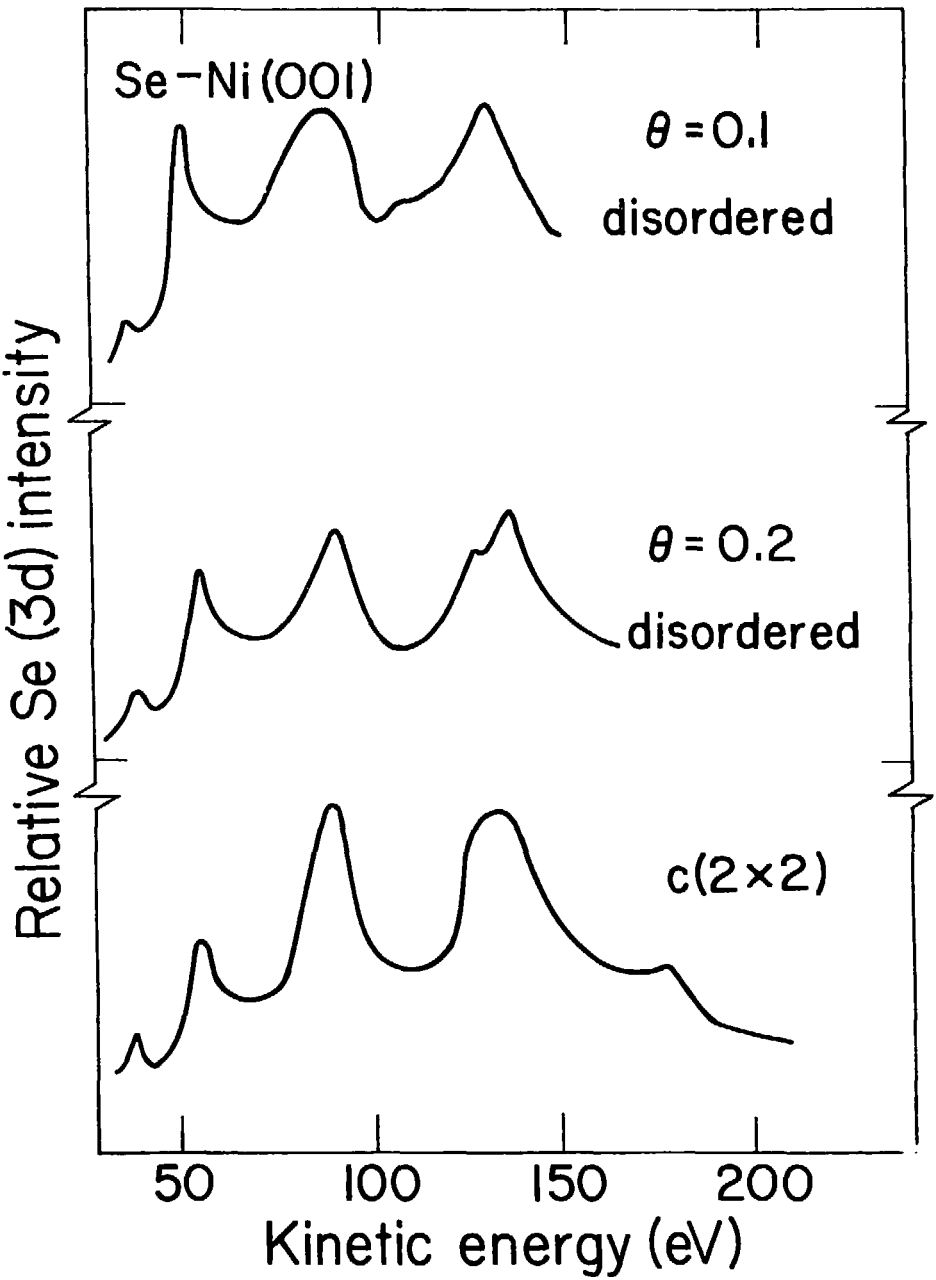

XBL 794-1376

Figure 11

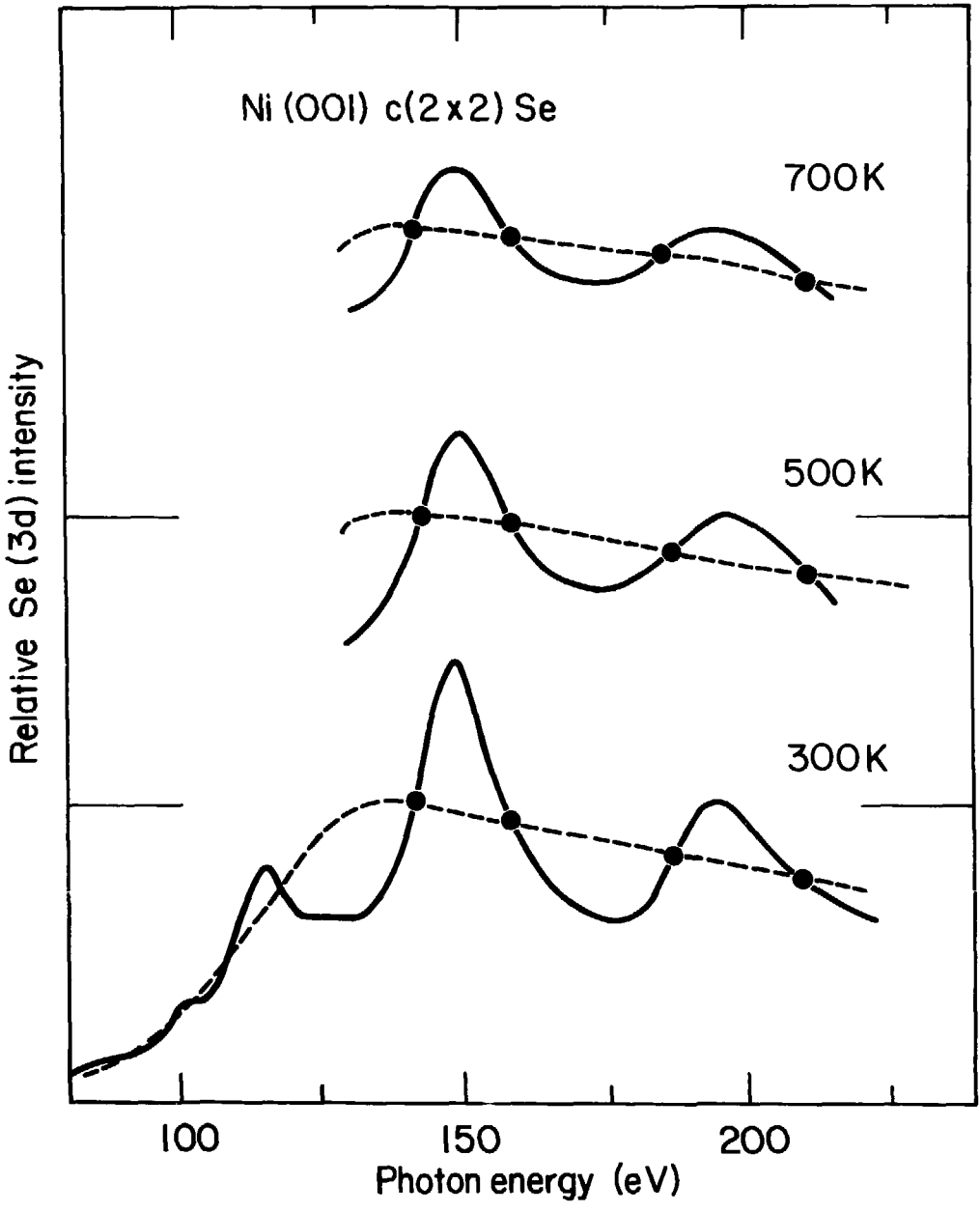

XBL-806-1360

Figure 12

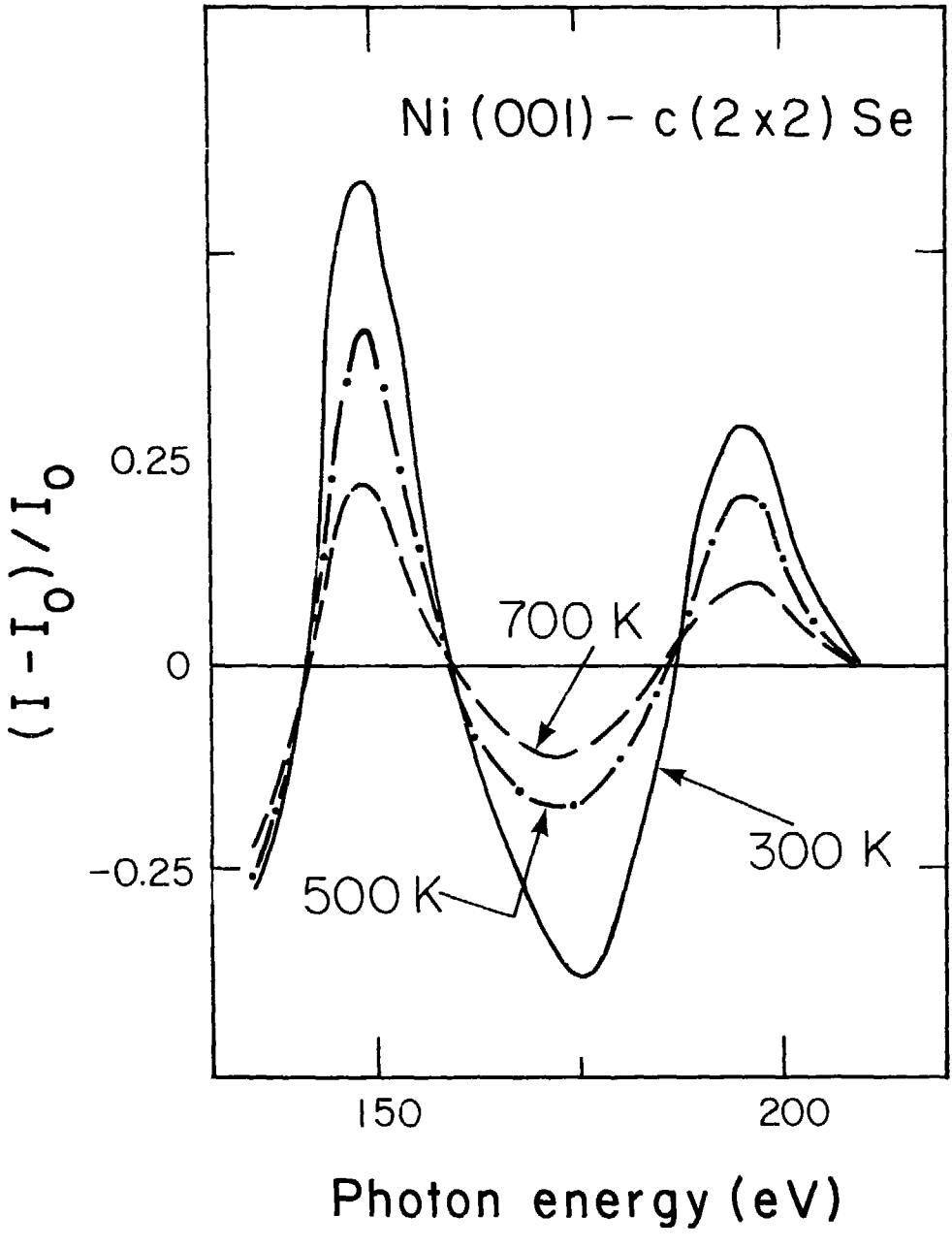

XBL 805-1072

Figure 13

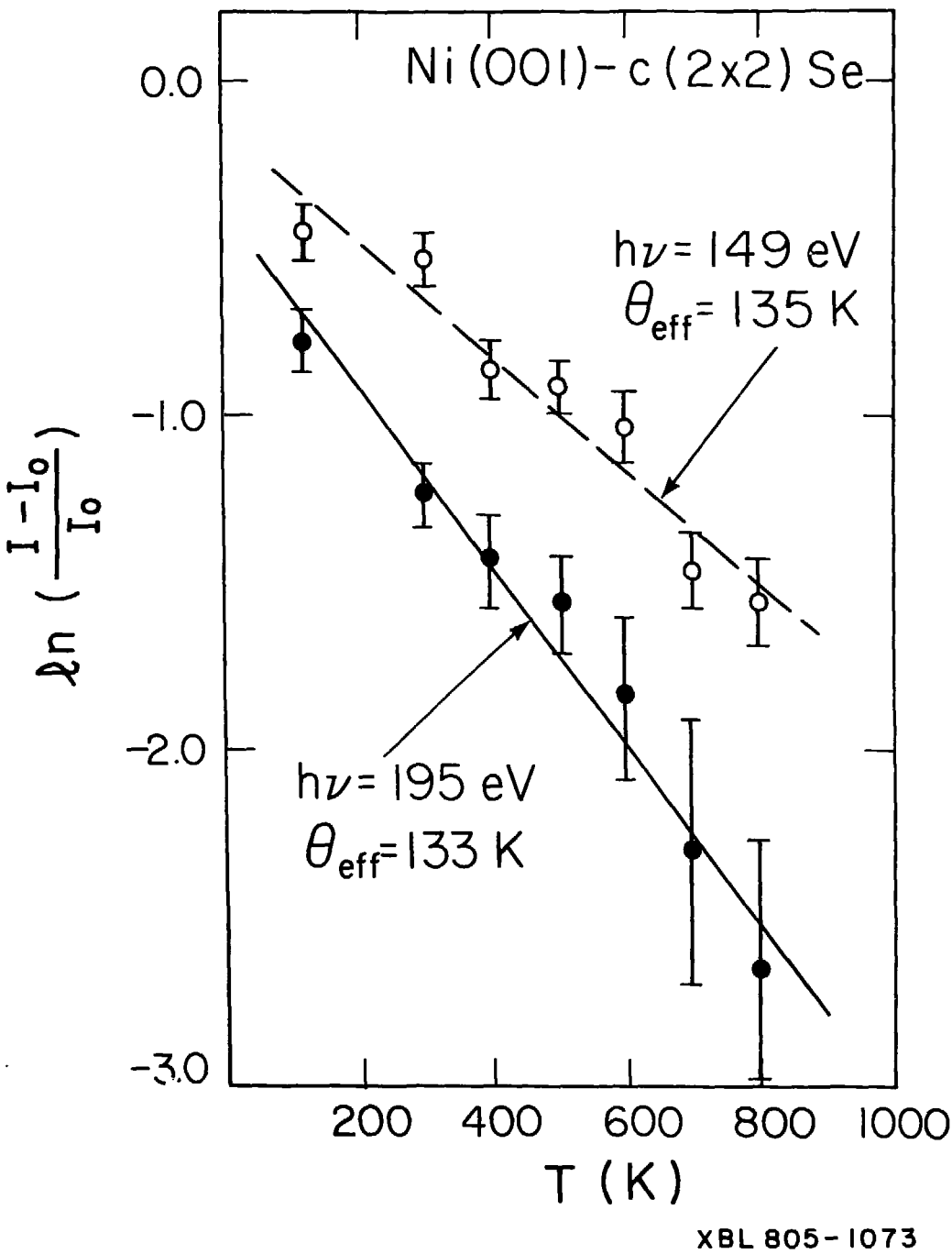
Ni(001)-c(2x2)Se
hν = 149 eV
θeff = 135 K
hν = 195 eV
θeff = 133 K
ln ((I - I0)/I0)
0.0
-1.0
-2.0
-3.0
200
400
600
800
1000
T (K)
XBL 805-1073

Figure 14

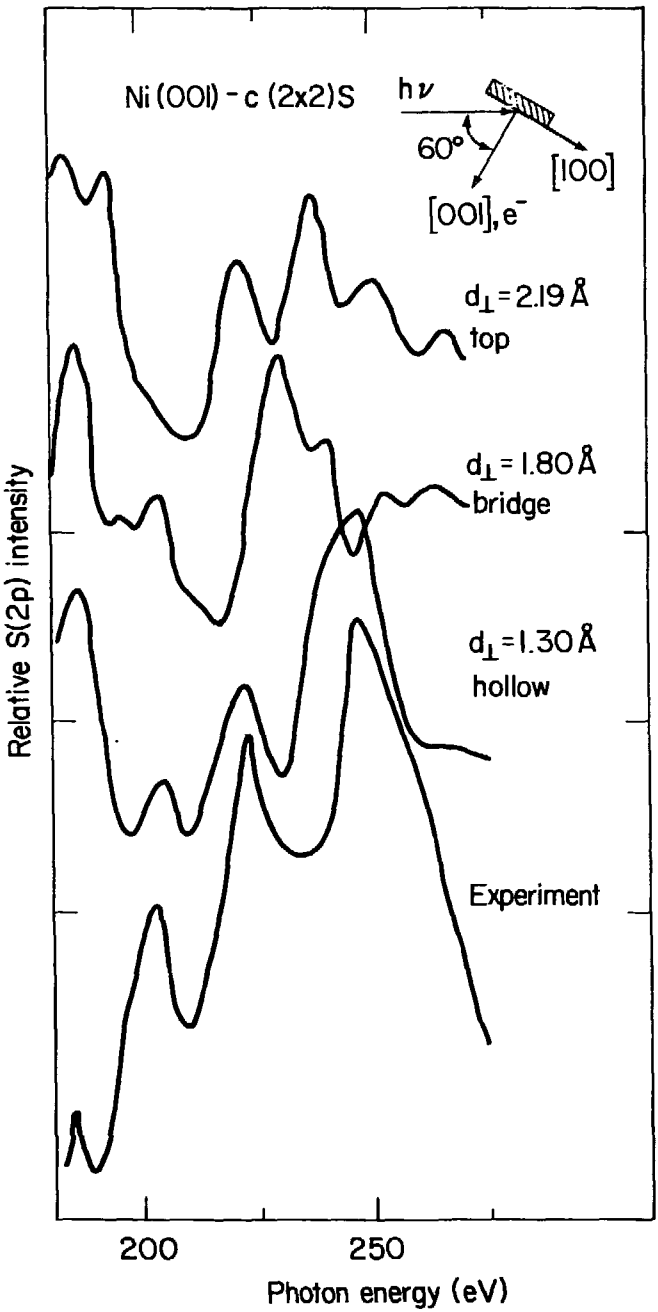

XBL-806-1362

Figure 15

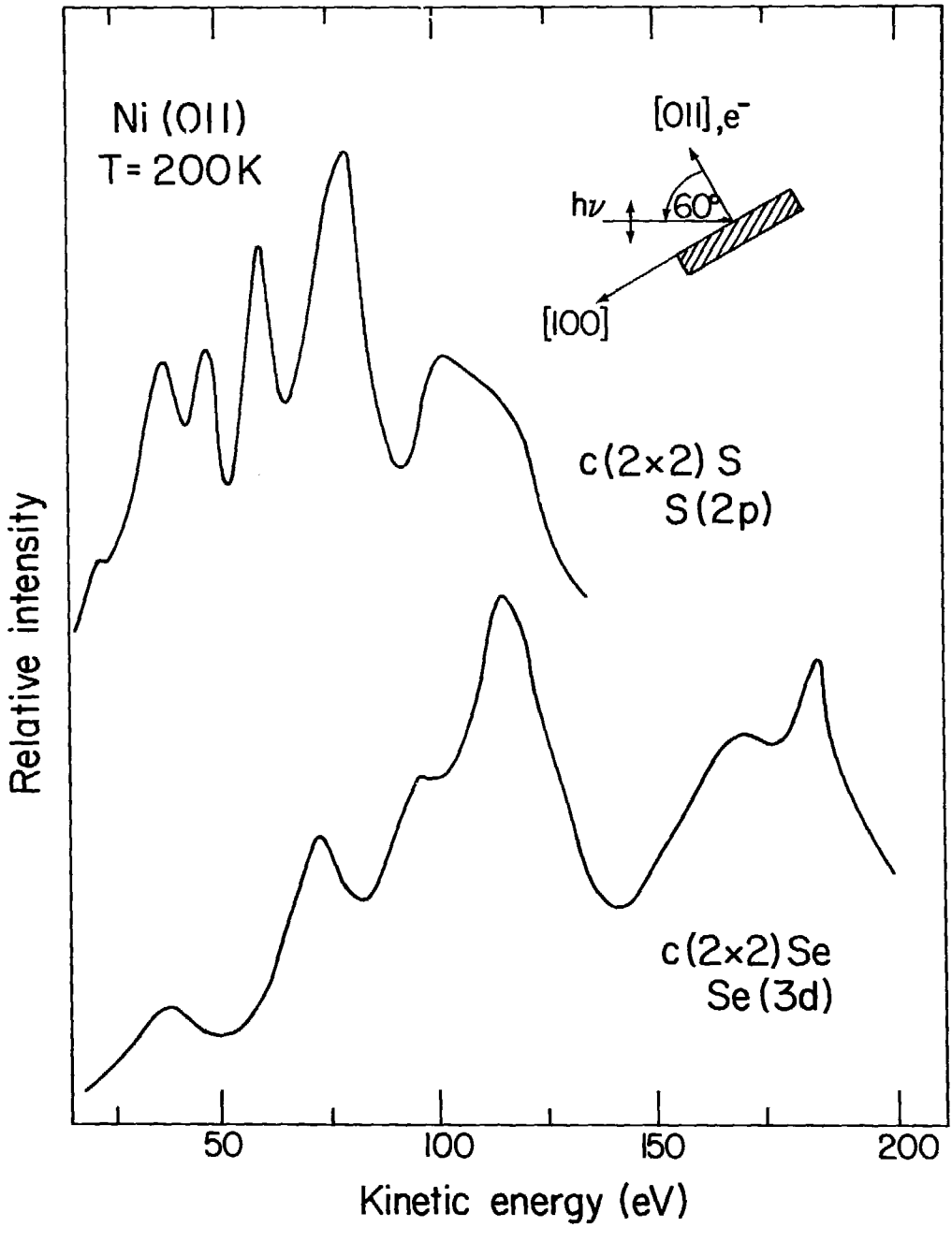

XBL796-1882

Figure 16

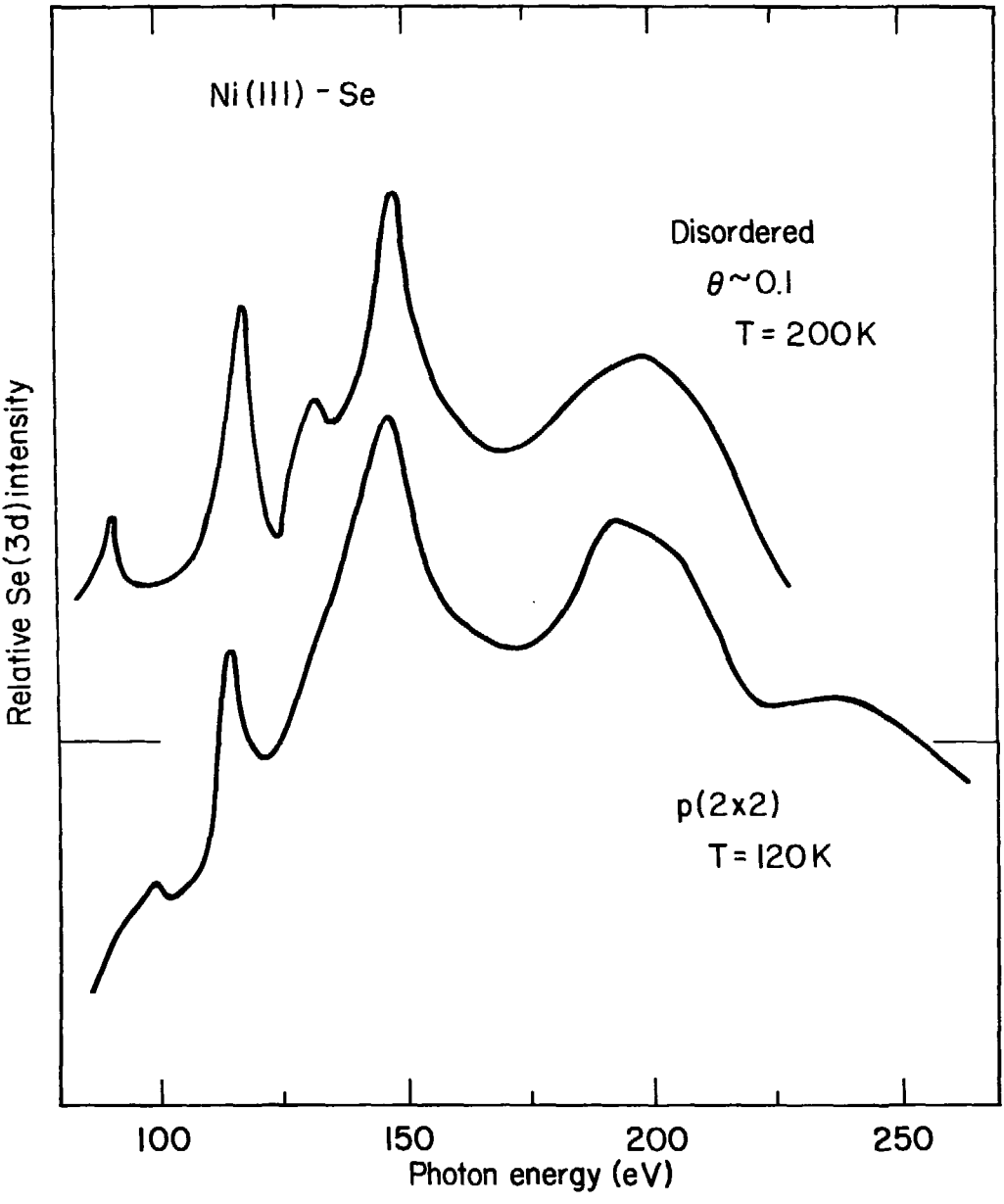

XBL-806-1359

Figure 17

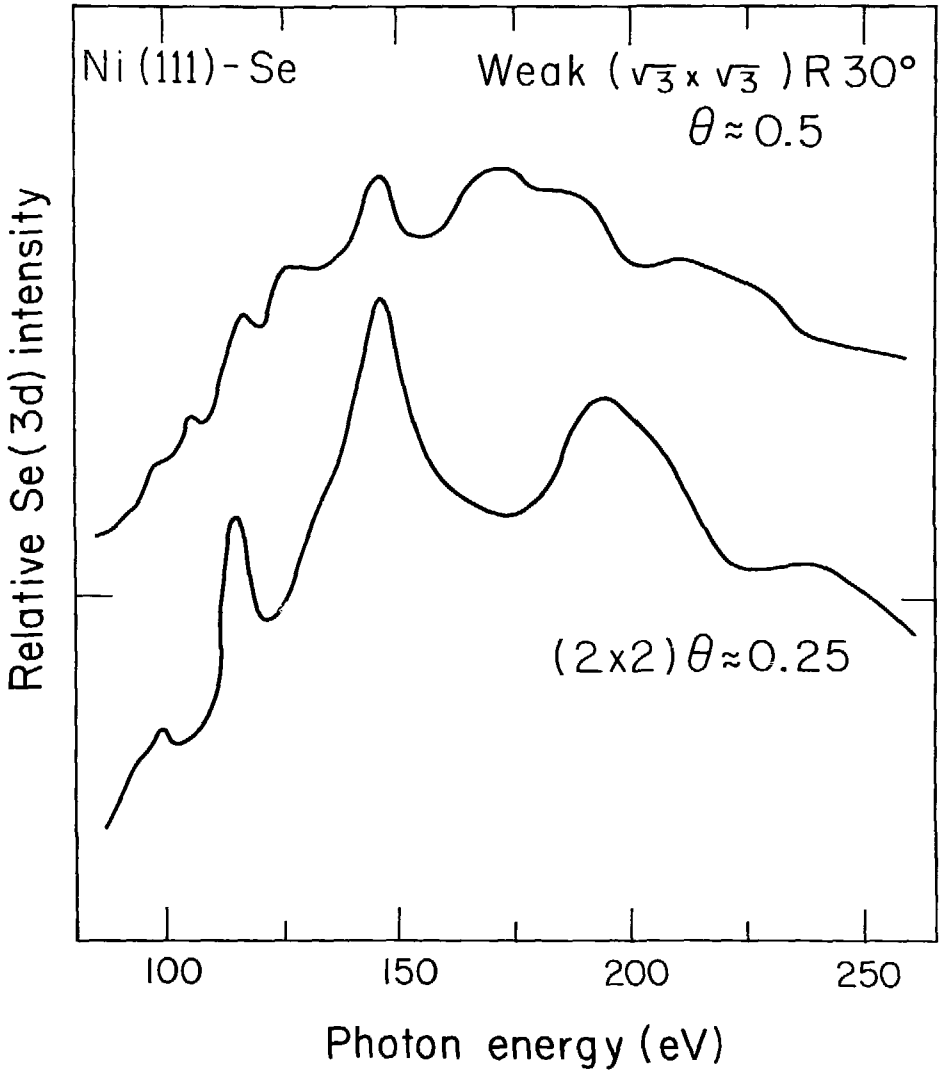

XBL805-1070

Figure 18

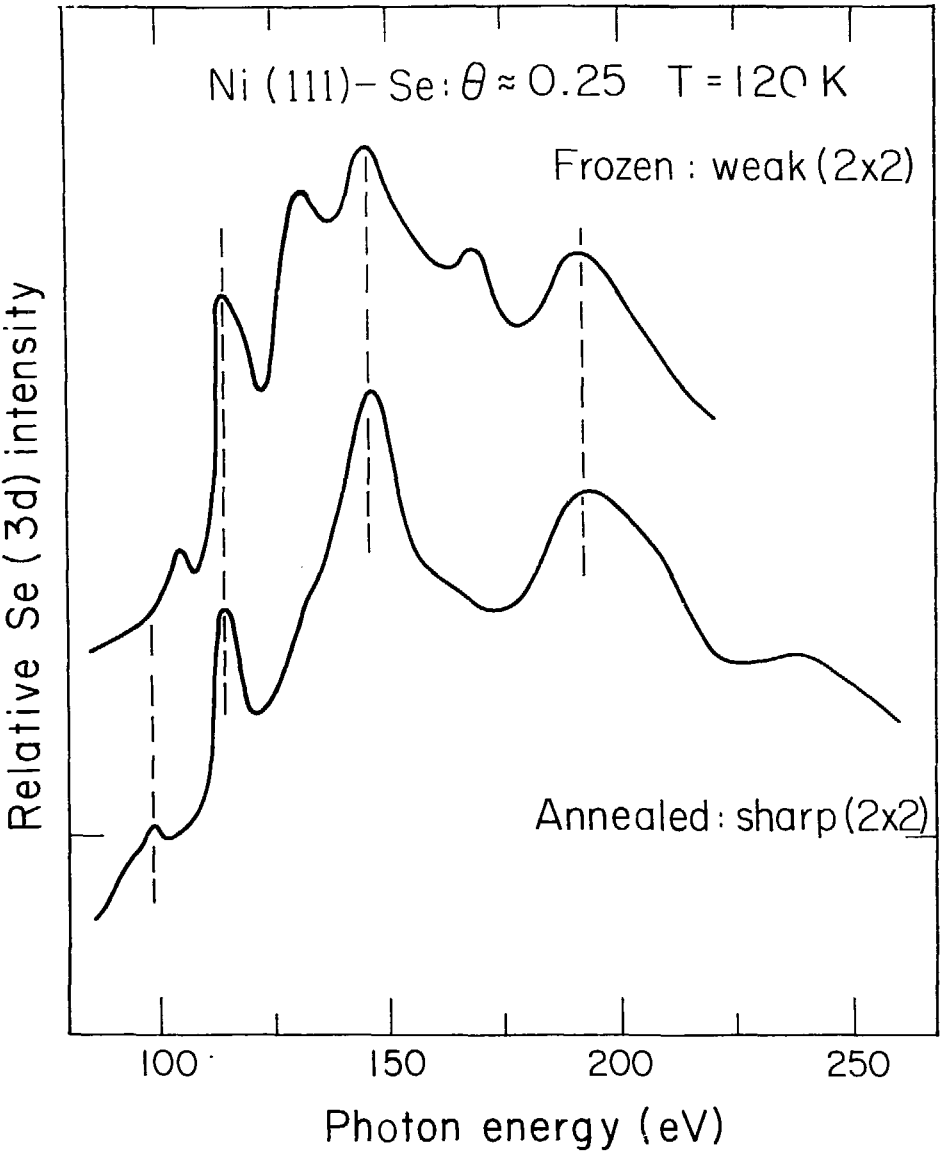

XBL 805-1069

Figure 19

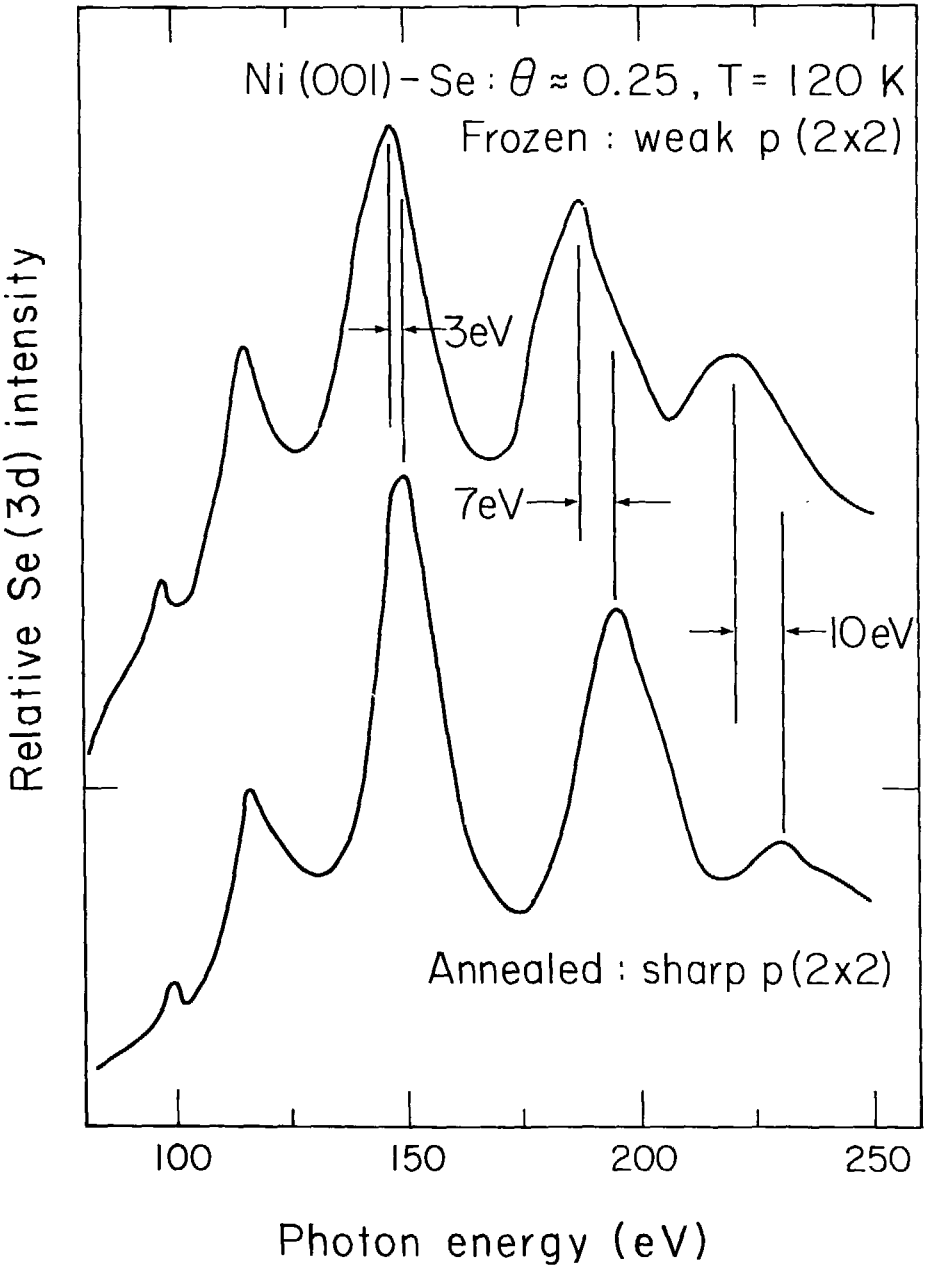

XBL805-1071

Figure 20

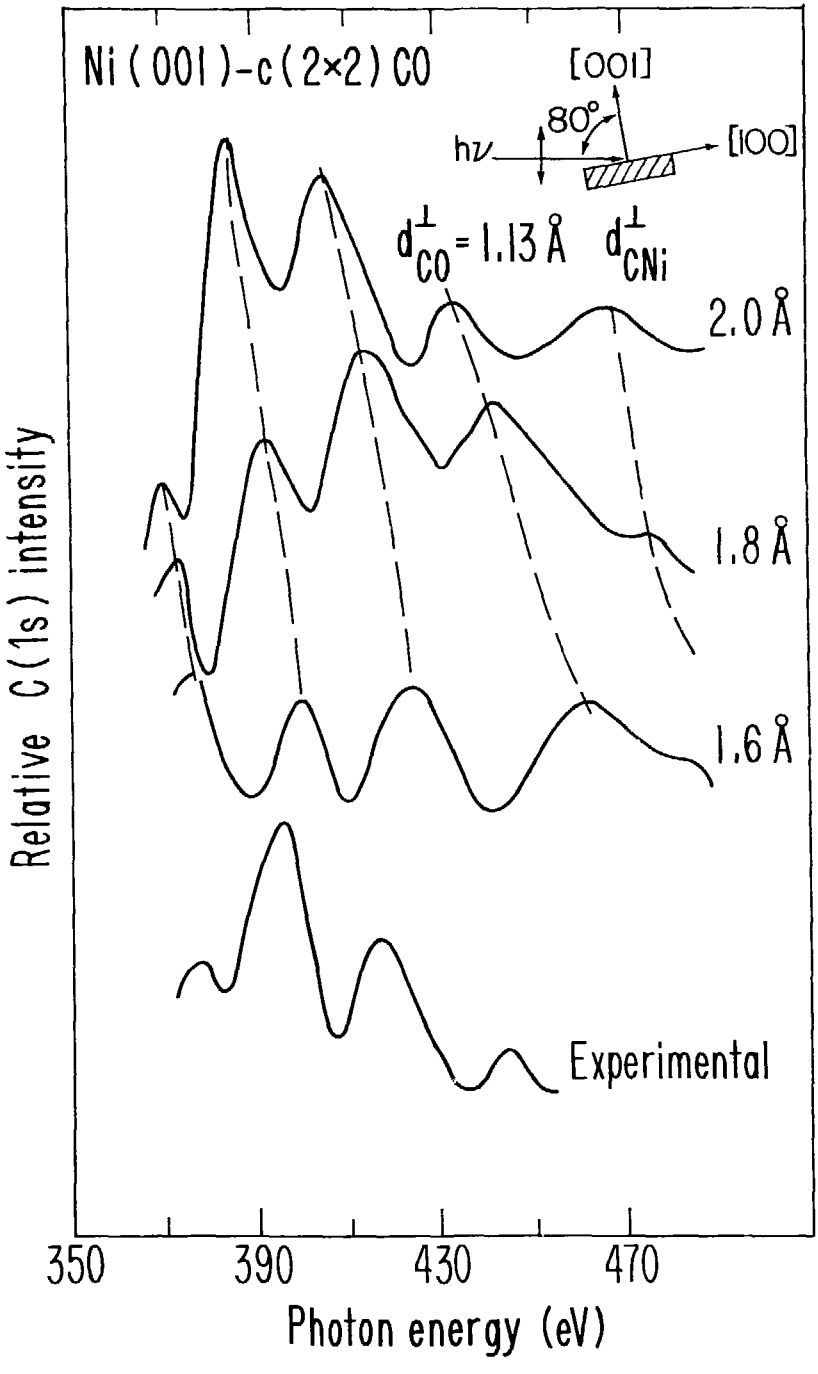

XBL 7911-13242

Figure 21

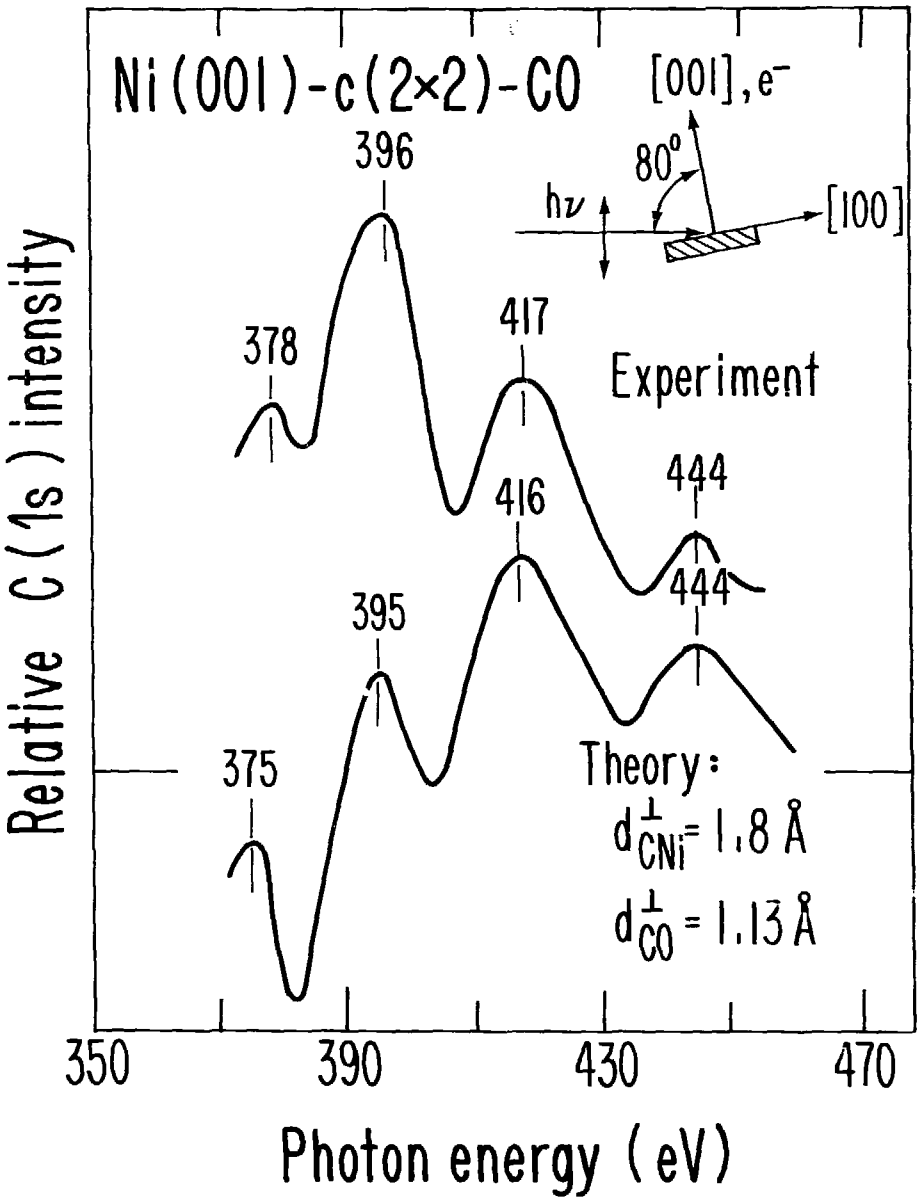

XBL7911-13243A

Figure 22

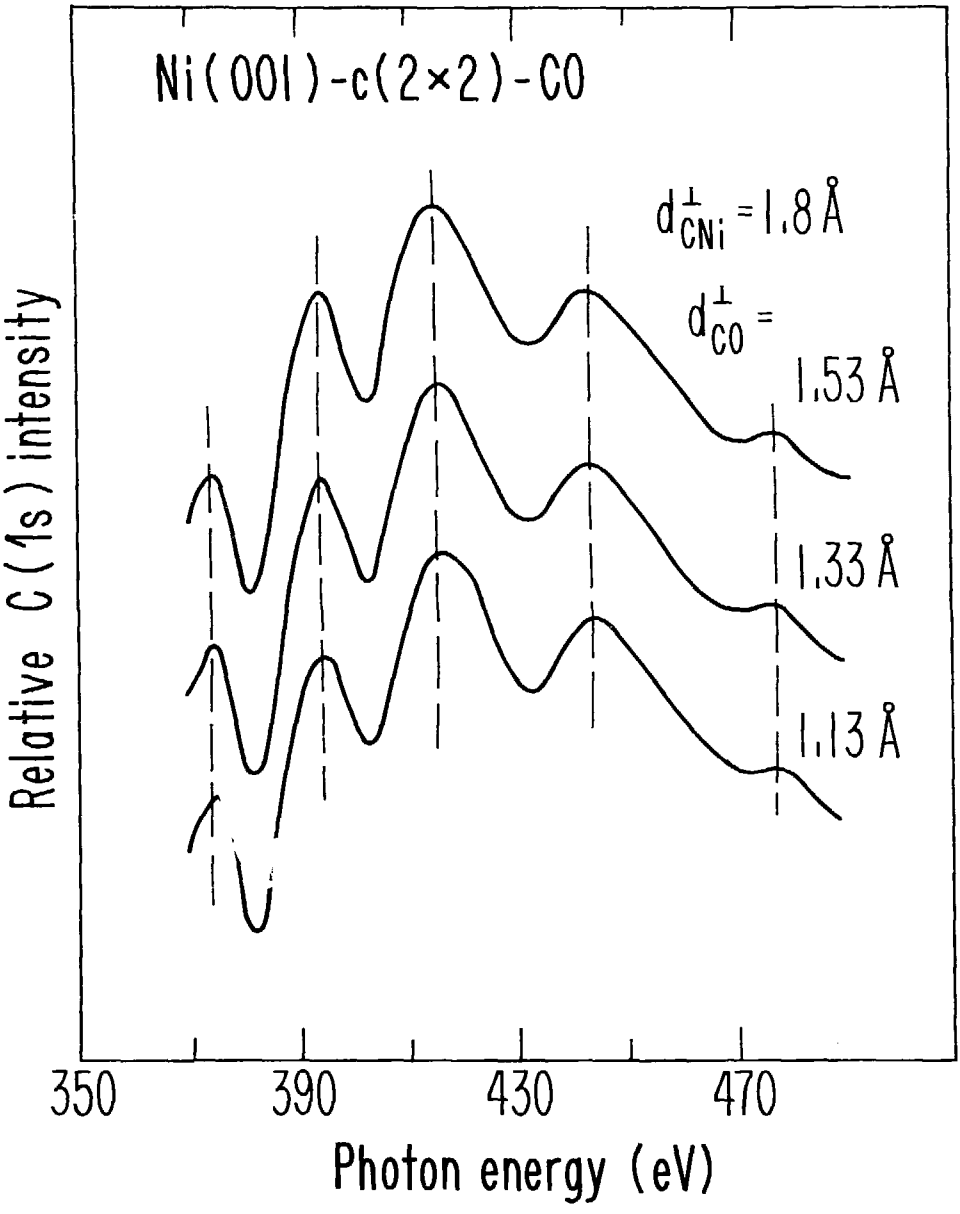

XBL7911-13243

Figure 23

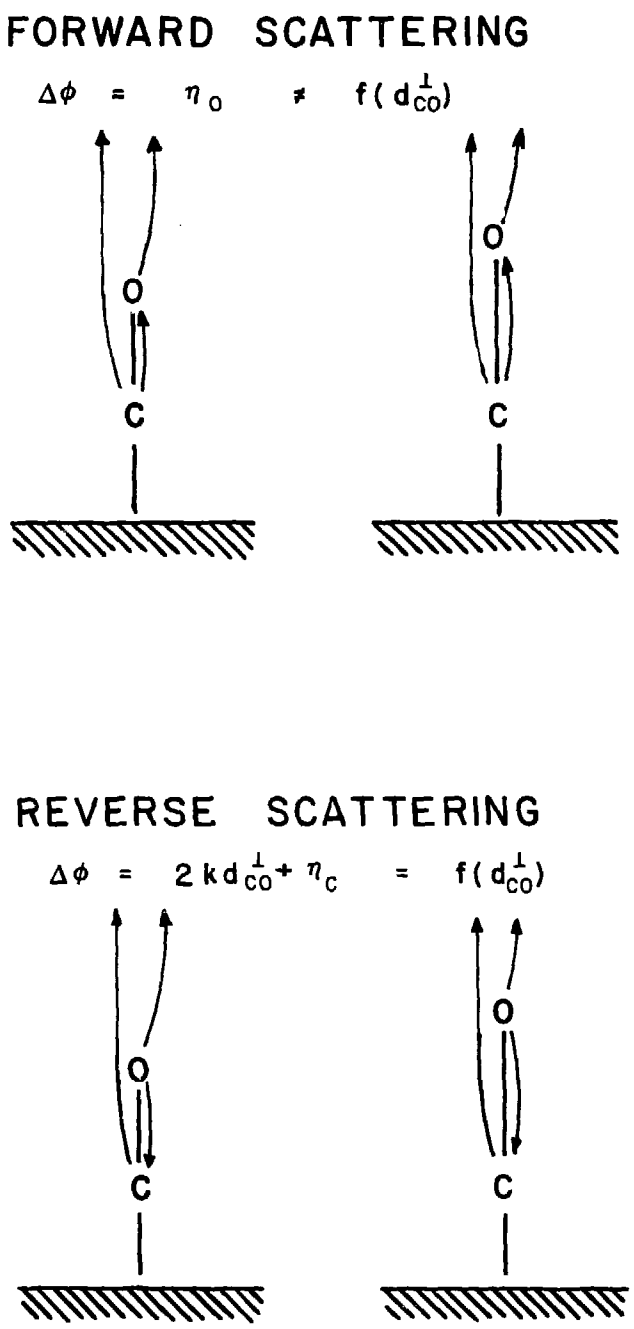
FORWARD SCATTERING
$\Delta\phi = \eta_O \neq f(d_{CO}^{\perp})$
O
C
O
C
REVERSE SCATTERING
$\Delta\phi = 2kd_{CO}^{\perp} + \eta_C = f(d_{CO}^{\perp})$
O
C
O
C
XBL 806-9961

Figure 24

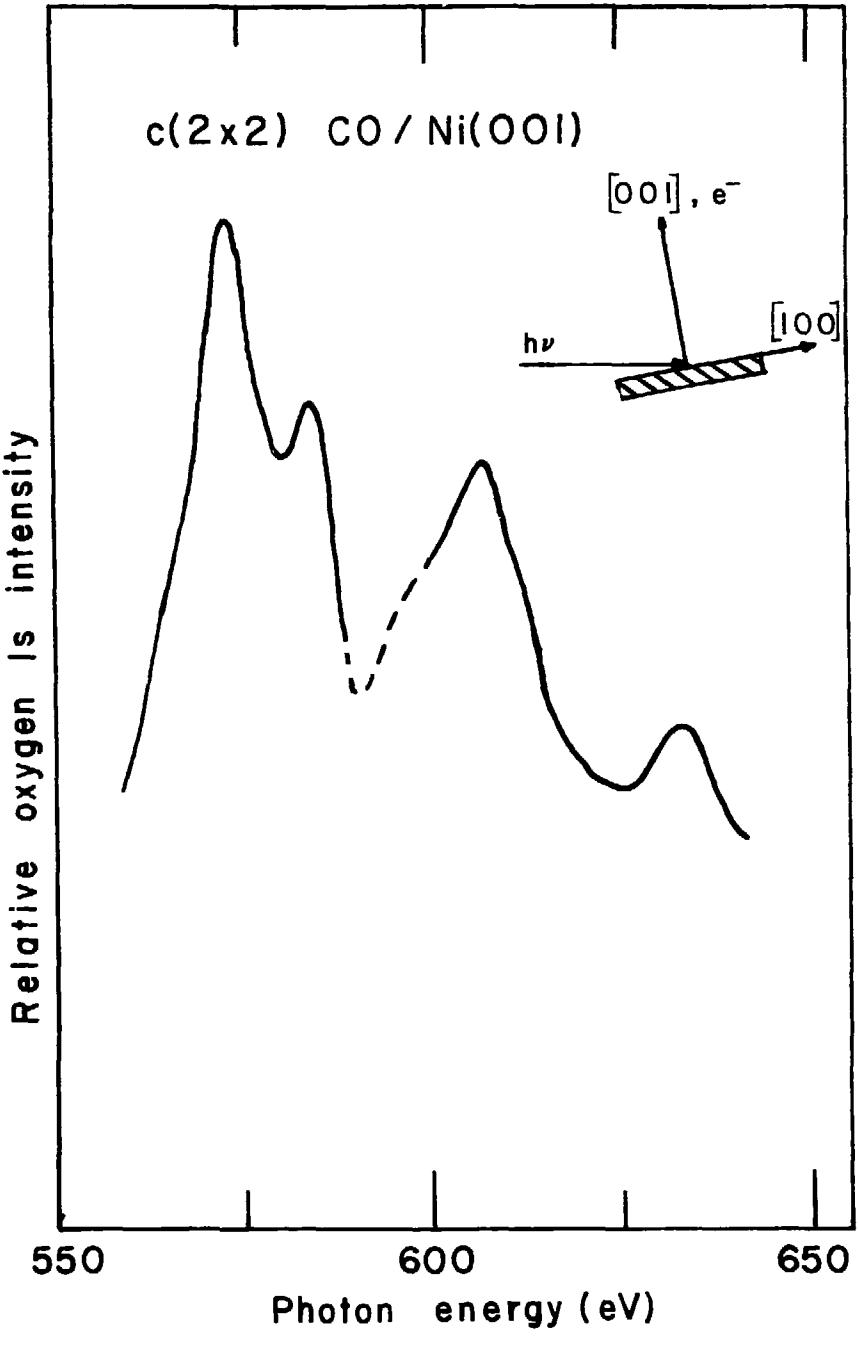

XBL 806-10509

Figure 25

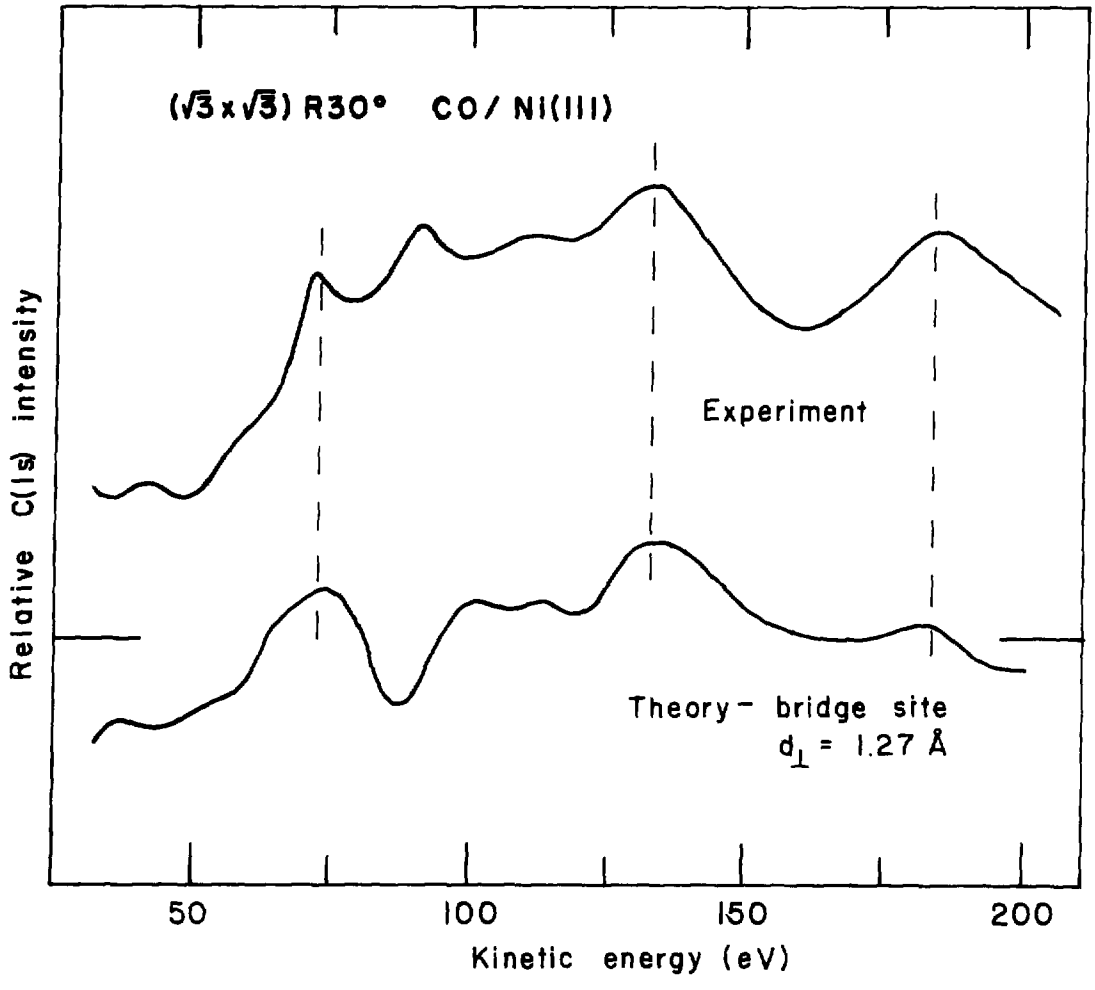

XBL 806-10510

Figure 26

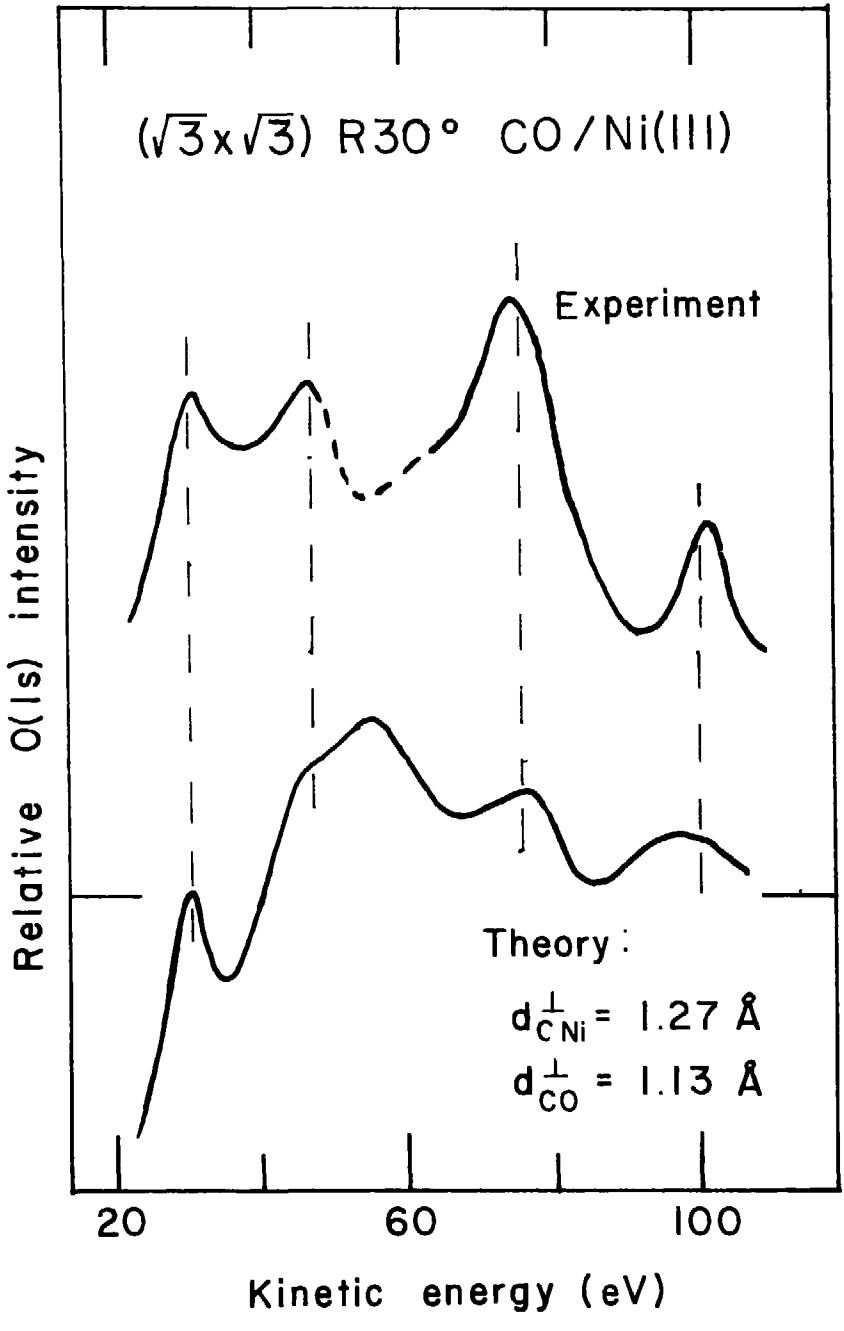

XBL 806-10511

Figure 27

IV. CONCLUDING REMARKS

The final chapter of a doctoral thesis is perhaps the most valuable from a long range point of view. It allows - indeed, forces - the author to evaluate objectively the output from several years of concentrated effort. This can provide insight into previous studies for future workers in the field as well as deliver guidance into possible future directions. I have organized this brief chapter in just that way: an evaluation of the past, an analysis of current questions and problems, and finally my thoughts on the future of photoelectron diffraction.

A. The past: What have we learned?

Three years ago, the major question concerning photoelectron diffraction was whether it would be sensitive to surface structure at all. The zero-order conclusion of this thesis and the various efforts reported elsewhere[1] is an emphatic affirmative response. Experimentally, the effect has been relatively large and easy to measure in every system we have studied. In fact, it is somewhat larger than one might at first expect, a point to which I will return shortly. Presently, the theoretical analysis lags behind our experimental output. In Table I, I show a list of systems which we have studied with the NPD technique to date, each accompanied by a mildly subjective evaluation of the state of the desired structural determination. An A means that a successful theoretical treatment has been completed, a B means that a treatment is in progress and, in most cases, preliminary results are encouraging, while C means that no treatment has been

undertaken yet. Perhaps the most striking feature of the table is the absence of failures, if one allows somewhat less stringent guidelines of what an "encouraging" result is for the oxygen 1s level. One of the significant factors contributing to this success rate is the effort expended over the last decade in treating LEED data. If PhD had been the first accurate surface structural technique, it would likely have had many of LEED's failures. When one considers that currently the theoretical treatment of PhD is about as difficult as LEED the two are more or less equivalent as techniques.[2] Considering the relative experimental ease and convenience of LEED and the sparcity of synchrotron radiation sources, PhD would clearly have no future if its structural sensitivity did not either complement or improve upon that of LEED.

It was essentially for this reason that we continued to pursue and develop the NPD technique to clarify its differences and potential advantages over LEED. The results of this effort have been fruitful, and are all reliant upon the localized nature of PhD and its relation to EXAFS. One of my more recent quips, in fact, is that PhD is an average of LEED and EXAFS, with enough characteristics of each to make it an entity unto itself. The application to disordered systems indicates the relation to EXAFS, for example, while the sensitivity (of NPD, at least) to $d_\perp$ rather than nearest-neighbor distances or absolute registry is specifically a LEED characteristic. These two characteristics - the localized nature and the sensitivity to $d_\perp$ - have been shown to combine to give NPD more promise in dealing with

molecular systems than LEED and probably also surface EXAFS. It is these features of PhD which must be developed and refined, and which in the long run will determine PhD's role as a surface structural tool.

B. The present: Where are we now?

It is also the two main features mentioned above with which the most current problems are involved. The relation of two-dimensional ordering to the experimental NPD result, for instance, is very important. I have previously stated that the degree and type of two-dimensional order in the overlayer has little effect on the NPD result. Indeed, in the systems we studied and at the level of accuracy at which we performed the experiments, this seems to be the case, but as the tecnique progresses and as we attain the ability to observe the subtleties in our curves, this conclusion will need to be carefuly checked. Such studies could prove useful, for example, in dealing with and measuring the extent of lateral interactions between adatoms. NPD's sensitivity to d_1 was a subject which was largely avoided in Chapter III. The core of the problem is found in Fig. 3 of Chapter I: the phase difference between the outgoing waves in PhD is $\Delta\phi = (1+\cos\theta)kr$ implying that one might expect sensitivity to $(1+\cos\theta)r$ rather than d_1. If there are many neighboring atoms, as at a surface, it is not at all clear why one should observe the magnitude of effect I reported in this thesis since the several scattered components which must add coherently will in general be out of phase leading to substantial averaging.

A very simple model can be developed which at least begins to explain this apparent contradiction. If one assumes an s initial state (or at least that the photon energy is well above threshold) and that a single scattering formalism is applicable, an analytic expression for the ARP intensity can be easily derived as shown in several places:[3,4]

$$I(k) \sim \rho\sigma^2 \left| \hat{\varepsilon}\cdot\hat{k} + \sum_j \frac{f(\theta_j)}{r_j} \exp\left(ikr_j(1+\cos\theta_j)\right) \hat{\varepsilon}\cdot\hat{r}_j \right|^2 \qquad (1)$$

Here ρ is the density of final states, σ is the atomic matrix element describing the absorption event, $\hat{\varepsilon}$ is the unit vector parallel to the polarization vector, r_j is the distance from the absorbing atom to the scattering atom j, and $f(\theta_j)$ is the complex scattering amplitude of atom j at θ_j, the angle between $\vec{r}_j$ and $\vec{k}$. The interpretation of equation 1 is simple: the first term in brackets is the direct term ($\hat{\varepsilon}\cdot\hat{k}$ is the result of assuming an s initial state), while the sum adds a contribution to the final state due to single scattering events. $(\hat{\varepsilon}\cdot\hat{r}_j)/r_j$ is the amplitude of the outgoing wave at atom j, and $kr_j(1+\cos\theta_j)$ is just the previously mentioned phase factor. Lee[3] showed that for an adsorbate on a crystalline surface this equation can be transformed into k-space, indicating the relation of the PhD final state to a coherent superposition of LEED beams, and yielding an equation identical to Liebsch's[5] single scattering result. To perform calculations with this equation would no doubt be cumbersome and fruitless; my purpose in using it lies in its analytic nature and in

the hope that the results to be derived are indicative of some general trend.

The direct and scattered waves are added coherently; the PhD effect, like the EXAFS effect and unlike LEED, arises from the cross term. If we set $I_0 = \rho\sigma^2(\hat{\varepsilon}\cdot\hat{k})^2$ and neglect the term involving the product of the sum with itself, we get

$$\frac{I-I_0}{I_0} = \sum_j \frac{(\hat{\varepsilon}\cdot\hat{r}_j)}{(\hat{\varepsilon}\cdot\hat{k})r_j} \left\{ f(\theta_j)\exp(ikr_j(1+\cos\theta_j)) + \right.$$

$$\left. f^*(\theta_j)\exp(-ikr_j(1+\cos\theta_j)) \right\} \qquad (2)$$

$$= \sum_j \frac{2(\hat{\varepsilon}\cdot\hat{r}_j)\left|f(\theta_j)\right|}{(\hat{\varepsilon}\cdot\hat{k})\, r_j} \times \cos\,(kr_j(1+\cos\theta_j) + \delta_j) \qquad (3)$$

where $\delta_j = \arg(f(\theta_j))$. If we now note that, <u>for normal emission</u>, $r_j\cos\theta_j = d_j^{\perp}$, where $d_j^{\perp}$ is the interlayer spacing between the absorbing atom's layer and the scattering atom's layer, we get after expanding the cosine of a sum

$$\frac{I - I_0}{I_0} = \sum_j \frac{2(\hat{\varepsilon}\cdot\hat{r}_j)\left|f(\theta_j)\right|}{(\hat{\varepsilon}\cdot\hat{k})r_j} \left\{ \cos(kd_j^{\perp})\cos(kr_j+\delta_j) - \right.$$

$$\left. \sin(kd_j^{\perp})\sin(kr_j + \delta_j) \right\} \qquad (4)$$

Changing the sum over all atoms j to a sum over layers l and atoms in each layer i, we get

$$\frac{I - I_o}{I_o} = \cos(kd_l)(X_l) + \sin(kd_l)(Y_l) \qquad (5)$$

where

$$X_l = \sum \frac{2(\hat{\epsilon}\cdot\hat{r}_{il})}{(\hat{\epsilon}\cdot\hat{k})r_{il}} \times \left|f(\theta_{il})\right| \times \cos(kr_{il} + \phi_{il}) \qquad (6a)$$

and

$$Y_l = \sum \frac{2(\hat{\epsilon}\cdot\hat{r}_{il})}{(\hat{\epsilon}\cdot\hat{k})r_{il}} \times f(\theta_{il}) \times \sin(kr_{il} + \delta_{il}) \qquad (6b)$$

Considering that the mean-free-path of the electron is 5-10 Å typically, the quantities X and Y in equations 6 involve sums over at least 30, and, for convergence, as many as 100 atoms, each atom contributing a unique frequency. X and Y therefore might be expected to be rather smooth functions of k, at least at higher values of k. On the other hand, only 3-4 layers will contribute substantially to the sum over layers. We arrive at the result that the quantity $(I-I_o)/I_o$ can be expected to oscillate with an amplitude characterized by the functions X and Y, but at a frequency sensitive to the d_l values for the various layers. This is precisely what is predicted by Tong's multiple scattering calculations. The hypothesis is that, while the single scattering equations will not adequately describe the NPD

result in detail, they do provide a tentative explanation for both the magnitude and the sensitivity of the technique. It is important to note that Equation 5 only holds for NPD since $r_j\cos\theta_j$ is not the same as $d_j^{\perp}$ for oblique emission angles. This is one way of explaining why APD studies have generally reported smaller effects.[1]

Another interesting application of Equation 5 is that it has the appearance of an EXAFS equation.[6] One implication of this is that Fourier transforms of NPD data at high energies might yield structural information directly. While some success has been attained in transforming Tong's calculated results, as yet no experimental data at high enough energies exist to test the validity of the idea. Another result of Equation 5 is that a treatment of vibrational effects similar to that of Schmidt[7] could be carried out with the result that NPD data would be sensitive to vibrations through a Debye-Waller-like factor, in qualitative agreement with our results.

Another issue which I have periodically addressed in this thesis is the applicability of a single scattering formalism to PhD. In the x-ray regime, PhD experiments have been undertaken and interpreted within such a formalism with a fair amount of success.[8] Apparently, somewhere between our energy range and 1000 eV, a single scattering limit seems to become a reasonably good approximation. From both a theoretical and a practical point of view, it will be important to determine (once and for all?) the usefulness of such a formalism.

C. The future: Is there any?

While I have already largely spoken to this question, a few comments seem to be in order. I started Chapter III with a warning that PhD is still a new technique which must weather several storms before it is commonly accepted as useful. While my feelings concerning the common acceptance of PhD have not changed in the course of writing this thesis (it still is not), I do believe that the technique has enough potential and unique characteristics that it should be actively pursued with the eventual goal of reaching a consensus.

References: Chapter IV

1. See Chapter I, Ref. 33-7.
2. I again emphasize the importance of moving to pulse counting techniques in LEED.
3. P. A. Lee, Phys. Rev., B13, 526 (1976).
4. L. McDonnel, D. P. Woodruff, and B. W. Holland, Surface Science, 51, 249 (1975).
5. Chapter I, Ref. 29.
6. Chapter I, Ref. 37.
7. Chapter III, Ref. 21.
8. Chapter I, Ref. 36, Chapter III, Ref. 36.

Table I. Systems studied by NPD

System	Level	Status
p(2x2)Se/Ni(001)	Se(3d)	A
c(2x2)Se/Ni(001)	Se(3d)	A
Se/Ni(001)-low coverage	Se(3d)	C
c(2x2)Se/Ni(001)	Se(3d)	C
(2x2)Se/Ni(11)	Se(3d)	C
$(\sqrt{3}x\sqrt{3})R30^{\circ}$Se/Ni(111)	Se(3d)	C
Se/Ni(111)-low coverage	Se(3d)	C
c(2x2)S/Ni(001)	S(2p)	A
c(2x2)S/Ni(011)	S(2p)	C
c(2x2)O/Ni(001)	O(1s)	C
c(2x2)CO/Ni(001)	C(1s)	A
c(2x2)CO/Ni(001)	O(1s)	B
$(\sqrt{3}x\sqrt{3})R30^{\circ}$CO/Ni(111)	C(1s)	A-B
$(\sqrt{3}x\sqrt{3})R30^{\circ}$CO/Ni(111)	O(1s)	B

ACKNOWLEDGEMENTS

It is impossible to produce a dissertation in the physical sciences without a large amount of support from a variety of people. I wish to thank some of the people who have made my efforts both possible and enjoyable. Each deserves much more credit and appreciation than I could ever hope to deliver in a few paragraphs.

The person who has had by far the largest impact on my scientific career is my thesis advisor, Professor D. A. Shirley. His excellence as a scientist is a constant source of inspiration; I have benefited immensely from his guidance.

I am thankful for the help and collaboration of several past and present members of our research group at LBL. Most of my experimental expertise and a good deal of my knowledge of photoemission was learned from Drs. P. S. Wehner and R. S. Williams. The collaborative building effort with Prof. F. R. McFeely is gratefully acknowledged. It has also been my pleasure to work with Professor N. Winograd and Dr. M. G. Mason during my tenure at Berkeley. Particular thanks go to Drs. D. Denley and B.-C. Lu, and to R. F. Davis, D. H. Rosenblatt, and J. G. Tobin who have been my closest friends and colleagues over the last two years. I wish also to thank D. J. Trevor, whose encyclopedic knowledge of instrumentation has been invaluable.

The support of the staffs at LBL and SSRL has been essential to the efforts reported in this thesis. The list of people whose help I have received is long, and I apologize in advance for neglecting to adequately thank most of them here. At SSRL, Dr. J. Stohr has been

helpful on several occasions on both a scientific and a practical level. Of particular note at LBL are J. Katz, D. Malone, and R. Strudwick whose design work was essential in putting our desires into a usable form. Ms. K. Janes, Ms. M. Bowman, and Ms. B. Komatsu have been helpufl in interfacing our results to the various printed media. My sincerest thaks go to Ms. Wini Heppler, who, in her roles as accountant, crystal cutter, and surrogate mother, has made my time at LBL a little more pleasant.

It is a humbling experience to attempt to thank ones' parents for a lifetime of love, patience, and support. Mine are truly tne best; this dissertation is as much theirs as it is mine.

Finally, I have the task of thanking Ms. Geri Richmond, who has endured my shortcomings for these last three years. Our relationship is as wonderful and fulfilling as it is undefined. My years at Berkeley would have been empty if not for her love, support, and companionship in scientific as well as non-scientific endeavors.

This work was supported by the Divison of Chemical Sciences, Office of Basic Energy Sciences, U.S. Department of Energy under Contract No. W-7405-ENG-48. It was performed at the Stanford Synchrontron Radiation Laboratory, which is supported by the NSF Grant No. DMR 77-26489, in cooperation with the Stanford Linear Accelerator Center.

APPENDIX I: POWER SUPPLIES AND VOLTAGES

Our procedure in providing power supplies for the hemispherical analyzer was to start with a comercially available supply which provided most of the desired functions and then to provide necessary modifications and extensions. We chose the Physical Electronics model 20-805 cylindrical mirror analyzer supply due to its required stability characteristics. A schematic of our final supply system is shown in Fig. AI-1. The 20-805 supplies the kinetic energy (KE), the inner (V_{in}) and outer (V_{out}) hemisphere voltages, and the mid-plane voltage (V_2). KE is provided by a high voltage operational amplifier and has switch selectable sweep and offset gains. The energy range in the UPS mode is 0-200 eV, and the power supply sweep gain is approximately -10, while in the XPS mode, the range is 0-2000 eV and the gain is -20. The sweep gain is a critical parameter as will be explained later. V_2 is formed by a simple summing junction, and V_{in} and V_{out} are derived from V_2 by two more supplies. The pass energy is variable in powers of two between 2.5 eV and 160 eV.

These four voltages are provided to a second power supply which then produces the rest of the lens voltages as well as the field terminating electrode voltages. V_1 and V_3 are the focusing voltages for the Einzel lenses. V_4 is applied to the first collimator and acts as the first stage of acceleration between the two lenses. The field terminating electrode voltages are produced by a resistive voltage divider between V_{in} and V_{out}. Channel plate and collector voltages are provided by a third power supply (Fig. AI-1, Physical Electronics No. 20-075). Table AI-1 summarizes the designations, functions, and values for the various voltages.

One circuit which is characteristic of our counting system alone and deserves some comment is the gain select on the kinetic energy sweep circuit. The multichannel detection system makes the power supply sweep gain critical in determining experimental resolution. The reason for this is straightforward. The width of the energy window at the exit plane of the analyzer is approximately 0.116x the pass energy. One digitizes this window with 8-bit resolution, so that the minimum energy per channel is $0.116 \times PE/256 = 4.53 \times 10^{-4} \times PE$. Since the analog input to the analyzer sweep originates in a 12-bit A/D converter in the LSI-11 microprocessor (Appendix II), one wishes to make an incremental change of one digit in the A/D converter lead to a change in analog output from the kinetic energy supply of one minimum energy per channel. If this condition is not met, energy resolution suffers as indicated schematically in Fig. AI-2. Data are accumulated (in this hypothetical case) into a 4-channel buffer memory and read into an 8-channel spectrum. If the energy per channel of the buffer and spectrum are the same (case a), incrementing the energy by one D/A bit maintains the registry of the channels in the two arrays. If one the other hand the channel sizes are different (case b) the two arrays work their way out of registry as the voltage is swept to accumulate the spectrum. It should be noted that this sweeping is essential to average out channel plate inhomogeneities (see Appendix II). The minimum energy per channel in the buffer memory is fixed for each pass energy as explained earlier and is determined by unalterable constraints such as the radii of the hemispheres. On the other hand,

the energy per channel of the spectral array is variable and controlled by the gain select circuit and the analyzer power supply gain as explained below.

The gain select circuit is shown schematically in Fig. AI-3. Output from the A/D in the LSI-11 microprocessor is in the range 0-10.24 V, and hence the incremental step size is 2.5 mV/bit. This step size is input to the gain select, the gain of which is controlled by 8 parallel bits from the LSI-11. Each bit corresponds to a different pass energy and hence a different output step size. One of the eight bits is set and the gain of the AD503 op amp is determined by the R_f/R_i ratio to give the appropriate output step for that pass energy. In practice, the gains of the various resistor combinations are set in powers of two to an approximately correct value, and then the gain of the 20-805 UPS and XPS kinetic energy sweep supplies are adjusted to optimize the experimental resolution.

An estimate of the magnitude of the effect is straightforward. In a typical experiment, there are about 30 virtual entrance slits in the analyzer exit plane. If the gain is wrong by 3 percent, the spectrum and buffer move out of phase by about one unit resolution over the width of the window, so that the resolution is degraded by a factor of two. Figure AI-4 shows two EDC's of the sharp M point surface state on Cu(100)[1,2] taken with the power supply gain optimized (bottom curve) and the gain wrong by about 2 percent. The effect is clearly one of the most significant in determining experimental resolution.

References: Appendix I

1. P. Heimann, J. Hermanson, H. Miosga, and H. Needermeyer, Phys. Rev. Lett., 42, 1782 (1979).

2. S. D. Kevan and D. A. Shirley, Phys. Rev., BXX, XXX(XXXX).

Table AI-1. Hemispherical analyzer voltages

Designation	Function	Value
KE	kinetic energy	0-200 eV
PE	pass energy	2.5-160 eV
V_2	midplane voltage	-KE+PE
V_{out}	Vf_2 - .2105*PE	outer hemisphere
V_{in}	V_2 + .2667*PE	inner hemisphere
V_4	first stage retarder	f_4V_2, $.7 \leq f_4 < .9$
V_1	first focus	f_1*KE, $.8 \leq f_1 \leq 1.0$
V_3	second focus	f_3*KE, $.8 \leq f_3 \leq 1.0$
V_{S_i}, i = 1,5	termination electrodes	r^{-1} between V_{in} and V_{out}
minus	CEMA front	V_2 + 100V
center	CEMA middle	minus + 1kV
plus	CEMA exit	center + 1kV
B_1	resistive anode	plus + 100V

Figure Captions: Appendix I

Figure 1. Schematic of Power supply setup and simplified cabling diagram.

Figure 2. Schematic of properly and improperly adjusted supply gain. Top: properly adjusted so that channels in spectrum and buffer stay adjusted. Bottom: not properly adjusted. Note that the channels in the spectrum do not stay in registry with the buffer with a consequent loss of resolution.

Figure 3. Schematic of gain select circuit.

Figure 4. Observed degradation of experimental resolution due to improper adjustment of lens supply gain.

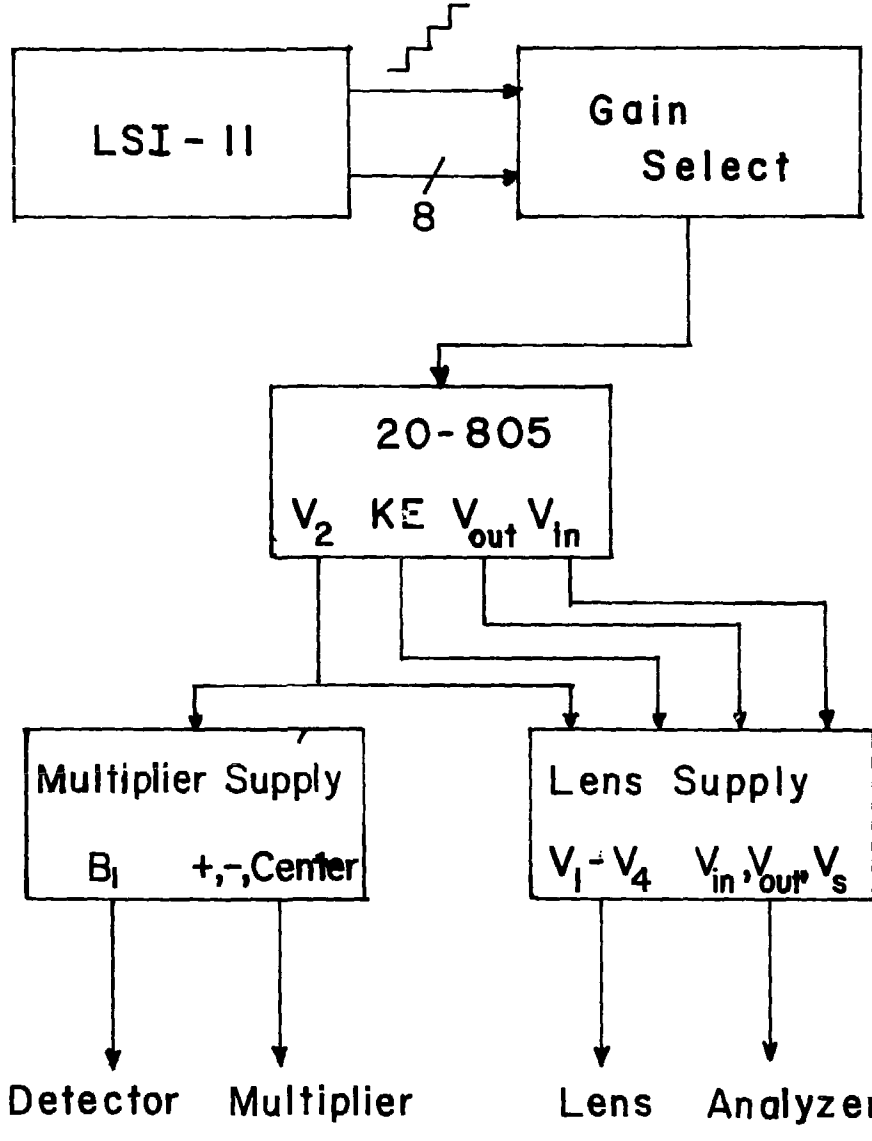

XBL 806-9951

Figure 1

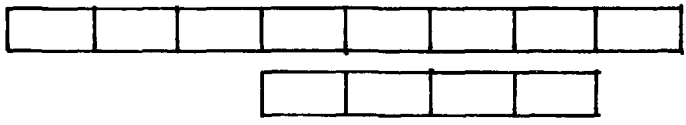

Spectrum Buffer

a) $\Delta E_S = \Delta E_B$

Spectrum Buffer

b) $\Delta E_S = 1.1 \times \Delta E_B$

XBL 806-9952

Figure 2

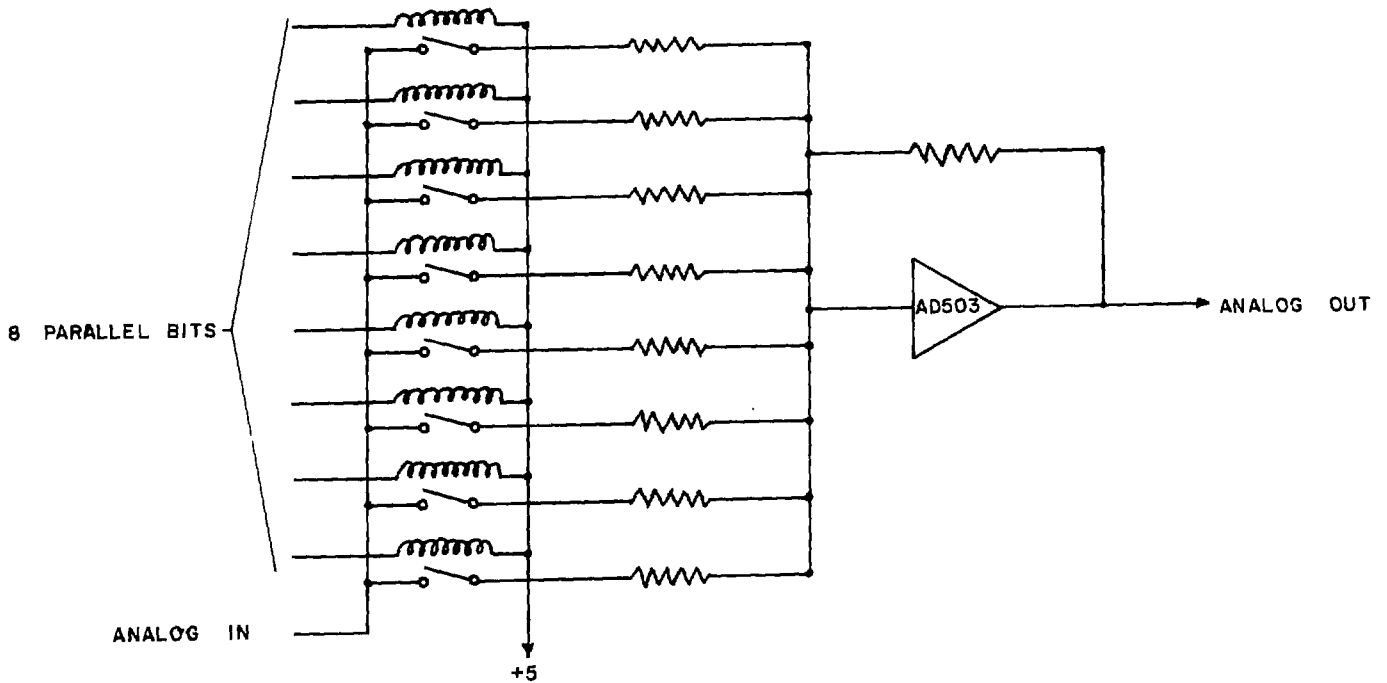

GAIN SELECT CIRCUIT

XBL 806-9967

Figure 3

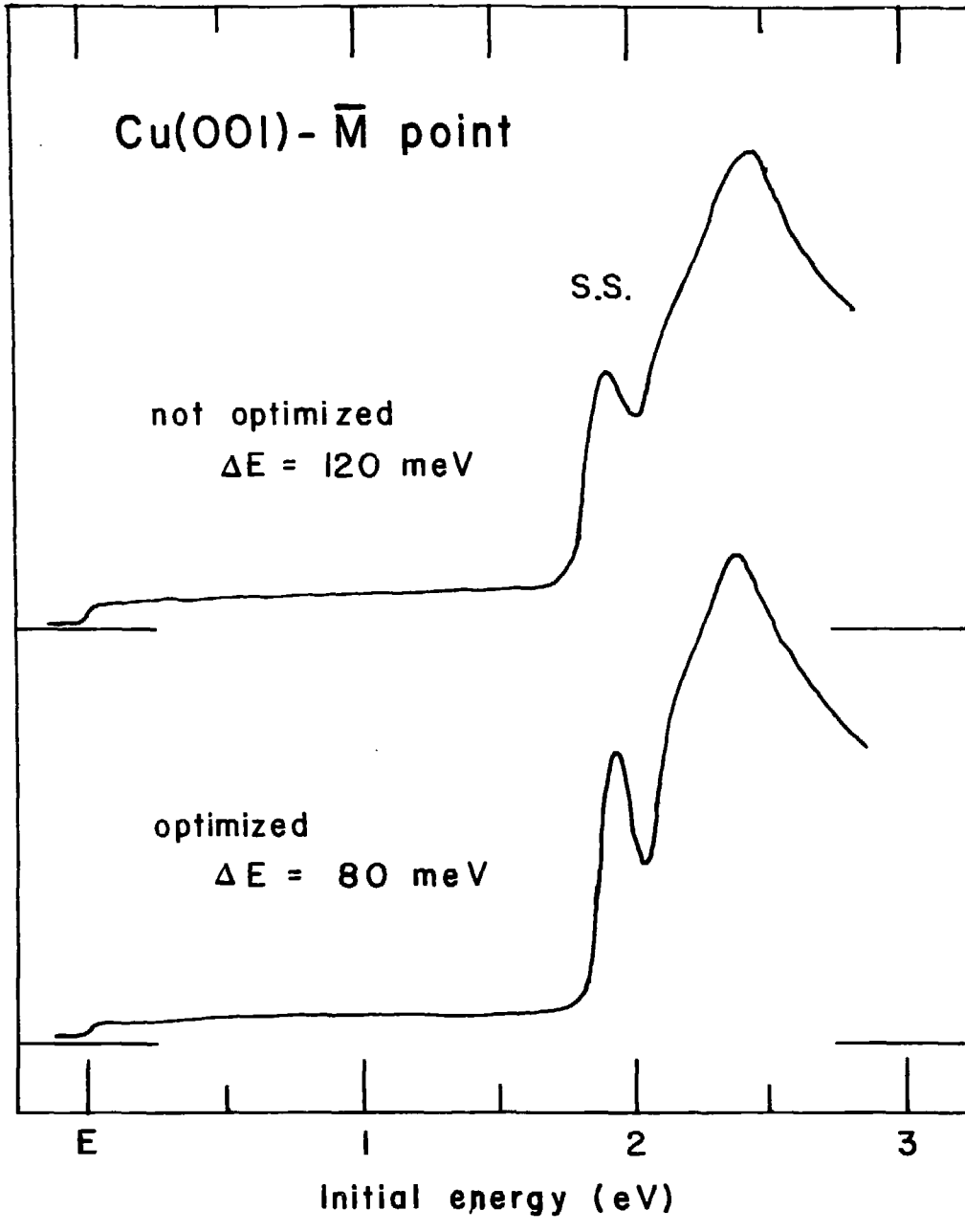

XBL 806-9956

Figure 4

APPENDIX II: MICROPROCESSOR HARDWARE AND SOFTWARE

Perhaps the most difficult area to provide continuity in a research group between entering and leaving students is that of computer hardware and software. DEC equipment is sufficiently straightforward that in nearly all cases, starting from scratch, one can interface their experiment in a matter of a few months. On the other hand, the author appreciates the difficulty involved in interpreting a particular person's way of doing things and hence I will provide a reasonably complete description of what for most readers can be left as a black box.

The LSI-11 Q-bus[1] requires that every computer circuit board inserted into the backplane have a unique address and, in most cases, also an interrupt vector. The fact that each board has a unique address makes the order of the boards largely unimportant except for those with active interrupt status or those with sensitive analog voltages which require lower noise positions. These requirements have been met by positioning the realtime clock and the A/D and D/A boards as close to the microprocessor and as far from the memory board as possible. Otherwise, position in the backplane is unimportant as long as no spaces are left open in the daisy-chain structure.[1]

A list of the boards used in the microprocessor is given in Table AII-1, along with their functions, addresses and, where appropriate, interrupt vectors. A brief description of each board follows:

1) DRV11- 1: 16 bit parallel I/O to control and read data from the one-dimensional digitizer. Also, the 8 parallel bits controlling the gain select circuit (Appendix I) are on this board, as well as three lines for controlling the grasshopper monochromator at SSRL. A complete list of the 16 I/O bits and their functions is given in Table AII-2.
2) DRV11- 2: 16 bit parallel I/O to control an incremental Calcomp plotter and an Ortec Counter/Timer. Table AII-3 gives a list of functions of these I/O bits.
3) AAV11: Four channel, 12 bit resolution D/A converter. Analog output range is wired to be 0-+10.24V, so the incremental step is 2.5 mV. Channel 0 controls the spectral sweep input of the gain select circuit, and channel 1 controls the kinetic energy offset for the beginning of each spectrum. This offset input of the 20-805 supply (Appendix I) has a gain of -20 and -100 for the UPS and XPS supplies, respectively. Channels 2 and 3 are available for future needs.
4) KWV11: Programmable realtime clock controls the timing of data acquisition.
5) Datel A/D-D/A: 16 channel, 12 bit resolution A/D converter, and two channel 12 bit resolution D/A converter. The D/A, wired with an analog range of -5.12V-+5.12V, controls a Hewlett-Packard display on which photoemission spectra are viewed as they are accumulated. Only the first four A/D channels are presently in use.

6) DSD-11: Controller for Data Systems Design floppy disc drive.

7) DLV11-J: Four channel RS-232 compatible serial I/O port for controlling a VT55 graphics terminal (channel 3), and an Intel 8080 microprocessor dedicated to controlling the grasshopper monochromator at SSRL (channel 1). Channels 0 and 2 are available for future use.

A more complete description of specific hardware components and the interfacing structure may be found in a notebook entitled "ARPES LSI-11 configuration," while a more general description of the LSI-11 bus structure may be found in the DEC user's manual.[1]

As promised in Chapter II, a complete description of the data acquisition program run as the foreground job will be given here. In a single channel counting system, the usual technique is to set the analyzer voltages to a particular kinetic energy, count for a certain amount of time, step the voltages, and repeat this cycle until the desired range of kinetic energy has been swept. In the multichannel counting system described in this thesis, one might expect to do the same thing, only stepping by analyzer energy window-width (ΔE = .116*pass energy in this case) instead of channel widths. Such a procedure would not work very well in practice due to the non-uniformity of the channel plate and digitization electronics. A significant electronic signature would appear in what would otherwise be a smooth photoemission spectrum. Instead, the spectrum must be swept through channelwise, keeping track of where the counts in a particular buffer memory channel belong in the spectrum. The process, which we call

dithering, is shown schematically in Fig. AII-1. The horizontal dimension is energy, and the goal is to fill N(E) into the spectral array. The energy window of the anayzler is swept across the spectral energy range so that every energy channel in the spectrum is sampled equivalently by every position of the energy window. The process starts with the analyzer window overlapping the spectrum by the first channel in each as shown in the top part of the figure. The window is then swept until only the last channel of each overlap. The computer program keeps track of which channel in the buffer memory is added to which channel of the spectral array. We add two further complications in the following ways. Fringing fields are expected to be most severe near the extremes of the energy window, i.e., near the hemispheres themselves. Hence, we divide the 256 channel energy window into 16 groups and count into only n groups, $1 \leq n \leq 16$, in the middle of the window. Also, since the minimum energy/channel (.116*PE/256) is always somewhat smaller than the experimental resolution, we introduce a memory divisor MD so that the buffer memory channels are added in groups of MD. For simplicity, MD must be a power of two. The D/A controlling the voltage sweep must of course also be stepped in units of MD (see Appendix I).

With these introductory words, I proceed with a description of the program ARPFB which controls data acquisition. A flow chart is shown in Fig. AII-2. The program starts in subroutine ARPIN, the routine which inputs the various parameters to describe the desired spectrum: spectral energy window width (WW), analyzer pass energy (IPE), number

of scans (NS), the number of milliseconds per step (NMSEC), angles (THETAE, PHIE. THETAP, PHIP) describing the position of the analyzer and sample, and the photon energy (HV). The routing also reads the beginning kinetic energy offset (EKIN), clears the spectral array (SPEC), and initiates the pointers required for data acquisition. After returning to the main program, a double loop is entered to accumulate the desired spectrum. One loop controls each scan through the spectral energy range, and the other controls the number of scans taken. The first of these is the heart of the dither and interrupt programming and will be described in some detail shortly. After completing acquisition, one has the choice of starting a new spectrum, dumping the present spectrum, or continuing on the present spectrum.

Another program, ARPCIS, is similar to ARPFB, except that some control over the grasshopper monochromator is provided so that a photoelectron diffraction curve may be generated more easily.

The data acquisition loop (Fig. AII-3) has several tasks. The dither process is shown in Fig. AII-4. The pointers NC1 and NC2 are of central importance. They point to the beginning and ending virtual spectral channels into which data is being read. In other words, NC1 can be less than 1, in which case data acquisition is near the beginning of the dither and the analyzer energy window only partially overlaps the spectral energy range. In addition, NC2 is larger than the number of spectral channels (NCH) near the end of the dither. Numbers N1 and N2 are derived from NC1 and NC2 and point to the actual first and last spectral channels to receive data. Also, NB1, the first

channel to be read from the buffer memory, is derived. The three different cases which occur in the course of a dither are shown in Fig. AII-1. In the real case, the number of groups (NGR) and the memory divisor (MD) must be taken into account. After the buffer memory is read, NC1 and NC2 are incremented, the voltages are stepped, and the next counting period begins.

This period is initiated by clearing the buffer memory, starting the realtime clock, and enabling the counting by the digitizer. At this point, the spectrum is displayed on the Hewlett-Packard display, and then the foreground job is suspended, leaving the clock running and the digitizer counting. The background (data analysis) job is active during this counting period, which is ended when the realtime clock times out, interrupts the background job and restarts the foreground job. The buffer memory is again read and stored away, and the loop repeated until the end of one sweep. The duty cycle is typically in excess of 95 percent, meaning that only 5 percent of the data acquisition time is dead time when the digitizer is not counting.

References: Appendix II

1. Microcomputer Processor Handbook, Digital Equipment Corporation, 1979.

Table AII-1: Microprocessor circuit boards.

Designation	Function	Peripheral	Address	Vector
DRV11	16 bit I/O	digitizer	167770-6	300
DRV11	16 bit I/O	plotter, scaler	167760-6	270
AAV11	4 channel D/A	sweep, offset	170440-6	---
KWV11	clock	timing	170420-2	440
Datel	16-A/D, 2-D/A	read offset, beam current, lockin, control display	170400-6	360
DSD11	DMA I/O	diskett interface	177170-6	264
DLV11-J	4 channel	8080 micro (ch. No. 1)	176510-6	210, 214
KD11-F	LSI-11	microprocessor		
REV11-A		refresh, boot	173000	
INTEL-1611	memory, 28Kx 16 bits			

Table AII-2: DRV11 bit designations for controlling digitizer.

I/O bit number	output function	input function
0	enable count	data 0
1	clear memory	data 1
2	reset address	data 2
3	address advance	data 3
4	HP scope z-intensify	data 4
5	reset 8080	data 5
6	move monochromator	data 6
7	not used	data 7
8	gain: 7.38 mV/step	data 8
9	gain: 3.69 mV/step	data 9
10	gain: 1.84 mV/step	data 10
11	gain: .922 mV/step	data 11
12	gain: .461 mV/step	overflow
13	gain: .231 mV/step	not used
14	gain: .115 mV/step	mono. move done
15	gain: .058 mV/step	computer/local

Table AII-3: DRV11 bit designations for controlling plotter, scaler.

I/O bit number	output function	input function
0	print, stop count	scaler data 1
1	print advance	scaler data 2
2	previous module finished	scaler data 4
3	system present	scaler data 8
4	system reset	sto count
5	dwell time off	module finished
6	gate	module printing
7	not used	bad bit
8	Calcomp on	Calcomp busy
9	drum up	not used
10	drum down	not used
11	carriage right	not used
12	carriage left	not used
13	pen up	not used
14	pen down	not used
15	not used	not used

Figure captions: Appendix II

Figure 1. The positions of the buffer memory relative to the spectrum at three relevant positions during a scan. At the beginning of the scan, only the rightmost channel of the buffer is accumulating used data, while at the end of the scan only the leftmost channel is used.

Figure 2. Overall flow chart of the program ARPFB.

Figure 3. Flow chart of the loop controlling the dither and data accumulation.

Three Positions of Dither:

Upper Array : Spectrum - fixed energy
Lower Array : Buffer - varible energy

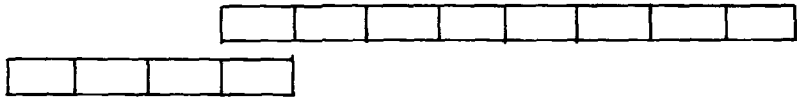

a) Beginning of Scan

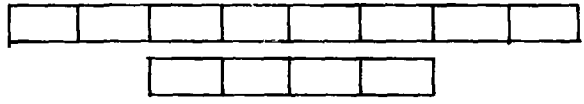

b) Middle of Scan

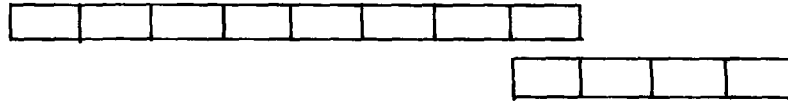

c) End of Scan

XBL 806-9955

Figure 1

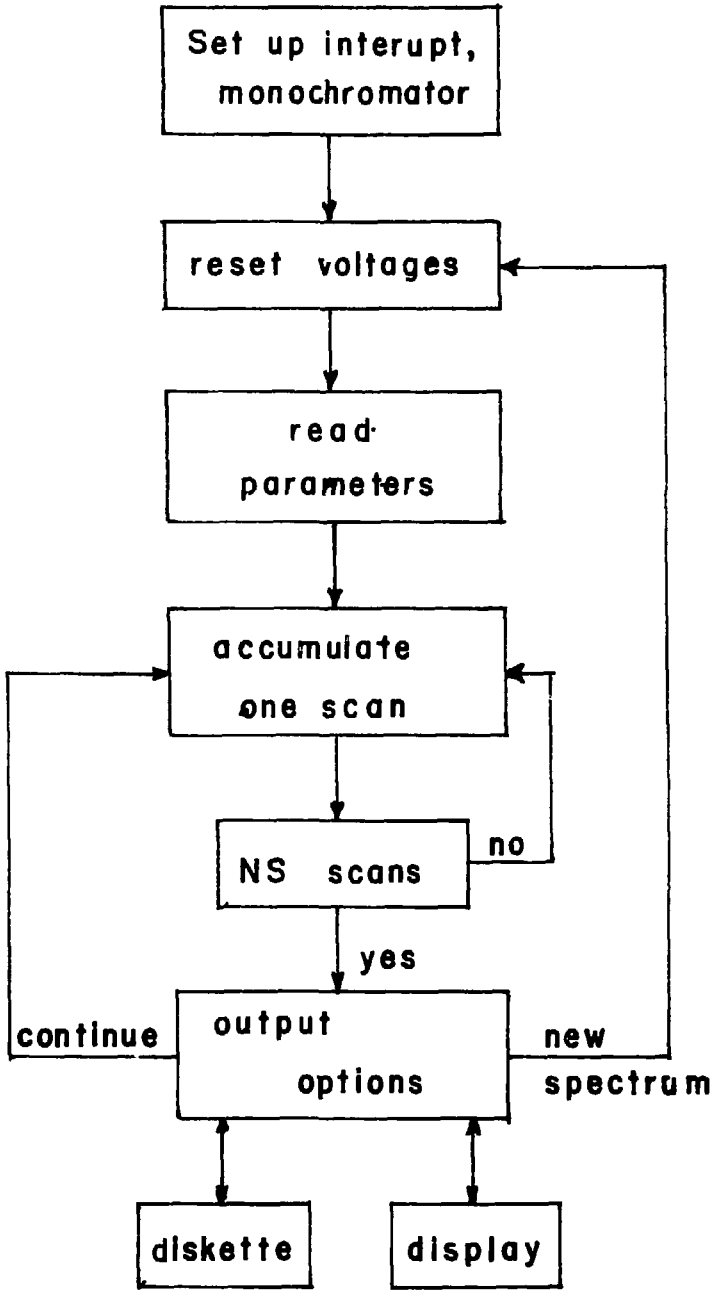

XBL 806-9954

Figure 2

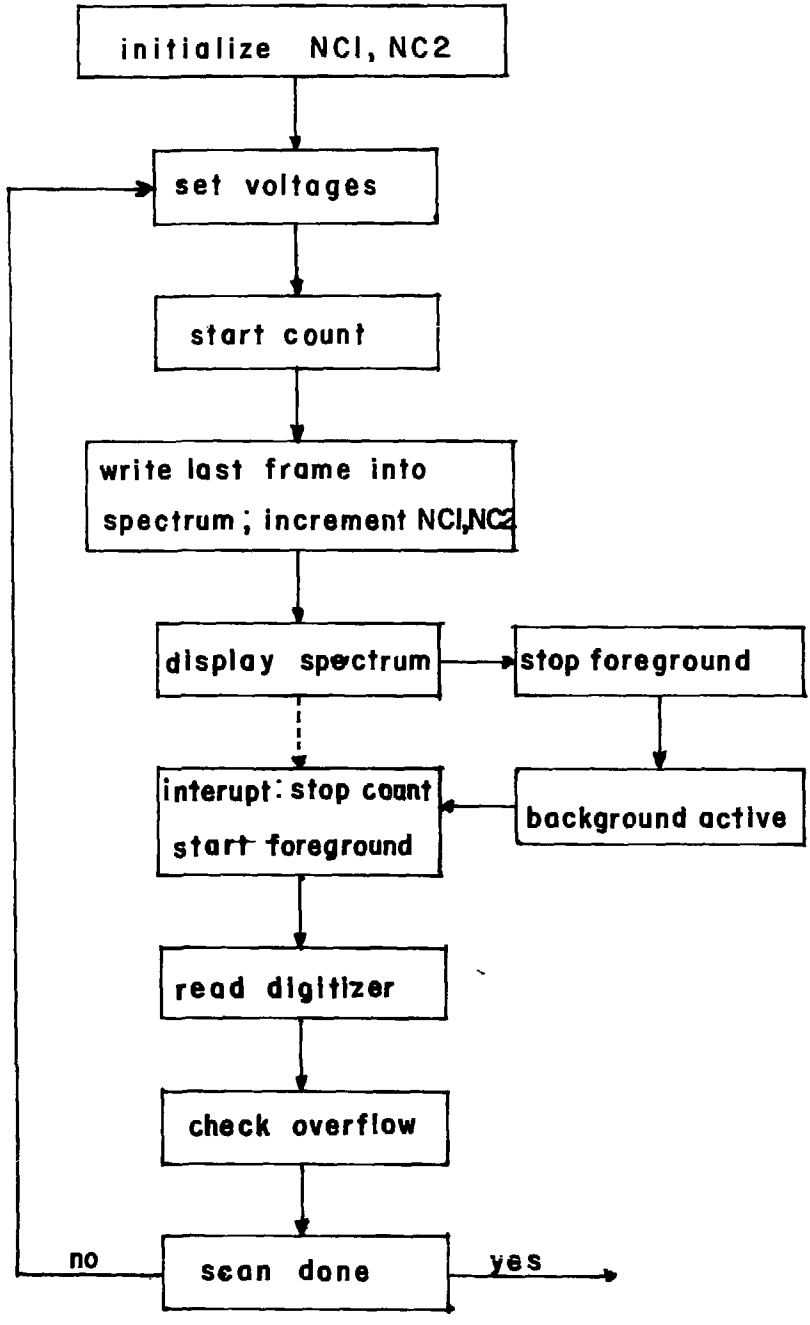
initialize NC1, NC2
set voltages
start count
write last frame into spectrum; increment NC1,NC2
display spectrum
stop foreground
interupt: stop count start foreground
background active
read digitizer
check overflow
scan done
no
yes
XBL 806-9953

Figure 3

APPENDIX III: EFFUSIVE BEAM DOSING

As explained in Chapter II, all gaseous exposures were performed by directing an effusive beam of gas at a clean sample. One wishes of course to control and measure the amount of gas one directs at the sample. The standard exposure technique is to admit a certain ambient partial pressure of the desired gas into the chamber for a certain period of time. Exposures are normally measured in units of 10^{-6} torr-sec or Langmuirs. For unit sticking porbability, approximately one Langmuir exposure will saturate the surface. If one uses the kinetic theory of gases, exposures using an effusive beam can be controlled and measured.

Figure AIII-1 shows a schematic of the exposure geometry. The sample is positioned a distance d from a small aperture of radius r. A partial pressure P_1 in microns of the appropriate gas is admitted to the region behind the aperture. From the kinetic theory of gases, the flux of molecules leaving region I for an effusive beam is

$$\dot{N}_I = \frac{P_I}{\sqrt{2\pi mkT}} \times A$$

where $A = \pi r^2$ is the area of the aperture, m is the mass of the gaseous molecules, k is the Boltzmann constant, and T is the absolute temperature. For T = 300K, m in AMU, and r in cm,

$$\dot{N}_I = 6.35 \times 10^{18} \quad \frac{P_I r^2}{\sqrt{m}} \text{ sec}^{-1}$$

Also, from the kinetic theory, we know that

$$\dot{N}_{II}(\theta) = K\cos\theta$$

where K is a normalization constant determined from the conditions that

$$\dot{N}_{I} = \int_0^{2\pi} d \int_0^{\pi/2} d\theta \sin\theta \dot{N}_{II}(\theta)$$

K can be calculated to be $\dot{N}_{I/\pi}$, so that

$$\dot{N}_{II}(\theta) = 2.02 \times 10^{18} \frac{P_I r^2}{\sqrt{m}} \cos\theta \ \sec^{-1}$$

We wish to determine $\dot{N}(\Delta\omega)$, where $\Delta\omega$ is the solid angle of beam intercepted by the sample:

$$\dot{N}(\Delta\omega) = \int_0^{2\pi} d\phi \int_0^{\theta_{max}} d\theta \sin\theta \ \dot{N}_{II}(\theta)$$

$$\dot{N}(\Delta\omega) = [1 - \cos^2\theta_{max}] \times 6.35 \times 10^{18} \frac{P_I r^2}{\sqrt{m}} \sec^{-1}$$

If we assume a circular sample of radius z, then

$$\cos\theta_{max} = \left(\frac{d^2}{d^2 + z^2}\right)^{1/2} \approx 1 - \frac{1}{2}\left(\frac{z}{d}\right)^2$$

so that

$$\dot{N}(\Delta\omega) = 6.35 \times 10^{18} \frac{P_I r^2}{\sqrt{m}} \left(\frac{z}{d}\right)^2 \text{ sec}^{-1}$$

For ambinet dosing,

$$N = \pi z^2 \frac{P_{II}}{\sqrt{2\pi mkT}} = 6.35 \times 10^{21} \frac{P_{II} z^2}{\sqrt{m}} \text{ sec}$$

where P_{II} is measured in torr. For one Langmuir,

$$N(1L) = 6.35 \times 10^{15} \frac{z^2}{\sqrt{m}}$$

Hence, the number of seconds/Langmuir for beam dosing is found to be

$$= 1 \times 10^{-3} \frac{d^2}{P_I r^2} \text{ sec}$$

In our case, r = .005 cm., so that

$$= 40 \frac{d^2}{P_I} \text{ sec}$$

Since we want to avoid measuring P_I during an exposure in order to keep from exposing our gas to a hot filament, this equation needs to be modified slightly. For an effusive beam, P_{II}/P_I is

constant but dependent on the chamber pumping speed, a poorly known quantity. In practice, the best procedure was found to lie in performing several trial runs to determine P_{II}/P_I for each gas. Then, during an actual exposure, measurement of P_{II} yields P_I. In most cases P_{II}/P_I $5x10^{-6}$, so that for P_I = 2 microns, P_{II} = 1 x 10^{-9} torr, and T = 20 sec for d = 1 cm. The chamber walls are exposed to approximately 50 times less active gas than they would be for an equivalent ambient exposure.

Figure captions: Appendix III

Figure 1. Schematic of the geometry near the sample during an effusive beam exposure.

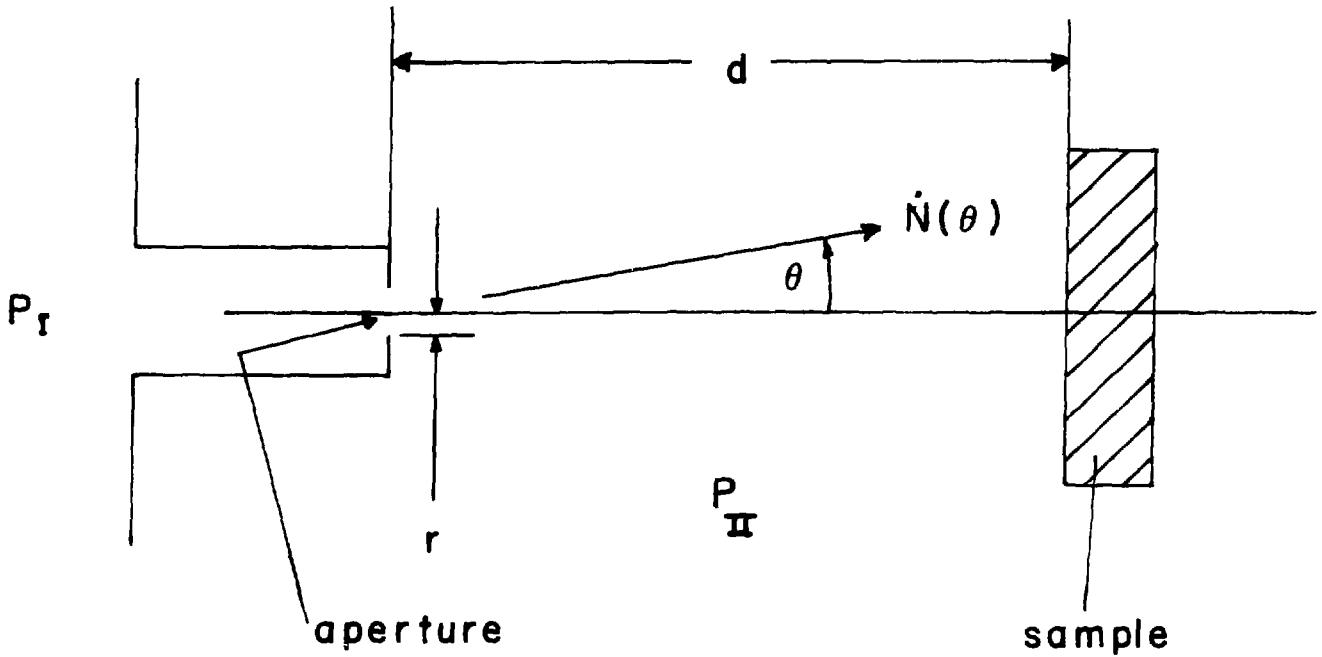

XBL 806-9950

Figure 1